研　究　成　果　報　告　書

難揮発性包有物とエンスタタイトコンドライトの変質作用

研究課題番号　１８５４０４８３

平成１８年度ー平成１９年度科学研究費補助金
（基盤研究（Ｃ））研究成果報告書

平成２０年６月６日

研究代表者　Ｔ．・Ｊ．　Ｆａｇａｎ
（フェイガン　ティモシー　ジェイ）

早稲田大学総合・科学学術院准教授

＜はしかぎ＞

基盤研究（C）「難揮発性包有物とエンスタタイトコンドライトの変質作用」
(課題番号18540483)

研究組織：

研究代表者　T.・J.　Fagan
（フェイガン　ティモシー　ジェイ）
早稲田大学教育・総合科学学術院

	直接経費	間接経費	合　計
平成　１８年度	2,400,000	0	2,400,000
平成　１９年度	900,000	270,000	1,170,000
総　計	3,300,000	270,000	3,570,000

研究発表：

〔雑誌論文〕　計（1）件

著　者　名	論　文　標　題				
Fagan T.J., Guan Y., MacPherson G.J.	Al-Mg isotopic evidence for episodic alteration of Ca-Al-rich inclusions from Allende				
雑　誌　名		査読の有無	巻	発行年	最初と最後の頁
Meteoritics and Planetary Science		有	42	2007	1221-1240

〔学会発表〕計（１１）件

発　表　者　名	発　表　標　題		
Fagan T.J., Guan Y. and MacPherson G.J.	Al-Mg isotopic constraints on alteration of Allende Ca-Al-rich inclusions		
学　会　等　名		発表年月日	発　表　場　所
Lunar and Planetary Sciences Conference 37		2006年03月17日	Houston, TX, USA

発　表　者　名	発　表　標　題
Komatsu M., Fagan T.J., Miyamoto	Amoeboid olivine aggregates in the Yamato-86009 CV3 chondrite

M., Krot A.N. and Mikouchi T.		
学 会 等 名	発表年月日	発 表 場 所
Lunar and Planetary Sciences Conference 37	2006年03月14日	Houston, TX, USA

発 表 者 名	発 表 標 題	
Komatsu M., Fagan T.J., Miyamoto M., Krot A.N., Mikouchi T. and Keil K.	Mineralogy and petrography of the oxidized CV chondrite Yamato 86009	
学 会 等 名	発表年月日	発 表 場 所
Antarctic Meteorites 30	2006年06月06日	東京国立極地研究所

発 表 者 名	発 表 標 題	
Fagan T.J., Krot A.N., Kobayashi S. and Yurimoto H.	Correlation between texture and oxygen isotopic systematics in CAIs from Acfer 094	
学 会 等 名	発表年月日	発 表 場 所
Lunar and Planetary Sciences Conference 38	2007年03月13日	Houston, TX, USA

発 表 者 名	発 表 標 題	
Fagan T.J., 工藤 美紀子	Setting of Na-alteration in a type B2 Ca-Al-rich inclusion from the Allende CV3 chondrite	
学 会 等 名	発表年月日	発 表 場 所
日本地球惑星科学連合２００７年大会	2007年05月23日	幕張メッセ国際会議場

発 表 者 名	発 表 標 題	
加島 大樹, Fagan T.J.	Fe-alteration of spinel in a fine-grained CAI from the Efremovka CV3 chondrite	
学 会 等 名	発表年月日	発 表 場 所
日本地球惑星科学連合２００７年大会	2007年05月23日	幕張メッセ国際会議場

発 表 者 名	発 表 標 題	
片岡 翔, 高橋 裕也, Fagan T.J.	Setting of equilibrium process in the EH chondrites based on chondrule types and silica polymorphs	
学 会 等 名	発表年月日	発 表 場 所
日本地球惑星科学連合２００７年大会	2007年05月23日	幕張メッセ国際会議場

発 表 者 名	発 表 標 題	
田才 雄,佐藤 公信, Fagan T.J.	Mineral alteration of type B1, B2 and fluffy type A Ca-Al-rich inclusions from the Allende CV3 chondrite	
学 会 等 名	発表年月日	発 表 場 所
日本地球惑星科学連合２００７年大会	2007年05月23日	幕張メッセ国際会議場

発 表 者 名	発 表 標 題
Ebata S., Fagan T.J. and	Identification of silicate and carbonaceous presolar grains in the

Yurimoto H.	type 3 enstatite chondrite ALHA81189	
学 会 等 名	発表年月日	発 表 場 所
Meteoritical Society Annual Meeting	2007年08月16日	Tucson, AZ, USA

発 表 者 名	発 表 標 題	
Fagan T.J., Kataoka S., Takahashi Y. and Matsui K.	Roles of chondrule formation and parent body metamorphism during equilibration of EH chondrites	
学 会 等 名	発表年月日	発 表 場 所
Meteoritical Society Annual Meeting	2007年08月14日	Tucson, AZ, USA

発 表 者 名	発 表 標 題	
Fagan T.J., Kataoka S., Matsui K., Norose K. and Yoshida A.	Equilibration reactions between silicates, sulfides and Fe,Ni-metal in EH chondrites	
学 会 等 名	発表年月日	発 表 場 所
Lunar and Planetary Sciences Conference 39	2008年03月11日	Houston, TX, USA

Research Summary 研究要約

This research project focuses on origin and alteration of enstatite (EH) chondrites and refractory inclusions (CAIs) in carbonaceous chondrites. For both the EH chondrites and CAIs, research goals are to constrain: (1) initial crystallization conditions; (2) elemental changes that occurred during alteration and metamorphism; (3) the setting in which alteration occurred. The main analytical techniques are thin section petrography, and imaging and elemental analyses by electron probe micro-analysis. Cathodoluminescence imaging and laser Raman spectroscopy also are used. Isotope analyses by secondary ion mass spectroscopy are conducted in collaboration with other laboratories.

The following data regarding CAIs from CV3 chondrites were collected: identification of secondary minerals, textures and mineral modes in coarse-grained CAIs from Allende; mapping of spinel and melilite composition in CAIs from both Allende and Efremovka; Al-Mg isotopic data from Allende CAIs; O-isotope imaging in CAIs from Acfer 094. A suite of EH chondrites of varying metamorphic grade were examined for comparison of: chondrule types and textures; silica polymorphs; compositional variations in olivine, pyroxene, Fe-Ni-metal and troilite.

Most mineral alteration of Allende CAIs and elemental alteration of Efremovka CAIs is extensive near CAI boundaries with matrix. This correlation suggests that most alteration of these CAIs occurred in the parent body setting. However, subtle variations in Na in melilite and anorthite and Al-Mg isotopic data indicate that some alteration events preceded parent body formation. Likewise, a ^{16}O-rich rim on an Acfer 094 CAI formed in the nebular setting.

Variations in chondrule texture, silica polymorphs, and mineral compositions indicate that ALHA81189 is a primitive EH3; greater equilibration in other EH3 chondrites is attributed to more extensive heating during chondrule formation (not parent body metamorphism). Iron was transferred from mafic silicates to sulfides and metal during EH3 metamorphism; but silicates, sulfides and metallic minerals underwent variable re-equilibration during metamorphic cooling.

本研究において，我々はエンスタタイトコンドライトとCVコンドライト中における粗粒難揮発性包有物（CAIs）において，次の4つについて調べた．(1)結晶化の初期条件，(2)変質と変成による再結晶化中に起きた元素変化，(3)再結晶化中に起きた化学反応，(4)変質発生の状態薄片の顕微鏡写真と電子顕微鏡による元素分析と，補足的に、カソードルミネッセンスのイメージ分析とレーザーラマン分光を行った．　更に，同位体分析を他研究室の質量分析器を用いて共同で行った．
CV3コンドライトのCAIsにおいて，次の4つのデータを得た．(1)アエンデ隕石の粗粒CAIs中の2次鉱物の判別，組成の特徴，構成鉱物の面積比率　(2)アエンデとエフレモフカ隕石のCAIsにおけるスピネルとメリライトの組成変化　(3)アエンデ隕石のCAIsの初期鉱物と2次鉱物のAl-Mg同位体組成　(4)Acfer 094隕石のCAIsにおける組成と酸素同位体更に，様々な変成度を持つエンスタタイトコンドライトについて，次の3つのデータを得た．(1)コンドリュールの特徴と組成　(2)シリカの存在と多形　(3)橄欖石，輝石，金属鉄及びFeSの組成変化アエンデ隕石のCAIsの鉱物変質とエフレモフカ隕石のCAIsの元素変質は，CAI表面で大きく表面の変質度が大きいCAIsは内部も大きく変成している．
故に，CAIsの変質は母体内で起こったとされそうである．　しかし，メリライトにあるNaの微小な幅，灰長石のNaとMg，Al-Mg同位体組成は，変質が母体形成よりも先に起こったことを示し，Acfer094にある16Oが豊富なCAIの縁は星雲内で再結晶化して形成したと考えられる．　また，コンドリュールの組成，シリカの多形，鉱物組成から，ALHA81189が最も始原的なエンスタタイトコンドライトであることが分かった．　他のEH3コンドライトは，コンドリュール形成時により加熱されているようだ．　鉄はEH3の変成時に珪酸塩鉱物から硫化物や金属に移動したのだが，珪酸塩，硫化物，金属鉱物は変成中において様々な再平衡を経験したようである．

Refractory Inclusion and Enstatite Chondrite Alteration Processes

T.J. Fagan 鉱（フェイガン　ティモシー　ジェイ）

早稲田大学、教育学部地球科学教室

〒１６９－８０５０東京都新宿区西早稲田１－６－１

Department of Earth Sciences, Waseda University, 1-6-1 Nishiwaseda, Shinjuku, Tokyo 169-8050, Japan (fagan@waseda.jp)

Table of Contents

Introduction

The general motivation for this project is to understand the alteration and metamorphism in chondritic meteorites. In order to determine the alteration/metamorphic histories of these rocks, it is necessary also to establish the processes, timing and physical conditions of initial formation. Taken together, these goals represent entire fields of study within meteoritics and cosmochemistry, and encompass the work of several laboratories, analytical approaches and mult-year projects. Thus it is necessary to specialize within this general research theme to identify project goals that are attainable on relatively short time scales and meet the analytical limitations of a given laboratory.

This study is limited to the alteration/metamorphic histories of enstatite chondrites and refractory inclusions in carbonaceous chondrites; however, even with this limitation, this topic is too broad for a two-year project of a single laboratory. The main rocks of interest were limited further to EH chondrites and refractory inclusions in CV chondrites and in the relatively unmetamorphosed carbonaceous chondrite Acfer 094.

Refractory inclusions and enstatite chondrites are distinct rocks, but they share similar questions regarding petrogenesis and can be studied using similar analytical approaches. Similar questions include: (1) were these rocks affected by multiple "alteration/metamorphism" events? (2) to what extent did "alteration/metamorphism" occur in the nebular setting vs. the parent body setting? (3) to what extent was alteration/metamorphism a closed-system process? (4) which elements were transferred to and from these rocks during alteration? Furthermore, refractory inclusions were affected by isotopic, elemental and mineralogic alteration: were these types of alteration linked, or did they occur independently? A parallel question regarding enstatite chondrites considers the main mineral groups, silicates, metals and sulfides: were these groups altered and recrystallized in isolation, or was matter transferred between these mineral groups during alteration/metamorphism?

Refractory inclusions and enstatite chondrites can also be studied using similar analytical techniques. Most previous studies of refractory inclusions (also known as Ca-Al-rich inclusions or CAIs) have focused on primary minerals, thus basic data concerning the identity, abundance and textural occurrence of secondary minerals have not been established. Likewise, although some data have been presented on modes of enstatite chondrites, fundamental observations concerning chondrule textures, relationships between chondrules and "matrix" in enstatite chondrites remain poorly constrained. Also, detailed correlations between textural setting and elemental and isotopic composition remain surprisingly scarce in CAIs; yet such correlations must be established if we are to determine the general petrologic history of CAIs and chondrites in general.

As a part of this general effort, this study focused on establishing fundamental petrologic data on secondary and primary mineralogy, textures and elemental compositions in a suite of EH chondrites and CAIs from carbonaceous chondrites. Samples were selected to compare: a range of metamorphic grade in EH chondrites; CAI types from the CV3 Allende; CAIs from the oxidized CV3 Allende and reduced CV3 Efremovka; and CAIs from the unmetamorphosed carbonaceous chondrite Acfer 094 with CAIs from metamorphosed CV3 chondrites. The data are based on thin section petrography, back-scattered electron (BSE) and elemental imaging, and quantitative

electron probe micro-analysis (EPMA). Additional analyses conducted at Waseda University include laser-Raman spectroscopy to identify polymorphs of silica in enstatite chondrites, and cathodoluminescence (CL) imaging of anorthite in CAIs. The work conducted at Waseda has led to secondary ion mass spectroscopy (SIMS) analyses for Al-Mg isotopes (Arizona State University, USA) and O isotopes (Hokkaido University); SIMS analyses at Hokkaido University are scheduled for June 2008, and additional SIMS analyses are planned for later in 2008.

Work on CAIs focused on: (1) modes and textures of secondary phases in CAIs from Allende; (2) compositional variations in primary minerals in CAIs from both Allende and Efremovka; (3) Al-Mg isotope systematics of secondary phases in Allende CAIs; and (4) rimming textures and O-isotopic systematics of CAIs from Acfer 094. Project (1) was undertaken in order to determine the extent of replacement of some representative CAIs from Allende, to constrain the elemental fluxes that occurred during secondary mineral formation, and to compare the extent of alteration of different CAI types. The main goal of project (2) was to identify spatial patterns of elemental alteration in primary minerals in different CAIs from both Allende and Efremovka. The patterns identified in projects (1) and (2) were used to infer setting of alteration. Al-Mg isotopic data were used in project (3) to evaluate the timing and setting of formation of secondary minerals. O-isotopic data were combined with textural study in project (4) in order to identify fluctuations in oxygen isotopic setting during formation of CAIs in the solar nebula. Furthermore, because of the primitive (essentially unmetamorphosed) nature of Acfer 094, the data from project (4) serve as a reference point for interpreting results from the metamorphosed CV chondrites.

Secondary Minerals in Allende CAIs

Secondary minerals were identified and textures characterized in Allende CAIs 3655A (Type B1), 4022-1 (B2), 3898 (compact Type A, CTA) and 3529-47-1 (fluffy Type A, FTA). Modes of primary and secondary minerals were determined for Allende CAIs 3655A (Type B1), 4022-1 (B2), and 3529-47-1 (fluffy type A, FTA). (Due to limited sample availability, modes were not determined for CAI 3898.) Modes were determined using both manual counts on grid patterns superimposed on back-scattered electron (BSE) images, and an automated classification routine based on elemental mapping by EPMA. BSE images (Fig. 1) and elemental maps (Fig. 2) were collected using EPMA at Waseda University and the Smithsonian Institution. During the manual mode determination, several secondary minerals with similar grayscale appearance in BSE (nepheline, sodalite, Fe-bearing spinel, secondary anorthite) were grouped together as a single category, "BSE-dark". Subsequently, energy-dispersive spectroscopy (EDS, conducted at National Institute of Polar Research) was used to identify individual minerals in this category. A classification scheme in the ENVI (Environment for Visualization) software package was used to estimate mode from elemental maps.

Secondary minerals and textures. Both textural and compositional data were used to classify minerals as primary and secondary in the four Allende CAIs studied in detail (Table 2). Primary

minerals in these objects formed at high temperatures, and thus, they are poor in volatile elements such as Na and Cl. Furthermore, primary minerals show textural evidence of relatively early formation; such evidence includes euhedral crystal form, straight grain margins, coarse grain-size. Primary crystals may also show evidence of partial replacement by later phases. Minerals were classified as secondary if they showed textural evidence of late-stage formation by partial replacement of pre-existing minerals. Secondary minerals tend to be relatively fine grained, occur along margins, veins and pockets enclosed within primary minerals. The classification of minerals as "primary" and "secondary" does not imply that crystallization took place in only two stages. On the contrary, results from this study show that CAI crystallization and alteration was episodic.

Two texturally-distinct settings for alteration mineral assemblages were recognized in each of the four CAIs: (1) grossular-rich veins and relatively equant domains that we will refer to as "patches"; and (2) secondary anorthite+feldspathoid-bearing domains. Both types of alteration assemblages are commonly in contact with melilite and likely formed by replacement of that phase. The grossular-rich veins and patches occur mainly in the CAI interiors, whereas the secondary anorthite+feldspathoid alteration occurs mostly (but not exclusively) in a semi-continuous rim just inboard of the Wark-Lovering rim sequences around the CAIs. Much of the secondary anorthite has a lath-like texture (Fig. 3) and shows small, but consistent deviations from feldspar stoichiometry, with enrichments in Al, Fe and Mg that may be a result of beam overlap onto very fine-grained spinel or pyroxene. Less porous, more tabular secondary anorthite was identified in CAIs 4022-1 and 3898-2; this feldspar shows blue to white cathodoluminescence and is stoichiometric.

Although both types of secondary assemblage were identified in each of the four CAIs investigated in this study, the specific textures, mineral assemblages and relative abundances of grossular-rich vs. feldspar+feldspathoid-bearing domains vary among these CAIs and are described separately.

CAI 3655A (B1). The grossular-rich alteration domains in this CAI occur as equant patches in the CAI core and as veins along melilite grain boundaries in the CAI mantle. The grossular occurs as equant, anhedral grains less than 15 μm in diameter (Fig. 4A,B), and is intricately intergrown with fine-grained monticellite. Melilite immediately adjacent to the grossular-rich alteration domains contains abundant vacant pores. Wollastonite occurs with grossular and monticellite in alteration patches in the core of the CAI, but was not found in veins in the CAI mantle. The grossular-rich veins appear to have formed by pseudomorphic replacement of melilite along grain boundaries, cleavage traces, and cracks in melilite. Although the alteration patches in the core primarily replace melilite, serrated margins along neighboring primary anorthite grain boundaries suggest that some anorthite also might have decomposed during alteration (Fig. 4B).

Most of the secondary feldspar+feldspathoid-bearing alteration in 3655A is concentrated in an outer zone between the Wark-Lovering rim and the mantle melilite (Fig. 4C,D). The alteration patches and the rim domains are characterized by a consistent mineral sequence, with grossular occurring directly in contact with melilite, secondary anorthite mantling the grossular, and nepheline or sodalite exterior to the anorthite (Fig. 4D). Spinel in the alteration patches is generally Fe-bearing and commonly contains detectable Zn as well; secondary diopside is rare.

Grossular crystals may occur in the interior of rim alteration patches as well as along the fringe. As elsewhere, the secondary feldspar in these regions has an elongate lath-like shape (Fig. 4D).

CAI 4022-1 (B2). Grossular-bearing veins in CAI 4022-1 are similar to those observed in 3655A in that they are dominated by fine-grained (generally < 5 μm) intergrown grossular and monticellite, they occur throughout the CAI, and they commonly transect melilite crystals or occur along melilite crystal boundaries (Fig. 5A,B). Anorthite occurs instead of monticellite in some veins near the CAI margin. Secondary anorthite exhibits both lath-like and slightly coarser, more equant textures (Fig. 5B). Unlike the veins in 3655A, several grossular-rich veins in 4022-1 occur within primary anorthite crystals, apparently replacing the anorthite.

Secondary feldspar+feldspathoid-bearing alteration patches occur in the interior of CAI 4022-1 and they are in contact with all of the major primary minerals (Fig. 5C,D). Sodalite and nepheline in the interior of the alteration patches are for the most part separated from primary minerals by a discontinuous fringe of grossular. Similar to the feldspathoid-rich domains in CAIs 3655A, the feldspathoid alteration patches in the interior of 4022-1 include secondary anorthite; however, the anorthite does not occur as elongate laths, but forms coarser-grained, more equant, tabular crystals (Fig. 5D). Furthermore, this secondary anorthite does not form a concentric layer separating feldspathoids from the grossular fringe. Feldspathoids in the alteration patches are intergrown with elongate, fine (< 1 μm across) stringers of Fe-bearing spinel, and somewhat coarser (~ 5 μm across) equant crystals of high-Ca pyroxene with variable Mg/(Mg+Fe).

Feldspathoids also occur in the thin layer of alteration minerals just interior to the Wark-Lovering rim that forms the outer margin of CAI 4022. Similar to the feldspathoid-rich zone in CAI 3655A, a thin discontinuous fringe of fine-grained grossular occurs along the inner boundary of the alteration layer. The layer is characterized by fine-grained feldspathoids intergrown with laths of secondary feldspar and stringers of Fe-bearing spinel. Electron microprobe analyses of these phases rarely yield stoichiometric results, owing to the fine-grained and intergrown nature of the minerals.

CAI 3898 (Compact Type A). Secondary minerals in CAI 3898 are restricted mostly to the CAI margin, just interior to the Wark-Lovering rim sequence (Fig. 1C,2C). Grossular-bearing veins occur in CAI 3898, but are much less abundant than in the Type B CAIs, and are not found in the inner core of the CAI. Also, whereas the alteration veins in the Type B CAIs contain abundant monticellite in addition to grossular, the veins in 3898 consist almost entirely of grossular, with occasional secondary anorthite or feldspathoid (Fig. 6A,B). Monticellite and wollastonite were not identified in CAI 3898.

The secondary feldspar+feldspathoid assemblage occurs both in the wide continuous zone inboard of the Wark-Lovering diopside rim and in isolated patches enclosed by melilite near the CAI margin. Secondary minerals near the rim of 3898 exhibit essentially the same textural occurrence as observed in CAI 3655A: melilite is mantled by a discontinuous fringe of grossular; grossular is in contact with secondary lath-like anorthite, and nepheline and sodalite occur in the central portions of these alteration domains; some grossular crystals occur in the inner portions of alteration patches as well as along the fringing margins; Fe-bearing spinel occurs within the alteration patches (Fig. 6C,D). In rare cases, secondary feldspar is tabular and yields more stoichiometric electron microprobe analyses than the lath-like secondary feldspar.

CAI 3529-47-1 (Fluffy Type A). Secondary minerals in CAI 3529-47-1 form a much greater fraction of the whole CAI than in any of the others inclusions studied, and are dominated by the feldspar+feldspathoid assemblage (Figs. 1D, 2D). Similar to compact Type A CAI 3898-2 grossular-rich veins are rare; monticellite is absent. Within each of the nodules composing the CAI, secondary feldspar+feldspathoid-bearing domains occupy the irregular regions between the highly serrated melilite crystals and the Wark-Lovering rims (Fig. 7A,B). The melilite crystal margins are mantled by a discontinuous grossular fringe, which in turn is in contact with lath-like secondary anorthite. Grossular may occur in the interiors of altered domains as well as on the fringing margins. Nepheline and sodalite are concentrated away from the melilite. Iron-bearing spinel occurs as individual crystals generally < 2μm across and as thin strands of finer-grained crystals in contact with secondary feldspar and feldspathoids. Along broken nodule surfaces, the alteration minerals occur adjacent to inter-nodule matrix grains with no apparent reaction textures (Fig. 3).

Modes of Allende CAIs

Modal (volume) abundances of minerals are fundamental information for determining petrogenesis of any rock. Nonetheless, quantitative modes have rarely been reported for CAIs. This is due in part to the fine grain size of many minerals in CAIs and the difficulty in acquiring accurate modal data. In this study, quantitative modes were determined for three typical coarse-grained CAIs from Allende: 3655A (Type B1); 4022-1 (B2); and 3529-47-1 (fluffy Type A = FTA) using two methods. The first mode was determined from a BSE mosaic of the CAIs. A digital grid was lain on the BSE mosaic of each sample, and modes were determined by manually identifying the minerals at each node of the grid based on BSE-grayscale. Several secondary minerals, including nepheline, sodalite, secondary anorthite and Fe-bearing spinel have similar dark appearance in BSE; therefore, as a first step, these minerals were grouped together and counted as "BSE-dark". Afterward, an energy dispersive (EDS) spectrum was collected at each BSE-dark node to identify the mineralogy. Because of the fine grain size of the BSE-dark secondary minerals, several nodes fell on grain boundaries; at these points fractions of the minerals identified were counted toward the mode.

Because each node of the grid was counted manually, textures could also be considered during determination of the mode. Grossular veins and patches in the interiors of CAIs were classified separately from rim grossular, which occurs as fine grains fringing melilite near CAI rims. Similarly, primary anorthite was also distinguished from secondary anorthite, and Mg-rich spinel, which is enclosed within primary minerals, was distinguished from Fe-bearing spinel, which occurs adjacent to secondary minerals.

The second method of mode determination was an automated routine based on elemental x-ray maps of the CAIs. A higher number of node points can be calculated using this approach; however, textural distinctions cannot be made, and mixed points can be difficult to identify.

In spite of these differences, modes determined by the two methods are similar for most minerals in the three CAIs examined (Table 3). Some discrepancies between the two methods occur. For example, the automated method indicates higher abundances of nepheline and sodalite

in the Type B CAIs. This is probably due to the similarity in BSE grayscale of these minerals and feldspar, and in this case, the automated results are probably more accurate than the grid counting results. Nonetheless, some general observations can be made from the data.

The modal data show that all three of these CAIs have undergone extensive mineralogic alteration. Secondary minerals comprise 20% of the mode of 3655A (B1), 30% of 4022-1 (B2) and 60% of 3529-47-1 (FTA) (Table 3). These results indicate extensive recrystallization of primary CAI minerals during subsequent thermal events. Alteration minerals are most abundant in CAI 3529-47-1, which has the highest surface area. Greater surface area may have favored alteration reactions because of greater fluxes of matter across primary mineral boundaries. In any case, the high abundance of secondary minerals in all of the CAIs, and particularly the presence of feldspathoids, indicate significant transfers of Na and Cl and in all likelihood other elements between primary CAIs and neighboring materials.

Compositional Variations in Primary CAI minerals from Allende and Efremovka

FeO contents of spinel and minor concentrations of Na and Fe in melilite were used as monitors of elemental alteration for one fine-grained and one coarse-grained CAI from Efremovka (Figs. 8 and 9) and a type B2 CAI from Allende (Figs. 1B and 2B). Concentrations of FeO in spinel show correlate with proximity to CAI margins for both of the Efremovka CAIs: fine-grained FGI-12 (Figs. 10 and 11A) and coarse-grained CGI-10 (Fig. 11B). One relatively FeO-rich spinel grain occurs in the interior of FGI-12, but this grain occurs adjacent to a large crack filled with matrix material. The correlation between FeO-content of spinel and proximity to matrix material in both Efremovka CAIs suggests that FeO-alteration of spinel occurred after the CAIs were brought into contact with matrix material in the parent body setting.

Melilite in Type B CAIs from Allende and Efremovka show similar trends of increasing FeO-content with proximity to CAI margins. Melilite Na-concentrations in Efremovka CGI-10 also increase with proximity to the CAI margin; however, Allende CAI 4022-1 (Type B2) has melilite with elevated Na2O-contents throughout the CAI interior. These results indicate that: (1) alteration was more intense in Allende than in Efremovka; or (2) alteration was more intense in Type B2 CAIs than in B1's; or (3) Na-alteration of melilite was decoupled from Fe-alteration of melilite; or (4) some combination of (1) (2) and (3).

Al-Mg Isotopic Data from Allende CAIs

Al-Mg isotopic data confirm the suggestion based on petrologic work that alteration of Allende CAIs took place in multiple stages. Most secondary minerals have Al-Mg isotope systematics indicating crystallization well after primary minerals (Fig. 12). Primary feldspar in CAI 3655A was closed to isotopic resetting after crystallization, and secondary minerals formed in the absence of significant "live ^{26}Al" (Fig. 12A,B). In contrast, primary feldspar in 4022-1 (B2) exhibits variable isotopic resetting after crystallization and some secondary grossular may have formed at

nearly the same time as primary minerals (Fig. 12C,D). Secondary grossular in 3898-2 (CTA) also appears to have formed at an early, nebular stage (Fig. 12E,F). Most secondary minerals in 3529-47-1 formed with some live ^{26}Al, but several 100,000 years after crystallization of primary minerals (Fig. 12 G,H); this event may have coincided with chondrule formation or it may have occurred during parent body heating.

In any case, the analyzed Allende CAIs show different Al-Mg isotope patterns. Implications are that: (1) the CAIs had different thermal histories prior to formation of the Allende parent body and (2) parent body metamorphism was not intense enough to re-set Al-Mg isotope systematics in CAIs.

O Isotopic Data from Acfer 094 CAIs

Acfer 094 is an unclassified, unusually primitive carbonaceous chondrite. Because of the primitive (relatively unmetamorphosed, unaltered) nature of this meteorite, CAIs in Acfer 094 have undergone minimal parent body heating and thus preserve the nebular history of petrogenesis. Many CAIs from this meteorite show a concentric texture, with more refractory minerals in cores and somewhat less refractory mantles. In some cases, the cores and mantles show simple mantling textures (Fig. 13 A,B); in contrast, other CAIs show a textural discontinuity, where pre-existing melilite has been partially transformed to anorthite which is, in turn, rimmed by diopside (Fig. 13 C,D).

Isotopic imaging of the CAI shown in Fig. 13 C,D was conducted in collaboration with colleagues at University of Hokkaido. Previously collected spot analyses indicated that the mantling melilite (Fig. 13 A,B) shares ^{16}O-rich compositions with core minerals; these compositions are characteristic of primary minerals in CAIs from many chondrite groups. Previous analyses suggested that the more texturally CAI (Fig. 13 C,D) has more complex isotopic systematics. Isotopic imaging confirms these results, indicating that the diopside-rich rim is ^{16}O-poor whereas the interior of RO-64 (Fig. 13 C,D) is ^{16}O-rich (Fig. 14). This variation in O isotopes, mineralogy and texture indicates that this CAI formed by high-temperature crystallization in 16O-rich setting, followed by resorption of melilite, followed by formation of the diopside rim in a 16O-poor setting. All of these events preceded parent body formation. Formation of the diopside rim may have coincided with an episode of chondrule formation.

Chondrule Types, Occurrence of Silica and Setting of Equilibration in EH Chondrites

Chondrule types and textures and the occurrence of silica were determined for a number of EH chondrites in order to evaluate the timing of equilibration processes (see Table 1). Silica maps (from X-ray elemental mapping) of polished thin sections (Fig. 15) were combined with multi-element maps, BSE imaging and petrographic microscope observations to describe chondrule textures.

The occurrence and speciation of silica appears to be critical for interpreting the origin and metamorphism of EH chondrites. Silica occurs as spherules and is abundant as rims on chondrules in the primitive EH3 ALHA81189 (Fig. 16A,B). Fragmented chondrules, many with silica-rich rims (Fig. 16C), were identified in all EH3 chondrites. In contrast to the EH3's, St. Marks (EH5) is characterized by coarse crystals of quartz (Fig. 16D).

Variations in chondrule textures and silica occurrence highlight the primitive nature of EH3 ALHA81189. ALHA81189 has high proportions of porphyritic olivine + pyroxene (POP) chondrules and whole (unfragmented) chondrules relative to other EH3 chondrites (Fig. 17). Furthermore silica-rich rims are much more abundant on both POP and porphyritic pyroxene (PP) chondrules in ALHA81189 than in other EH chondrites.

These observations indicate that ALHA81189 has experienced less progress on the equilibration reaction olivine + quartz → pyroxene than other EH3 chondrites. Furthermore, the differences in chondrule textures indicate that ALHA81189 is likely not a metamorphic precursor of the other EH3 chondrites. Lower chondrule fragmentation and greater abundance of silica-rich rims and POP mineral textures indicate that ALHA81189 chondrules are more primitive than the chondrules in other groups. Thus it is inferred that the other EH3 chondrites examined in this study experienced more equilibration during chondrule formation. These differences in equilibration among the EH3's are not due to parent body metamorphism.

Distributions of Minor Elements in EH Minerals: Implications for Metamorphic Reactions

Variations in Fe/(Fe+Mg) in olivine and pyroxene and Ti in troilite support the interpretation that ELHA81189 is a particularly primitive EH3 chondrite. The range of Fe/(Fe+Mg) in mafic silicates in ALHA81189 is generally similar to the EH3 ALH 84170; however, some extremely Mg-poor pyroxene is found in ALH 84170, whereas all analyzed pyroxene in ALHA81189 contains detectable Fe (Fig. 18A). This suggests that silicates in ALHA81189 formed under slightly higher oxygen fugacities than in other EH3 chondrites. Troilite in ALHA81189 has lower Ti concentrations than in other EH chondrites, also indicating the distinctive origin of this meteorite (Fig. 18B). In contrast, however, Si contents in Fe-Ni-metal are similar to other EH3 chondrites (Fig. 18C), indicating suggesting that silicates, sulfides and metallic minerals in these meteorites formed under different conditions or equilibrated at different times.

Table 1. Main samples used in this study.

Name	Type, host (CAIs)	Sample owner
enstatite chondrites		
ALHA81189	EH3	Smithsonian Institution
MET 01018	EH3	Smithsonian Institution
ALH 84170	EH3	Smithsonian Institution
PCA 82518	EH3	Smithsonian Institution
St. Marks	EH5	Smithsonian Institution
Sahara 97096	EH3	Waseda University
Ca-Al-rich inclusions		
CGI-10	B1, Efremovka	J. Goswami
FGI-12	fine-grained, Efremovka	J. Goswami
3655A	B1, Allende	Smithsonian Institution
4022-1	B2, Allende	Smithsonian Institution
3898	compact type A, Allende	Smithsonian Institution
3529-47	fluffy type A, Allende	Smithsonian Institution
several CAIs	diverse types, Acfer 094	D. Weber, A. Greshake

Note: Efremovka is a reduced CV3 chondrite; Allende is an oxidized CV3; Acfer 094 is an unmetamorphosed carbonaceous chondrite.

Table 2. Main minerals identified in four Allende CAIs.

Name	General Formula	Mineral Group
primary minerals		
anorthite	$CaAl_2Si_2O_8$	feldspar
diopside	$CaMgSi_2O_6$	pyroxene
fassaite	$Ca(Mg,Al,Ti)(Al,Si)_2O_6$	pyroxene
hibonite	$Ca(Al,Mg,Ti)_{12}O_{19}$	oxide
melilite (Ge-Åk)	$Ca_2Al_2SiO_7$-$Ca_2MgSi_2O_7$	sorosilicate
spinel	$MgAl_2O_4$	oxide
perovskite	$CaTiO_3$	oxide
secondary minerals		
anorthite	$CaAl_2Si_2O_8$	feldspar
Fe-diopside	$Ca(Fe,Mg)Si_2O_6$	pyroxene
Fe-spinel	$(Fe,Mg)Al_2O_4$	oxide
grossular	$Ca_3Al_2Si_3O_{12}$	garnet
monticellite	CaMgSiO4	nesosilicate
nepheline	$(K,Na)_2Al_2Si_2O_8$	feldspathoid
sodalite	$Na_4Al_3Si_3O_{12}Cl$	feldspathoid
wollastonite	$CaSiO_3$	pyroxenoid

Note: The naturally-occuring minerals are solid solutions with variations from the tabulated formulae. Gehlenite and åkermanite end-members of the melilite solid solution are shown. Anorthite occurs as both a primary and a secondary mineral.

Table 3. Modes of secondary and primary minerals in CAIs from Allende.

	3655A		4022-1		3529-47-1	
	grid	auto	grid	auto	grid	auto
Mineral						
melilite	28.8	35.8	24.9	25.0	15.4	25.5
total spinel	21.4	19.6	16.3	6.0	22.3	4.8
fassaite	23.2	22.3	19.3	17.3	0.15	0
total anorthite	5.0	4.9	9.2	5.4	21.5	27.0
total grossular	20.7	16.4	25.2	29.4	12.5	9.8
perovskite	0.33	0	0.2	0.04	0.6	0.53
hibonite	0.11	0.28	0.0	0.0	0.0	0.24
diopside	0.33	0	2.2	0.77	18.1	19.4
metal, sulfide	0.0	0.0	0.0	0.24	0.0	0.0
nepheline	0.15	0.29	1.4	8.9	5.7	3.1
sodalite	0.09	0.05	0.7	7.0	1.5	9.6
Ca-Cl mineral	0.0	0.4	0.0	0.0	0.0	0.0
Grid-counting only						
Fe-spinel	0.72		2.2		17.9	
Mg-spinel	20.7		14.1		4.5	
primary anorthite	4.0		7.0		0.0	
secondary anorthite	0.95		2.2		21.5	
rim grossular	0.66		4.4		6.3	
vein grossular	20.0		20.8		6.2	
total	100	100	100	100	100	100
unclassified	0	11.9	0.54	18.3	2.2	4.5

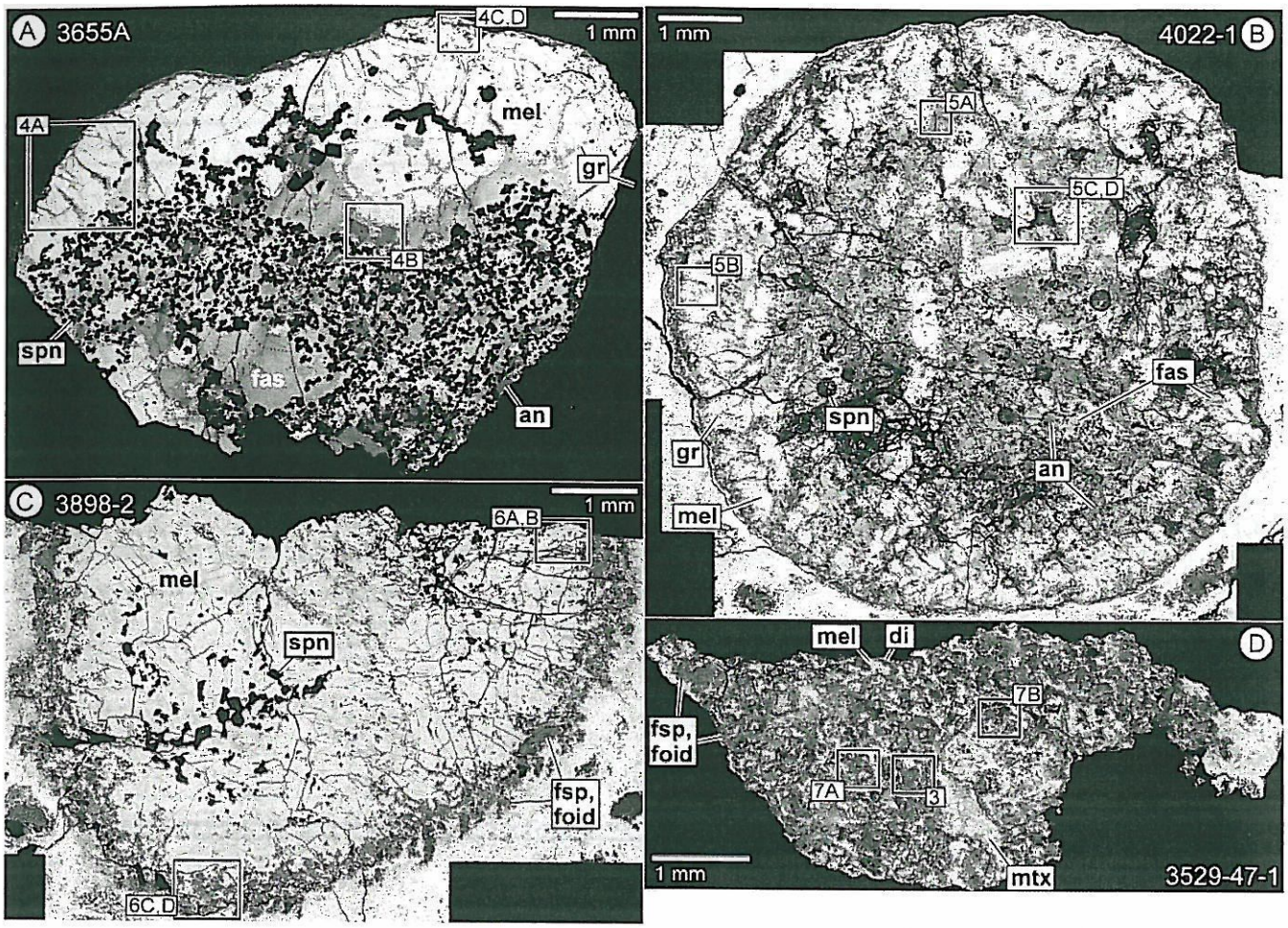

Fig. 1. Backscattered electron (BSE) mosaics of: (A) Type B1 CAI 3655A; (B) Type B2 CAI 4022-1; (C) Compact Type A CAI 3898-2; and (D) Fluffy Type A CAI 3529-47-1. Compare these figures with false-color elemental maps in Fig. 2. Mineral abbreviations here and in subsequent images: an = primary anorthite; di = diopside; fas = fassaite; Fe-sp = Fe-bearing spinel; foid = feldspathoid; fsp = secondary feldspar; gr = grossular; mel = melilite; mon = monticellite; mtx = internodule matrix; ne = nepheline; pv = perovskite; sod = sodalite; spn = spinel; wo = wollastonite.

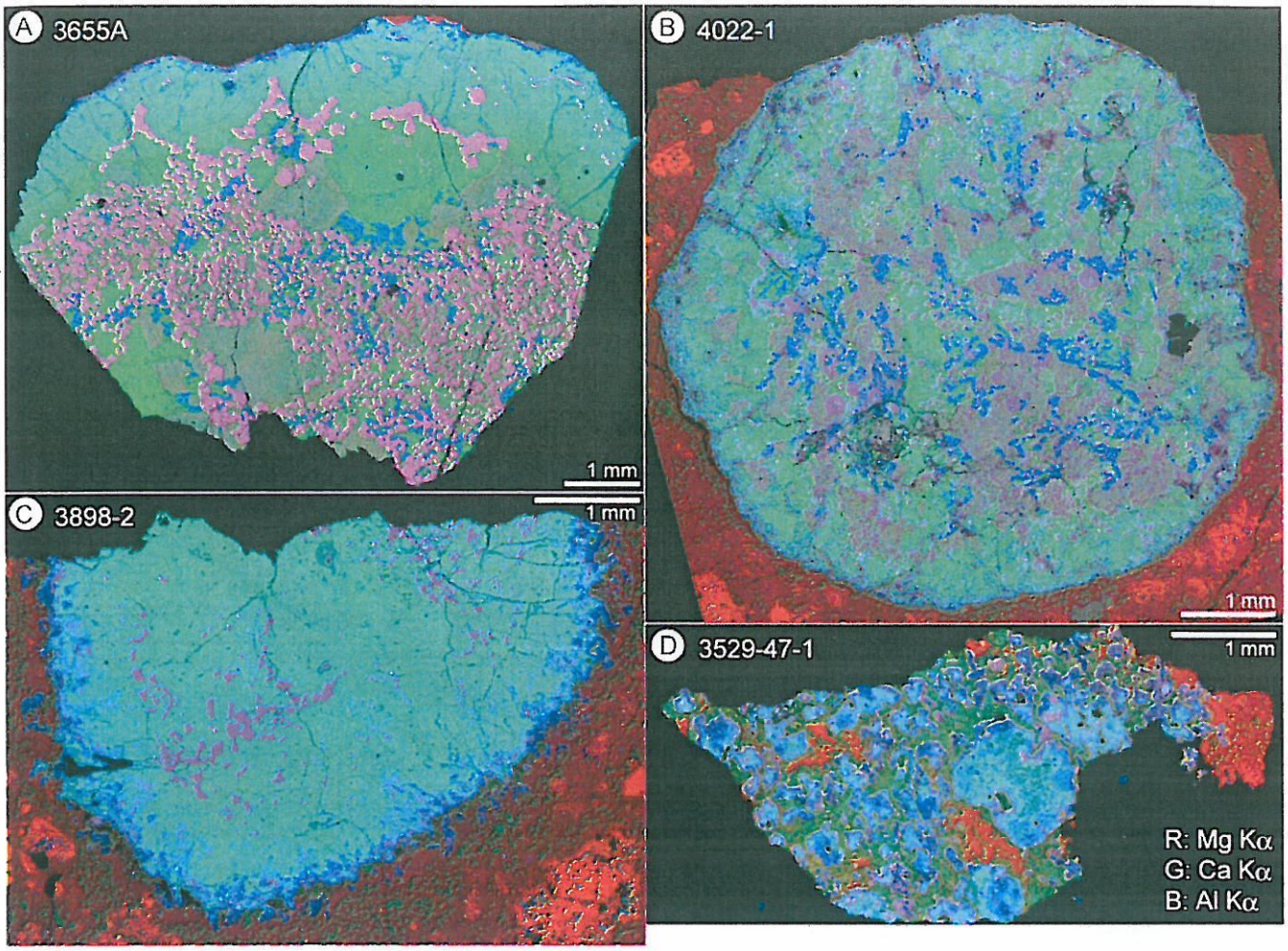

Fig. 2. False-color elemental maps of four CAIs from Allende: red = Mg Kα; green = Ca Kα; blue = Al Kα. See Fig. 1 for mineral identification.

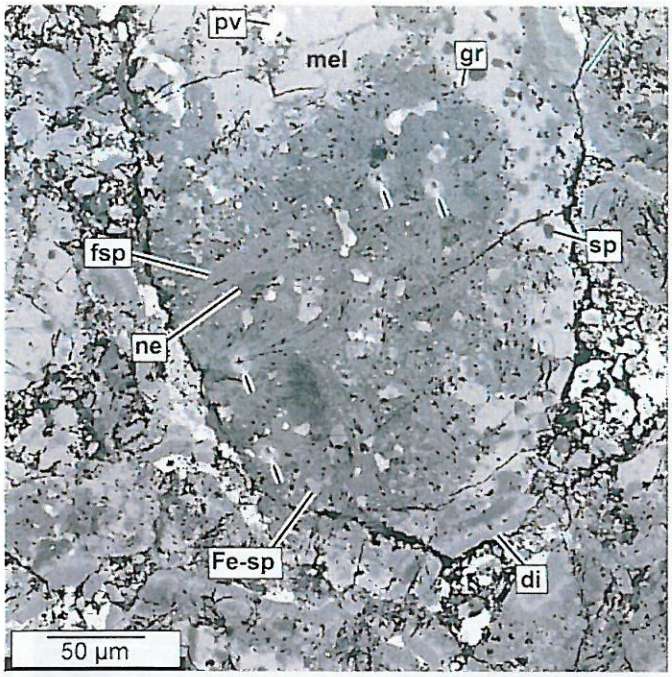

Figure 3. BSE image of Fluffy Type A nodule with broken surfaces in contact with internodule matrix. BSE image is overlain on an SE image with throughput adjusted so that compositional contrasts are shown in BSE and pits excavated during SIMS analyses are highlighted by SE. Craters sputtered during SIMS analyses are denoted by arrows; mineral abbreviations as in Fig. 1.

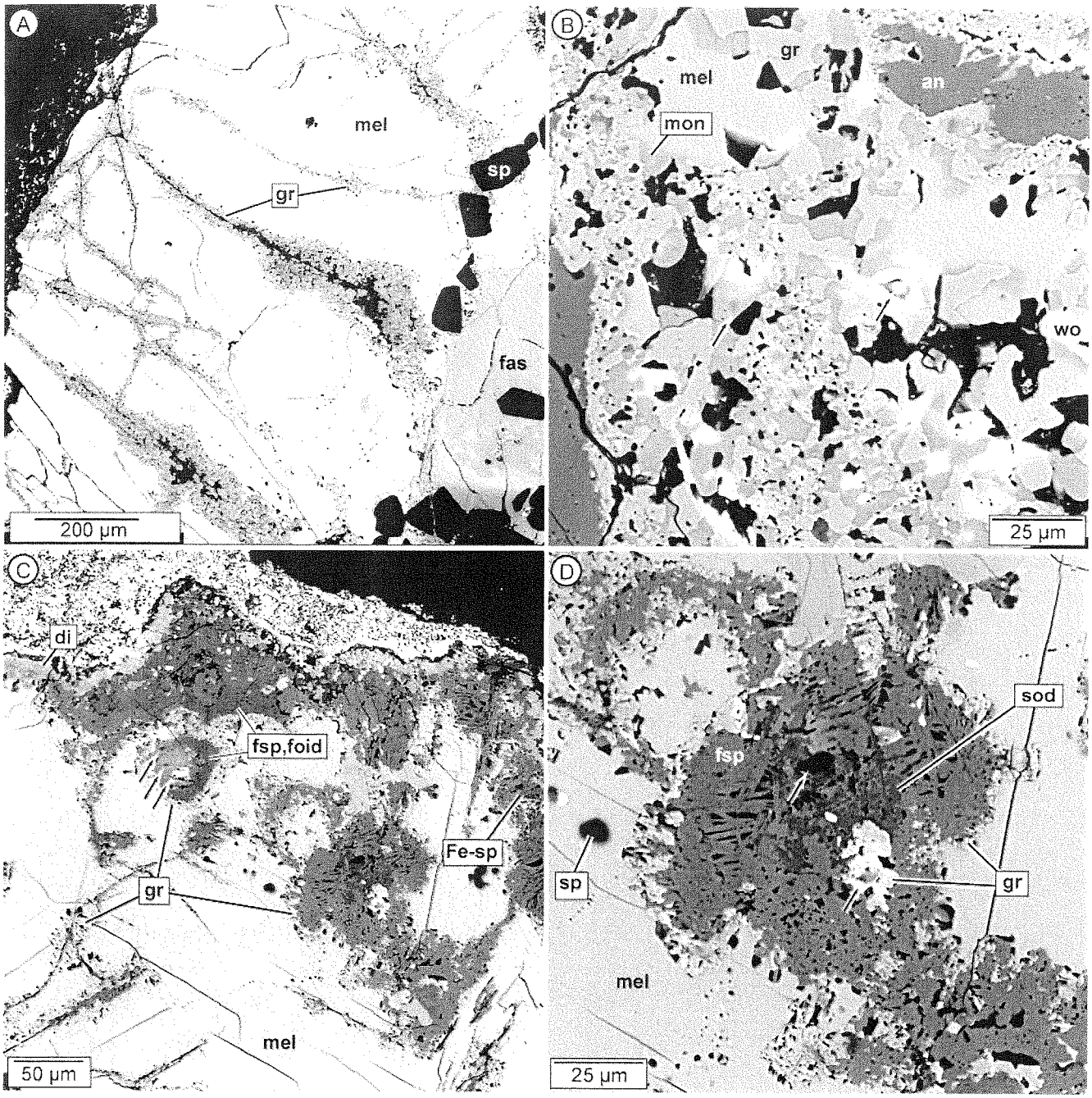

Fig. 4. BSE image (A) and BSE/SE overlays (B, C, D) of Type B1 CAI 3655A. (A) Grossular-rich veins in melilite-rich mantle of CAI. (B) Extensively pseudomorphed melilite from core of CAI. (C) Altered domains near rim of CAI. Very bright material in upper part of image consists of Allende matrix. Diopside along CAI margin is from the altered Wark-Lovering rim. Secondary minerals occur adjacent to the Wark-Lovering rim and in alteration patches enclosed by melilite near the CAI margin. (D) Detailed image from (C) of feldspathoid alteration patch. Note the presence of grossular along the rim and in the center of the alteration patch, the lath-like texture of secondary feldspar and the occurrence of sodalite in the center of the patch. Craters sputtered during SIMS analyses are denoted by arrows; mineral abbreviations as in Fig. 1.

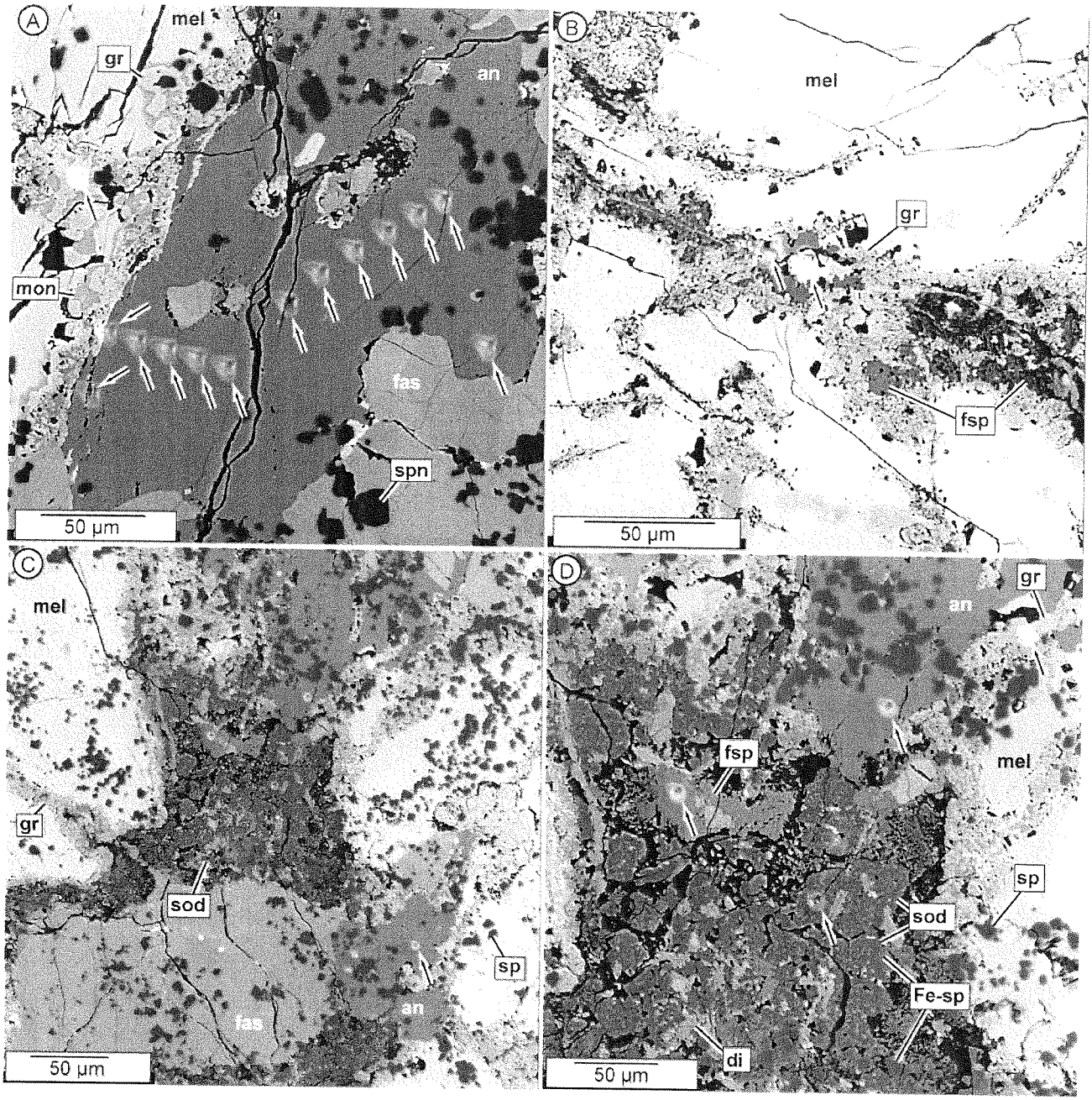

Fig. 5. BSE/SE overlay images of Type B2 CAI 4022-1. Craters sputtered during SIMS analyses are denoted by arrows. (A) Intersecting grossular-bearing veins in interior of CAI, and SIMS analyses in primary anorthite (center) and grossular (upper left). Arrows from lower right to upper left denote analyses considered representative of target minerals. Arrows pointing from upper right to lower left show SIMS craters on primary/secondary mineral boundaries or on mineralized cracks; these analyses were not considered in our interpretation of alteration history. (B) Grossular-bearing vein with secondary anorthite near margin of CAI. Some secondary anorthite has lath-like texture; some (center) has more equant, coarse-grained form. (C) Feldspathoid-bearing alteration patch, grossular-bearing veins and primary minerals in interior of CAI. (D) Detailed view of alteration patch shown in (C). Mineral abbreviations as in Fig. 1.

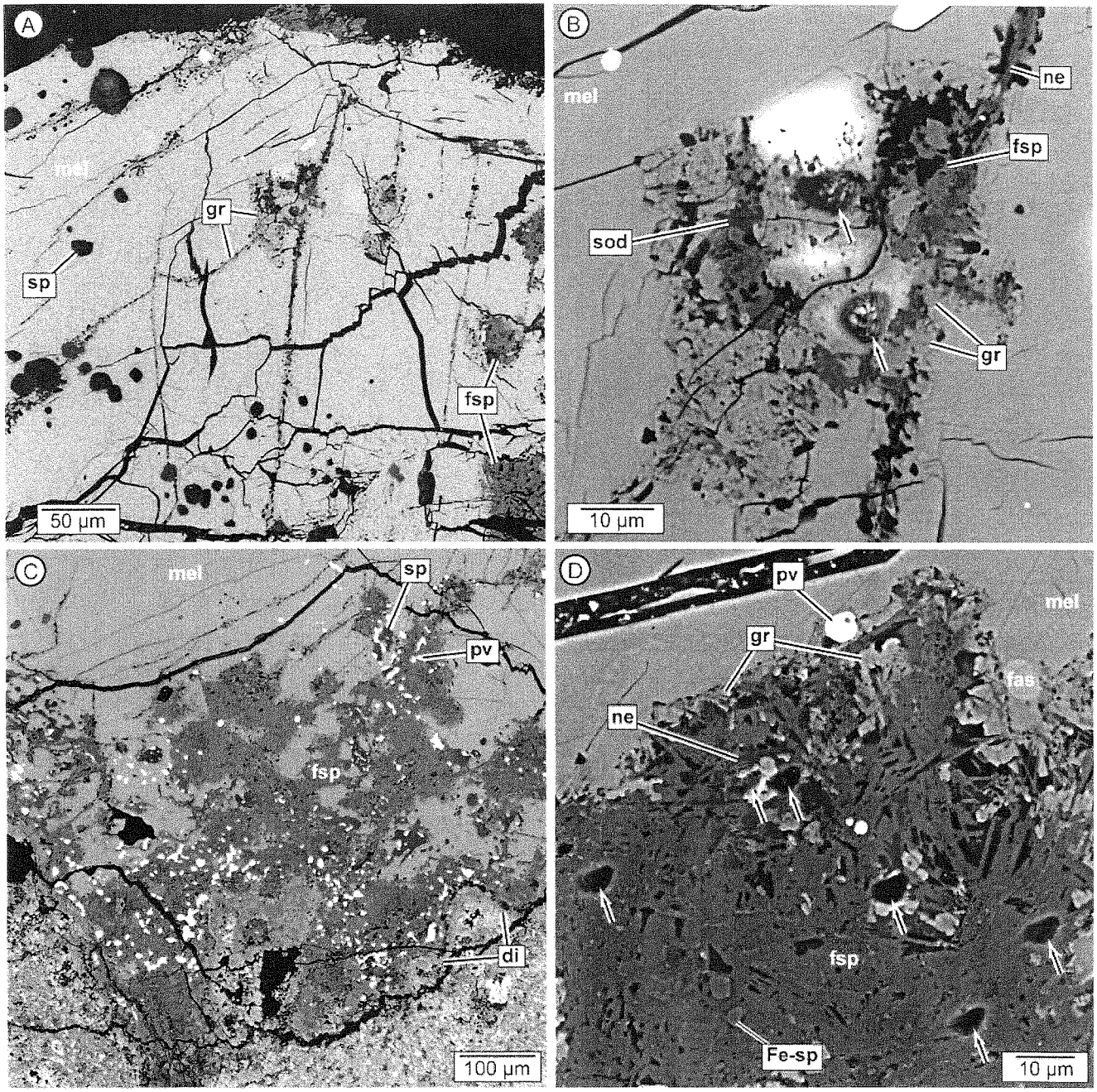

Fig. 6. BSE images of Compact Type A CAI 3898-2. (A) Grossular-bearing veins in interior of CAI. Note the paucity of veins compared with the Type B CAIs. (B) Detailed image from center of (A) showing thick portion of vein and pits excavated by SIMS. (C) Altered domains near rim of CAI. Bright material in lower part of image consists of Allende matrix. Diopside along CAI margin is from the altered Wark-Lovering rim. Secondary minerals occur adjacent to the Wark-Lovering rim and in alteration patches enclosed by melilite near the CAI margin. (D) Detailed image from (C) showing portion of a feldspathoid alteration patch. Note grossular along the fringe and in the center of the alteration patch, the lath-like texture of secondary feldspar and the occurrence of nepheline in the interior of the patch. Craters sputtered during SIMS analyses are denoted by arrows in (B) and (D). Mineral abbreviations as in Fig. 1.

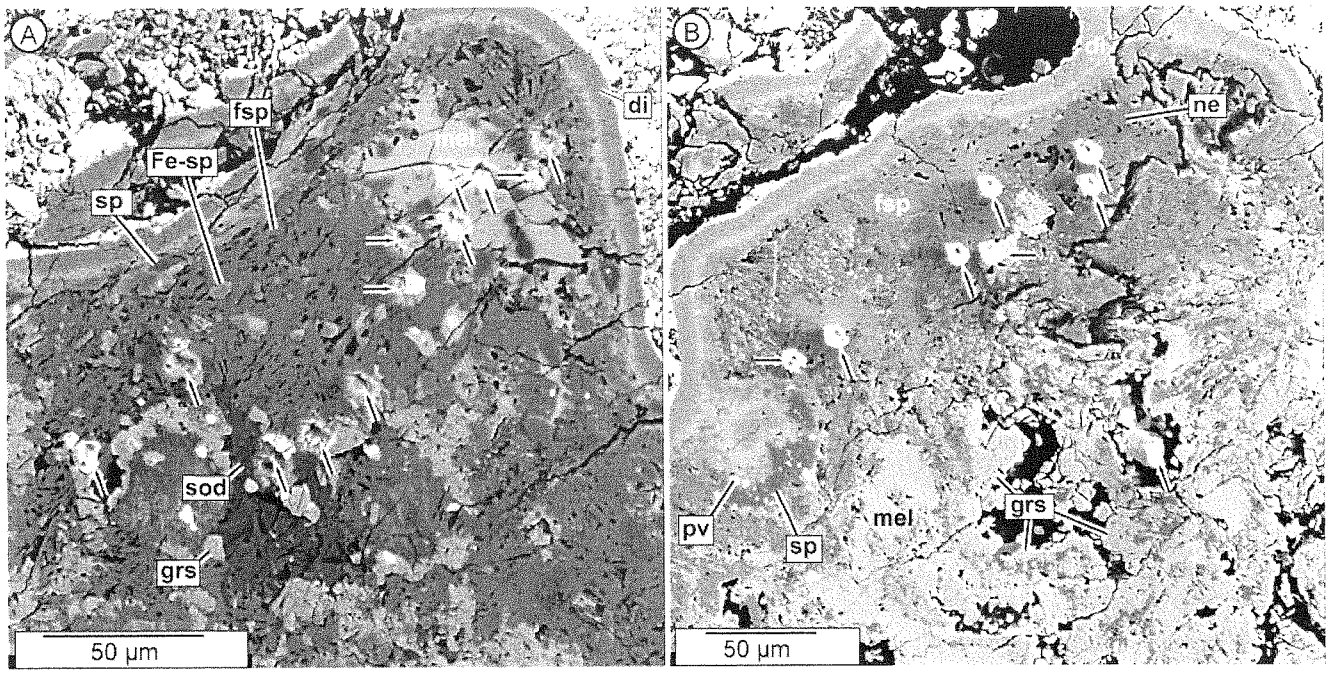

Fig. 7. BSE/SE overlay images of Fluffy Type A CAI 3529-47-1. (A) Original melilite has been extensively replaced by secondary feldspar and feldspathoids. Note the lath-like texture of secondary feldspar, corroded crystal boundaries of melilite and discontinuous grossular fringe on melilite. (B) Grossular occurs as fringe along melilite grain boundaries, as shown previously, and within interior of melilite. Craters sputtered during SIMS analyses are denoted by arrows. Arrows from lower right to upper left denote analyses considered representative of target minerals. Arrows pointing horizontally show SIMS craters on mineral boundaries; these analyses were not considered in our interpretation of alteration history. Mineral abbreviations as in Fig. 1.

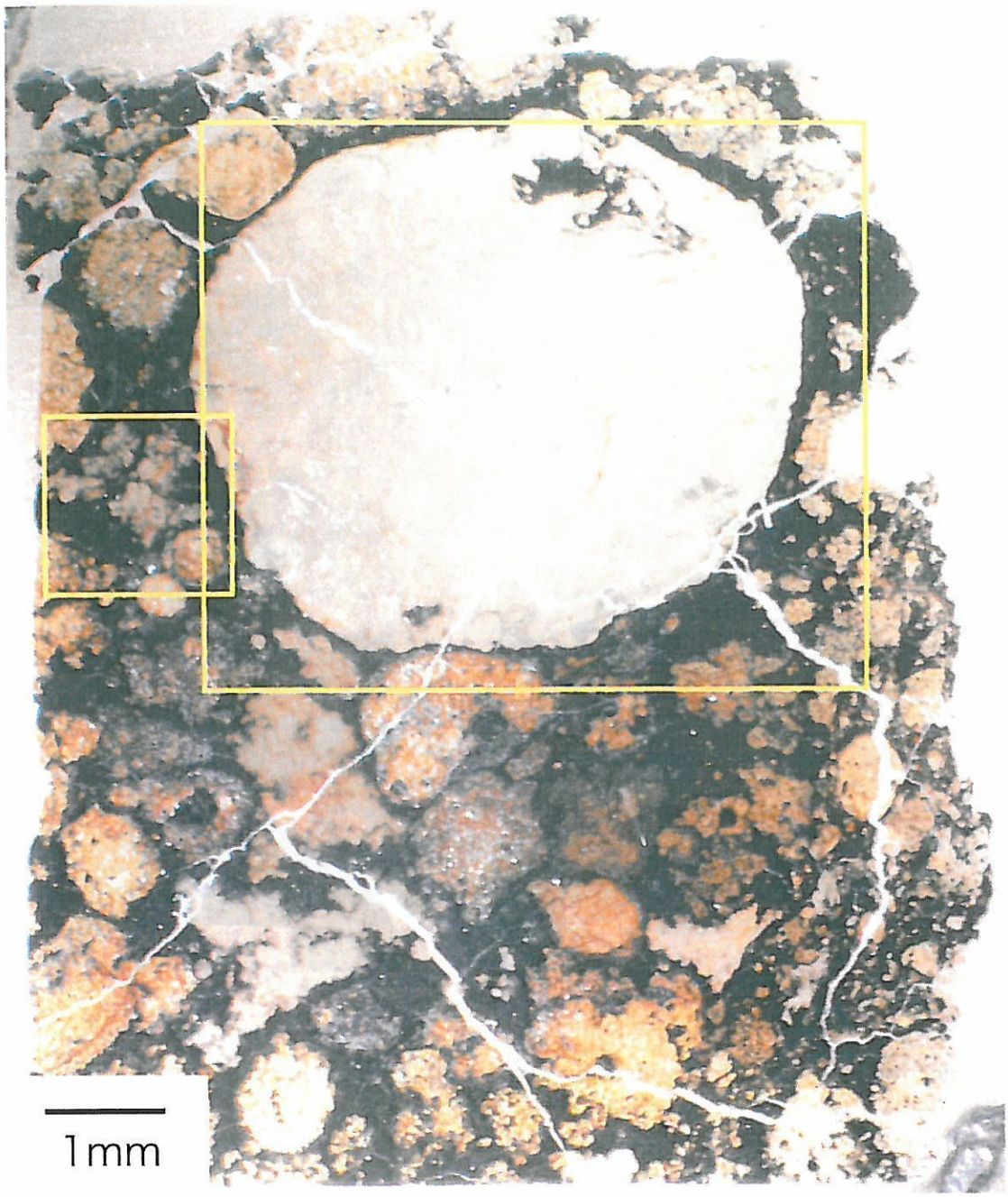

Fig. 8. Scanned image of Efremovka polished thin section showing coarse-grained type 1 CAI (CGI-10, outlined by large yellow box) and fine-grained spinel-rich CAI (FGI-12, outlined by small yellow box; see Figs. 9 and 10.

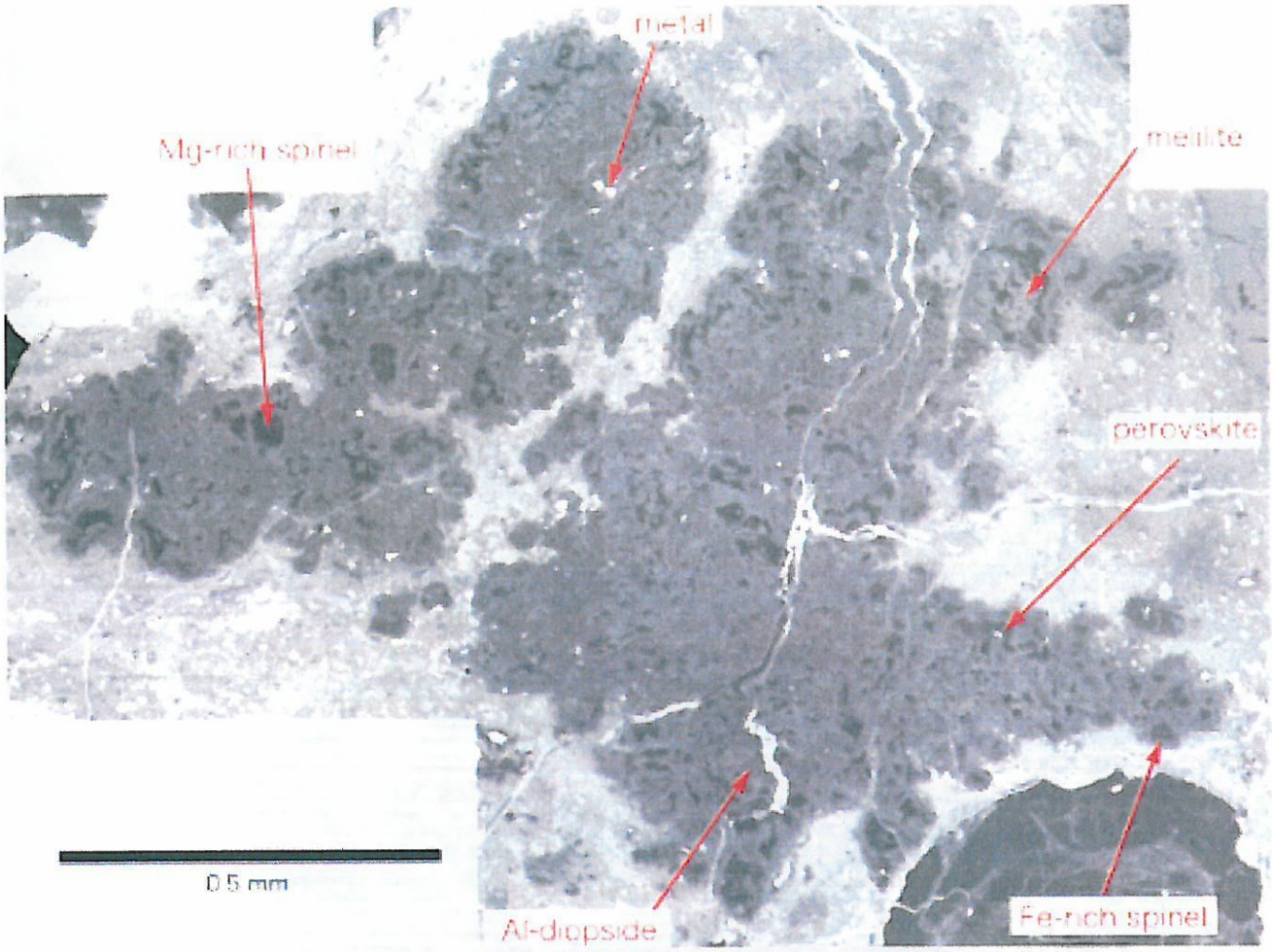

Fig. 9. Back-scattered electron mosaic of fine-grained spinel-rich CAI (FGI-12) in Efremovka.

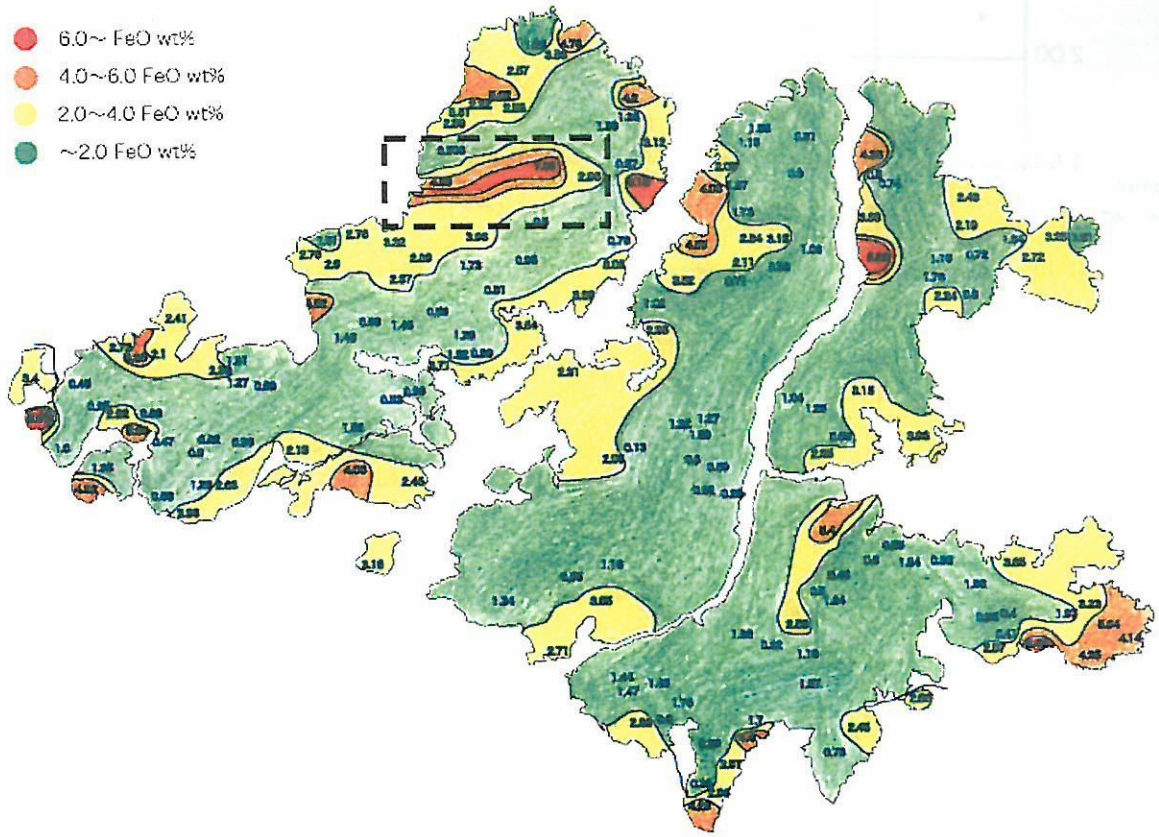

Fig. 10. Map of Fe-abundances in spinel in fine grained CAI FGI-12 from Efremovka. Numbers show concentrations of FeO in analyzed spinel grains. Most FeO-rich spinel grains are located near the CAI margin. One FeO-rich spinel occurs in the interior of the CAI (enclosed by dashed box); however, this area coincides with a wide crack in the CAI filled by matrix grains (compare with Fig. 9). Thus, even though this FeO-rich spinel occurs in the interior of the CAI, it is relatively close to matrix material.

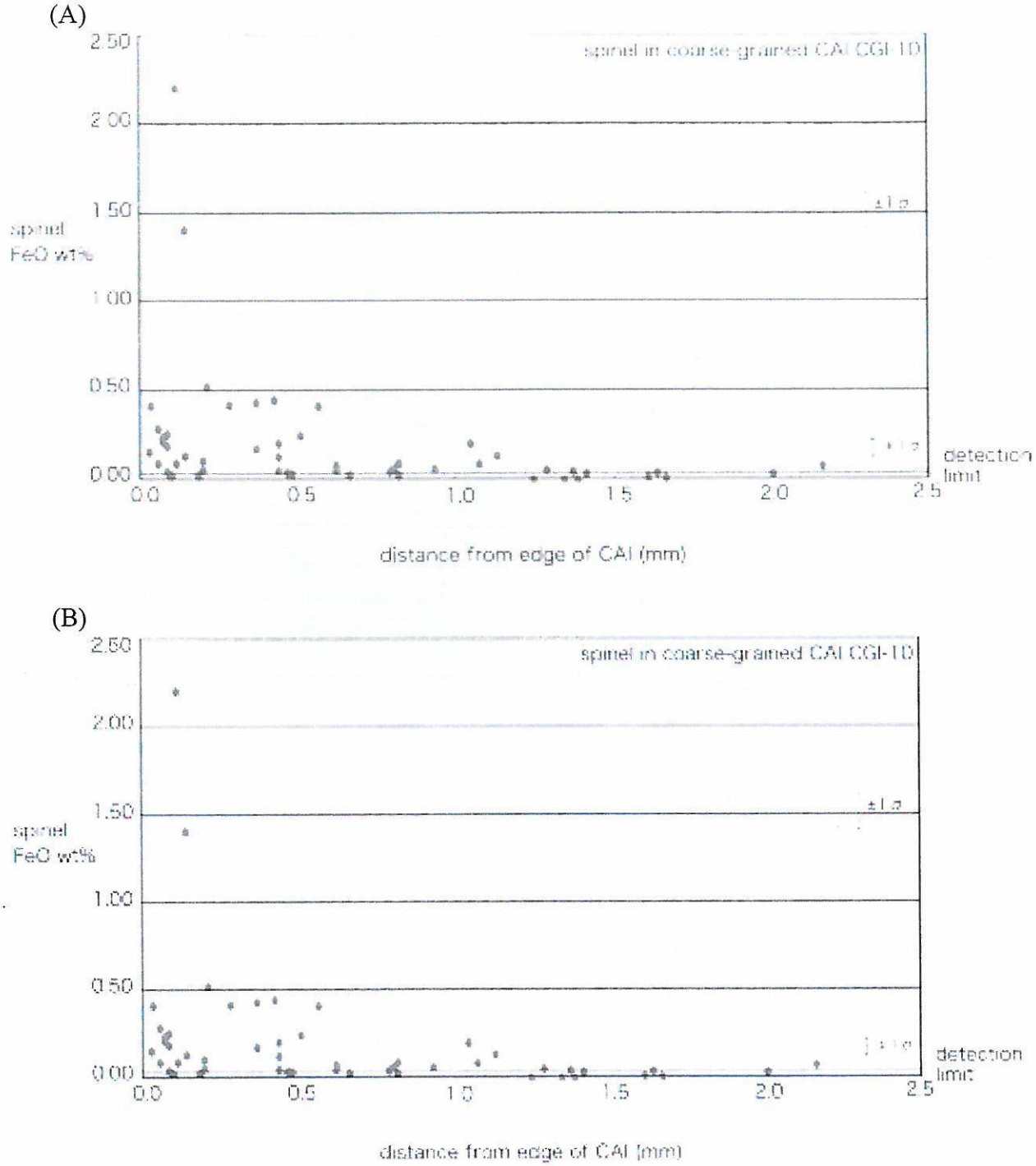

Fig. 11. Spinel FeO-content vs. distance for edge of CAI for FGI-12 (A) and coarse grained type B1 CAI CGI-10 (B), both from Efremovka (see Fig. 8)

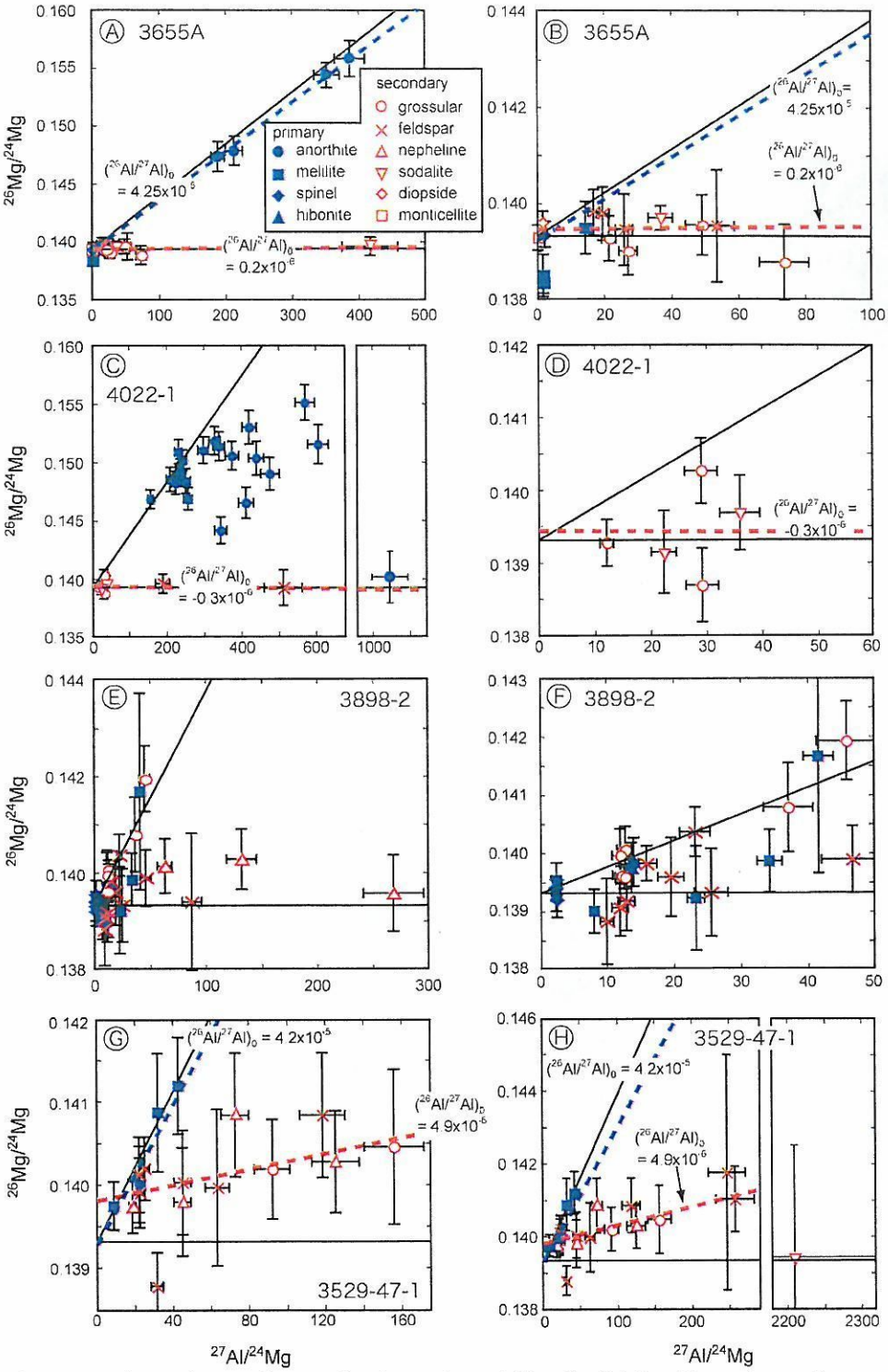

Fig. 12. Al-Mg isotopic results from four Allende CAIs. Error bars show ±2σ. Solid lines are reference lines showing initial $^{26}Al/^{27}Al = 4.5x10^{-5}$ and 0. Dashed lines are fits to data from primary (blue) and secondary (red) minerals. Points used to calculate regressions and uncertainties of the fits are discussed in the text. (a,b) Type B1 CAI 3655A. (c,d) Type B2 CAI 4022-1. (e,f) Compact Type A CAI 3898-2. (g,h) Fluffy Type A CAI 3529-47-1.

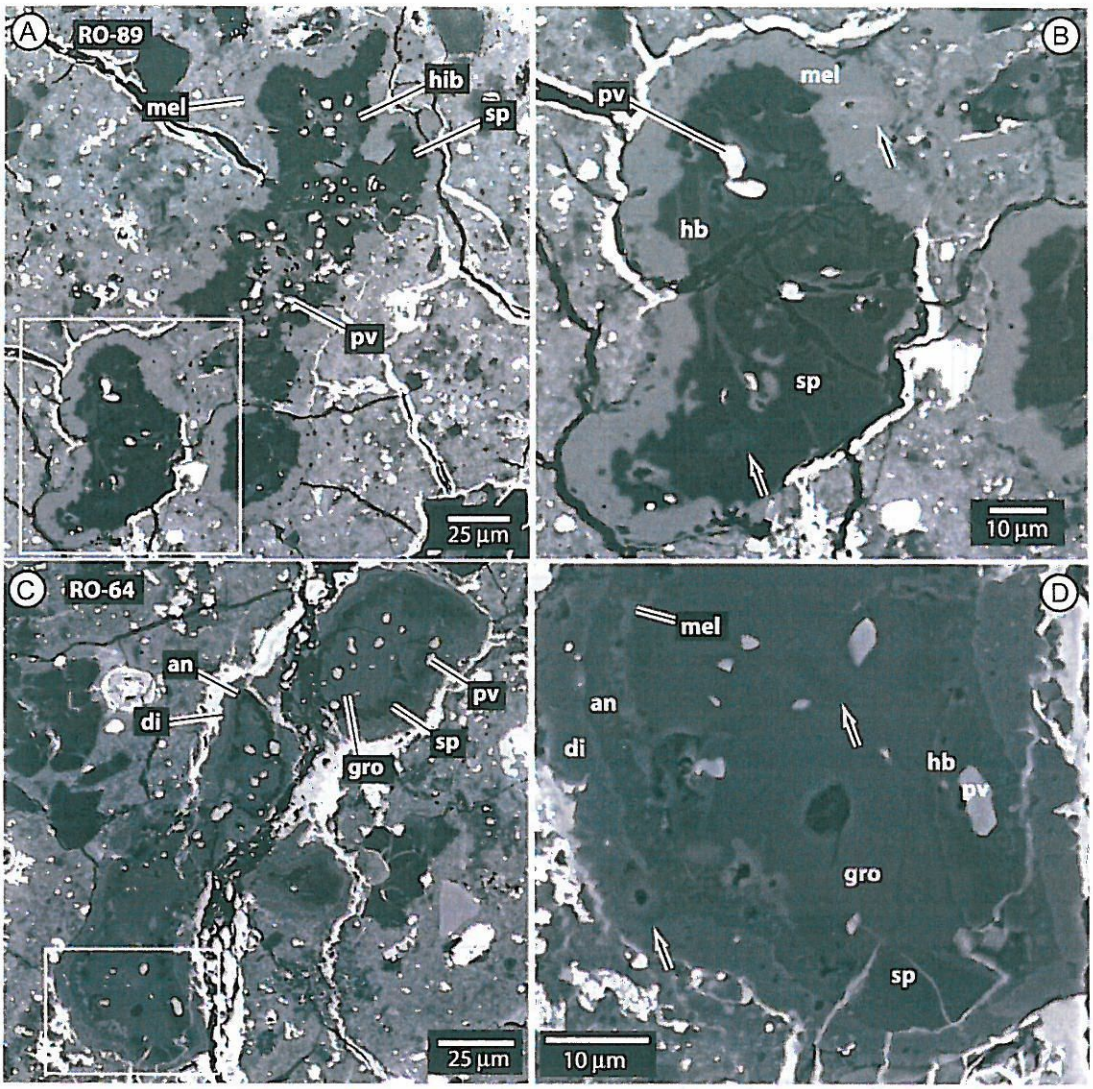

Fig. 13. Back-scattered electron (BSE) images of CAIs from Acfer 094: (A,B) refractory object 89; (C,D) refractory object 64. Areas shown in detail in (B) and (D) are highlighted by box in (A) and (C), respectively. Craters sputtered during SIMS analyses for oxygen isotopes are shown by black and white arrows. Mineral abbreviations: an = anorthite; di = diopside: gro = grossite; hb = hibonite; mel = melilite; pv = perovskite; sp = spinel.

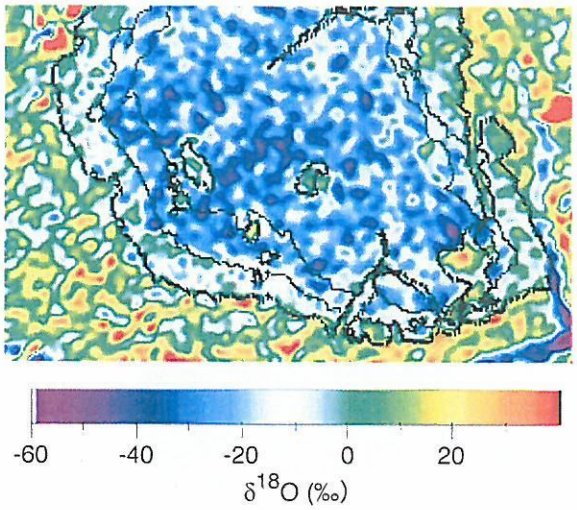

Fig. 14. Oxygen isotope map of a portion of CAI RO-64 (see Fig. 13D).

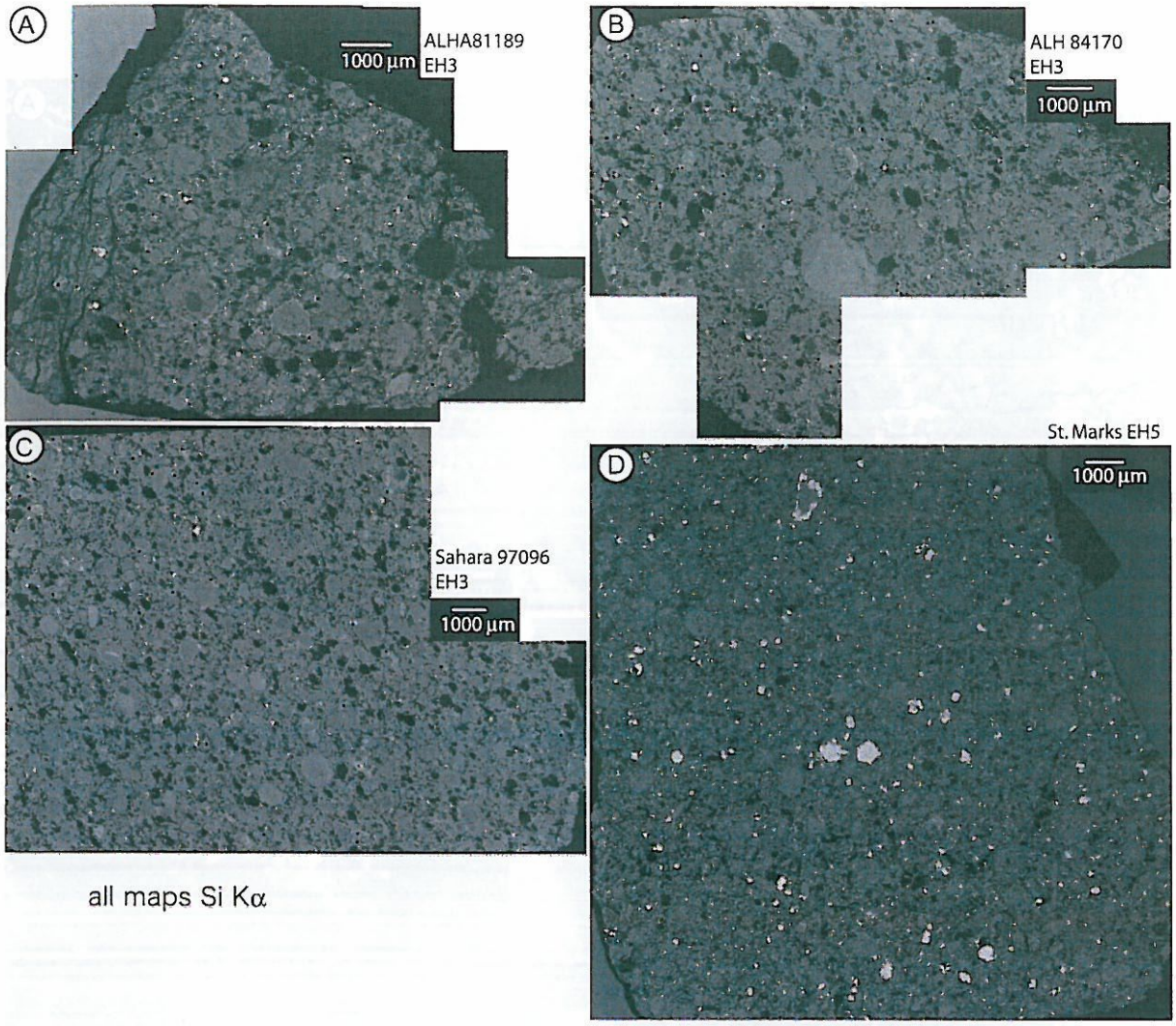

Fig. 15. Si Ka X-ray maps of EH chondrites: (A) ALHA81189, EH3; (B) ALH 84170, EH3; (C) Sahara 97096, EH3; (D) St. Marks, EH5.

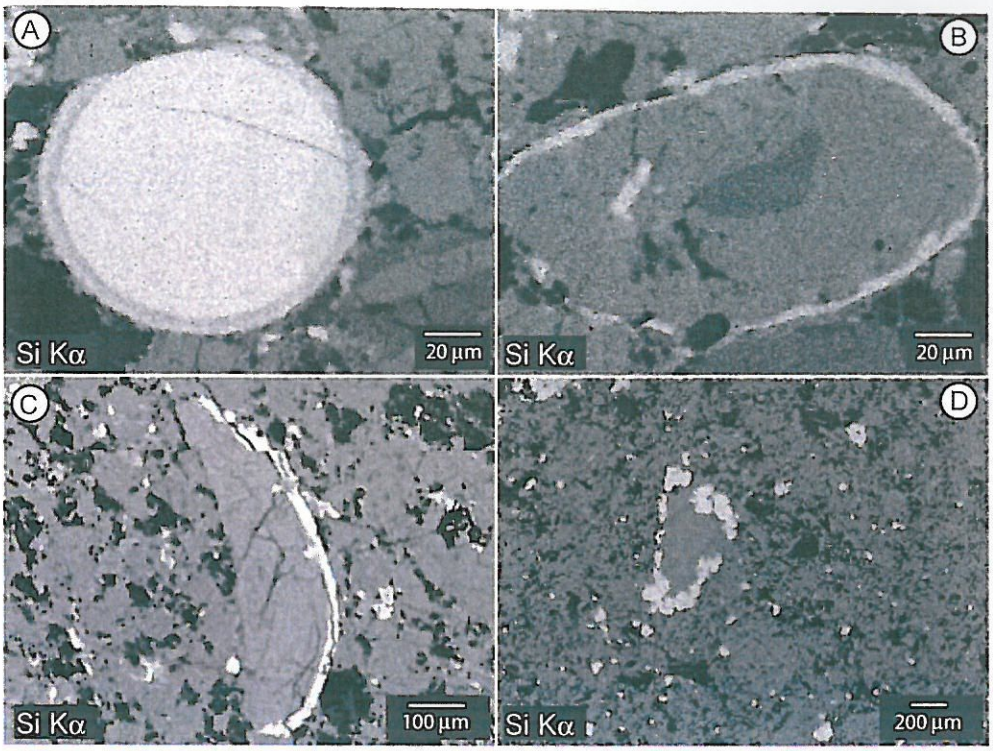

Fig. 16. Si Ka X-ray maps of characteristic objects in EH chondrites: (A) silica spherule in ALHA81189; (B) POP chondrule mantled by silica rim in ALHA81189; (C) fragmented chondrule with silica rim on original surface in ALH 84170 (D) coarse-grained quartz crystals in chondrule in St. Marks. Silica spherule shown in (A) is mantled by a silica-rich rim, but most spherules are unrimmed.

Chondrules in EH chondrites

A. Mineral textures

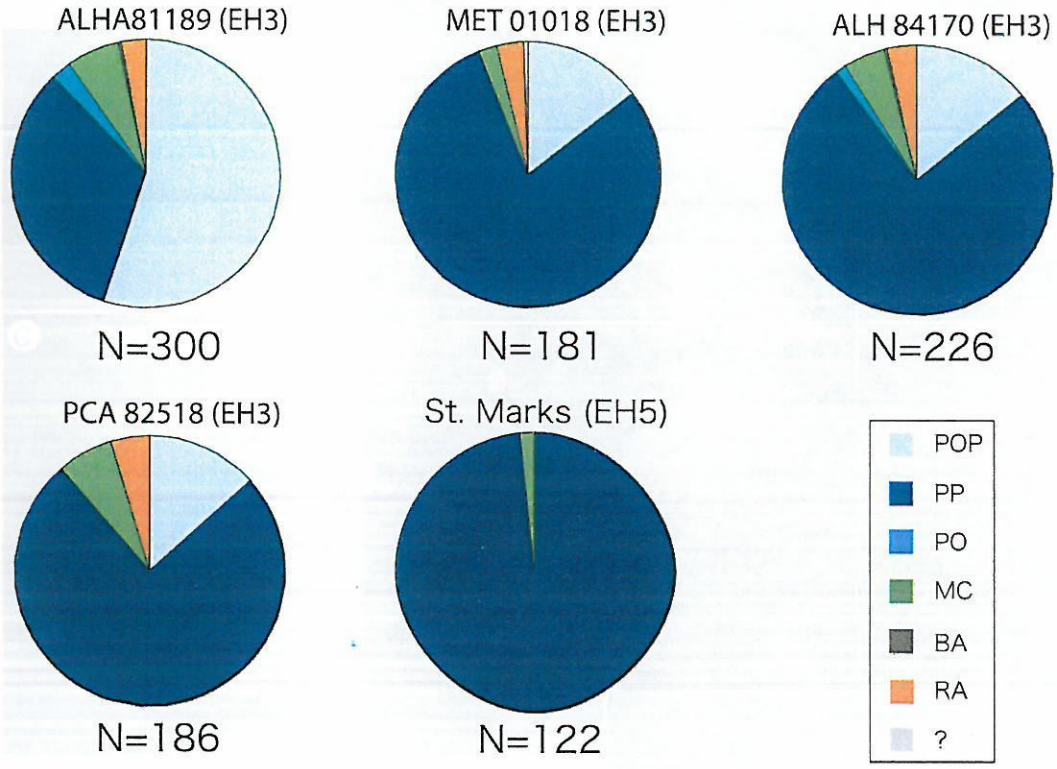

B. Whole vs. fragmented chondrules.

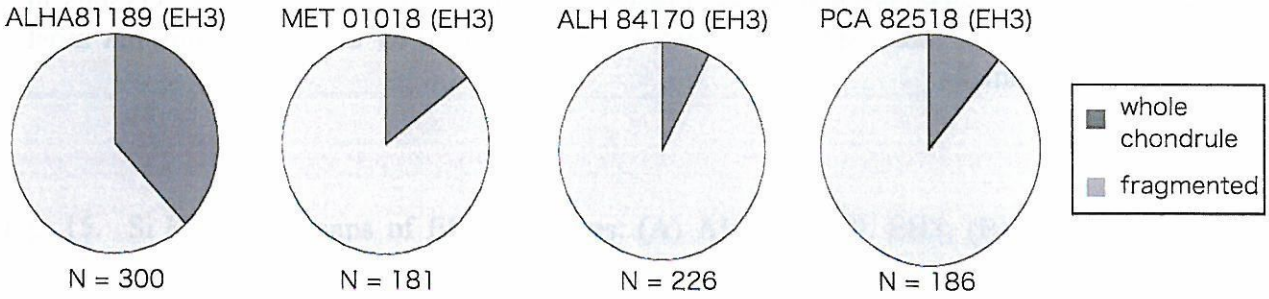

Fig. 17. Chondrule textures in EH chondrites based on thin section observations. A. Mineral texture. B. Whole vs. fragmented chondrules. Texture abbreviations: POP = porphyritic olivine and pyroxene; PP = porphyritic pyroxene; PO = porphyritic olivine; MC = microcrystalline; BA = barred; RA = radial; ? = unusual texture.

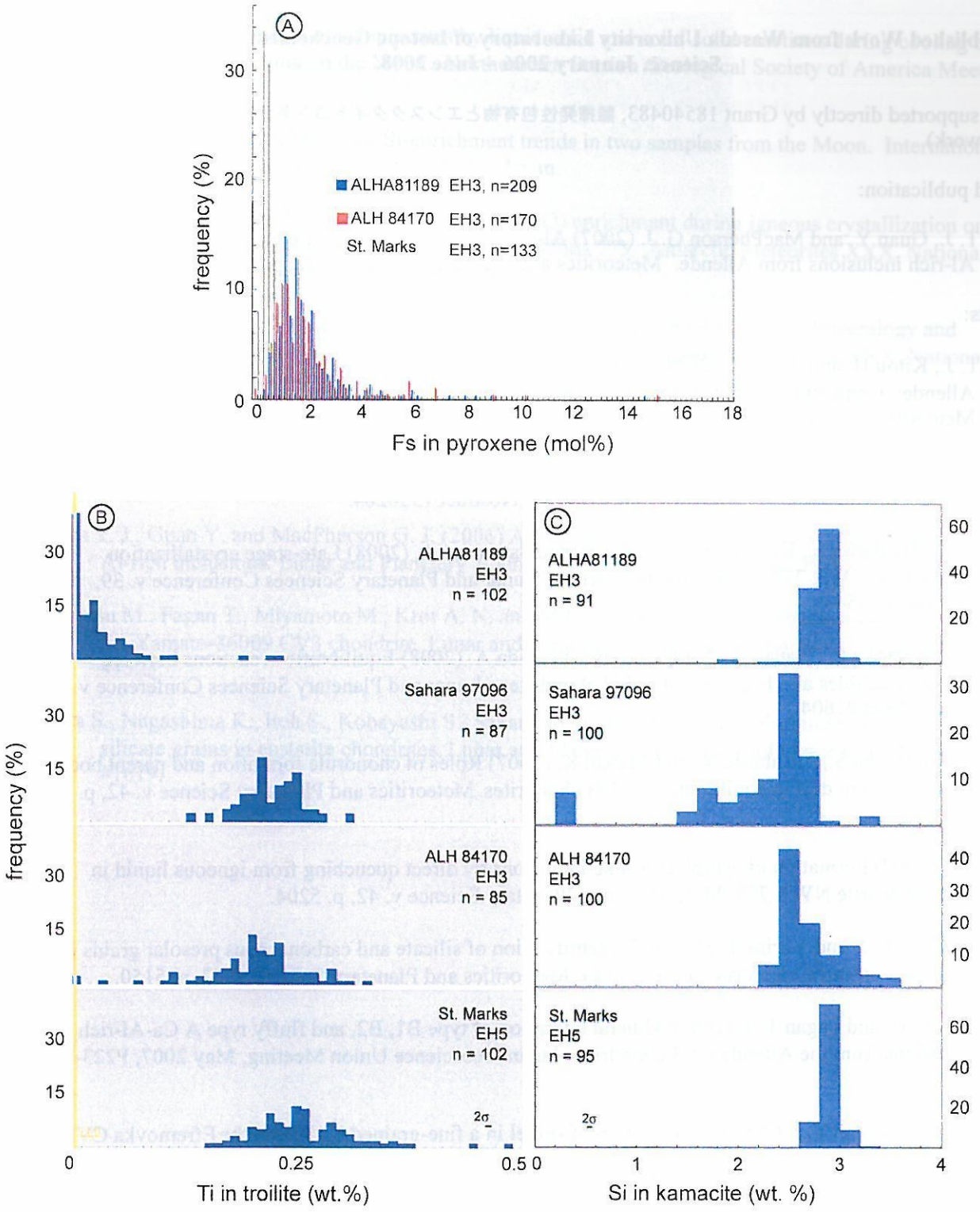

Fig. 18. Variations in mineral compositions in EH chondrites. (A) Fe/(Fe+Mg) in pyroxene; (B) Ti in troilite; (C) Si in kamacite. Analyses from ALHA81189, ALH 84170 and St. Marks are shown in (A). The same meteorites and Sahara 97096 are shown in (B) and (C).

Published Work from Waseda University Laboratory of Isotope Geochemistry and Planetary Science, January 2006 – June 2008.

([1]work supported directly by Grant 18540483, 難揮発性包有物とエンスタタイトコンドライトの変質作用; [2]other work)

refereed publication:

[1]Fagan T. J., Guan Y. and MacPherson G. J. (2007) Al-Mg isotopic evidence for episodic alteration of Ca-Al-rich inclusions from Allende. Meteoritics and Planetary Science v. 42, p. 1221-1240.

abstracts:

[1]Fagan T. J., Kitou H. and Tasai Y. (2008) Cathodoluminescence of anorthite in two type B CAIs from Allende: Contrasting alteration patterns. Meteoritics and Planetary Science (submitted for Meteoritical Society annual meeting).

[2]Fagan T. J. (2008) Products of late-stage crystallization in lunar meteorites: Do pegmatites exist on the Moon? International Geological Congress v. 33, Abstract 1338284.

[2]Fagan T. J., Hayakawa S., Kodama S., Kataoka Y. and Sasamoto A. (2008) Late-stage crystallization products in NWA 773 group lunar meteorites. Lunar and Planetary Sciences Conference v. 39, Abstract #1854.

[1]Fagan T. J., Kataoka S., Matsui K., Norose K. and Yoshida A. (2008) Equilibration reactions between silicates, sulfides and Fe,Ni-metal in EH chondrites. Lunar and Planetary Sciences Conference v. 39, Abstract #1604.

[1]Fagan T. J., Kataoka S., Takahashi Y. and Matsui K. (2007) Roles of chondrule formation and parent body metamorphism during equilibration of EH chondrites. Meteoritics and Planetary Science v. 42, p. 5205.

[2]Fagan T. J. (2007) Formation of symplectite-like inclusions by direct quenching from igneous liquid in lunar meteorite NWA 773. Meteoritics and Planetary Science v. 42, p. 5204.

[1]Ebata S., Fagan T. J. and Yurimoto H. (2007) Identification of silicate and carbonaceous presolar grains in the type 3 enstatite chondrite ALHA81189. Meteoritics and Planetary Science v. 42, p. 5150.

[1]Tasai Y., Sato H. and Fagan T. J. (2007) Mineral alteration of type B1, B2, and fluffy type A Ca-Al-rich inclusions from the Allende CV3 chondrite. Japan Geoscience Union Meeting, May 2007, P223-P005.

[1]Kashima D. and Fagan T. J. (2007) Fe-alteration of spinel in a fine-grained CAI from the Efremovka CV3 chondrite. Japan Geoscience Union Meeting, May 2007, P223-P004.

[1]Kataoka S., Takahashi Y. and Fagan T. J. (2007) Setting of equilibration process in the EH chondrites based on chondrule types and silica polymorphs. Japan Geoscience Union Meeting, May 2007, P223-P006.

[1]Fagan T. J. and Kudo M. (2007) Setting of Na-alteration in a type B2 Ca-Al-rich inclusion from the Allende CV3 chondrite. Japan Geoscience Union Meeting, May 2007, P223-013.

[1]Fagan T. J., Krot A. N., Kobayashi S. and Yurimoto H. (2007) Correlation between texture and oxygen isotopic systematics in CAIs from Acfer 094. Lunar and Planetary Sciences Conference v. 38, Abstract #1213.

[2]Fagan T. J. (2007) Formation of symplectites by liquid-solid and solid-solid reactions during cooling of an FeO-enriched magma on the Moon. Northeastern Section Geological Society of America Meeting, Paper No. 6-4.

[2]Fagan T. J. (2006) Fe-enrichment vs. Si-enrichment trends in two samples from the Moon. International Mineralogical Association Meeting, Kobe, Japan.

[2]Fagan T. J. (2006) A record of extreme FeO/(MgO+FeO) enrichment during igneous crystallization on the Moon preserved in lunar meteorite Northwest Africa 773. Antarctic Meteorites XXX, National Institute of Polar Research, Tokyo, p. 9-10.

[1]Komatsu M., Krot A. N., Fagan T., Miyamoto M., Mikouchi T. and Keil K. (2006) Mineralogy and petrography of the oxidized CV chondrite Yamato 86009. Antarctic Meteorites XXX, National Institute of Polar Research, Tokyo, p. 42-43.

[1]Komatsu M., Fagan T., Miyamoto M., Krot A. N. and Mikouchi T. (2006) Mineralogical studies of amoeboid olivine aggregates in the oxidized CV chondrite Y-86009. Japan Geoscience Union Meeting. Abstract P155-017_e.

[1]Fagan T. J., Guan Y. and MacPherson G. J. (2006) Al-Mg isotopic constraints on alteration of Allende Ca-Al-rich inclusions. Lunar and Planetary Sciences Conference v. 37, (CD-ROM) #1213.

[1]Komatsu M., Fagan T., Miyamoto M., Krot A. N. and Mikouchi T. (2006) Amoeboid olivine aggregates in the Yamato-86009 CV3 chondrite. Lunar and Planetary Sciences Conference v. 37, (CD-ROM) #1523.

[1]Ebata S., Nagashima K., Itoh S., Kobayashi S., Sakamoto N., Fagan T. J. and Yurimoto H. (2006) Presolar silicate grains in enstatite chondrites. Lunar and Planetary Sciences Conference v. 37, (CD-ROM) #1619.

CATHODOLUMINESCENCE OF ANORTHITE IN TWO TYPE B CAIS FROM ALLENDE: CONTRASTING ALTERATION PATTERNS

T. J. Fagan[1], H. Kitou[1], Y. Tasai[1]. [1]Department of Earth Sciences, Waseda University, Tokyo, Japan. (fagan@waseda.jp).

Introduction: Refractory Ca-Al-rich inclusions (CAIs) preserve a record of early, "primary" crystallization over a limited range of high temperatures in the solar nebula followed by poorly constrained "secondary" recrystallization/ alteration events [1]. Type B CAIs from the CV3 Allende are noteworthy in this respect because they exhibit texturally distinct secondary minerals, indicating that significant thermal events post-dated primary crystallization [e.g., 2,3]. More subtle effects of secondary processes are manifested by variable cathodoluminescence patterns of primary anorthite. In general, variable cathodoluminescence (CL) in minerals has been attributed to variations in defect structure and minor element zoning that are often difficult to detect by other means. In this study, we use CL of anorthite to identify different patterns of alteration in two CAIs—one Type B1 and one B2—from Allende.

Analytical Methods: Mineral assemblages and textures in polished thin sections of CAIs 3655A (Type B1) and 4022-1 (B2) were characterized using petrographic microscopes and a JEOL JXA-8900 electron microprobe at Waseda University. Cathodoluminescence (CL) of primary anorthite was studied using a Premier American Technologies Corporation ELM-3 Luminoscope. Covariations between CL brightness and minor element compositions of anorthite were investigated by elemental mapping and quantitative electron probe microanalysis (EPMA). Prior to EPMA, back-scattered electron (BSE) images were overlain on CL images and image transparencies were adjusted using imaging software. This procedure was used to ascertain the locations of EPMA points with respect to CL-bright and CL-dark domains in anorthite. Relatively high current (50 nA) and spot size (8x9 μm) were used at 15 kV for quantitative analyses in order to detect minor concentrations of Na and Mg in anorthite. Lower limits of detection under these analytical conditions are: Na_2O, 0.011 wt%; MgO, 0.012 wt%.

Results and Discussion: Primary anorthite in both CAIs exhibits blue CL with variable brightness. In CAI 3655A, CL-bright and CL-dark domains tend to have sharp, angular boundaries with simple geometries. The CL-dark domains are enriched in MgO (0.19 vs. 0.11 wt%) and Na_2O (0.12 vs. 0.08 wt%) compared to CL-bright domains. Primary anorthite in CAI 4022-1 exhibits patchy, irregular CL-bright and CL-dark domains with diffuse boundaries. Quantitative EPMA results do not show a simple distinction that correlates with CL in 4022-1, but elemental mapping suggests that the CL-dark domains are relatively enriched in Na_2O and MgO. The sharp boundaries, simple shapes and well-defined elemental variations of CL patterns in 3655A anorthite suggest that this CAI experienced a simpler, less extensive alteration history than 4022-1. This is consistent with Al-Mg results and subtle contrasts in textures of secondary minerals [2]. The CL-imaging combined with other data may reflect general differences in alteration histories of Type B1 and B2 CAIs.

References: [1] MacPherson G.J.. in Davis A.M. (ed.) *Treatise on Geochemistry* 1:201-246. [2] Fagan T.J. et al. 2007 *MaPS* 42:1221-1240. [3] Ushikubo T. et al. 2007 *MaPS* 42:1267-1279.

T.J. Fagan, submitted for 33rd International Geological Congress, session on origin of the Moon.

Products of late-stage igneous crystallization in lunar meteorites: Do pegmatites exist on the Moon?

Many of the clasts in the mafic lunar breccia Northwest Africa 773 (NWA 773) and paired meteorites originate from a common igneous system. A low-Fe# [Fe# = Fe/(Fe+Mg)] olivine micro-gabbro represents an early stage of crystallization. Pyroxene-bearing clasts with progressively increasing Fe# and Ti# [Ti# = Ti/(Ti+Cr)] formed at progressively later stages of igneous fractionation. These samples offer insight into igneous differentiation of mafic liquid on the Moon.

This project focuses on late-stage crystallization products including: (1) intercumulus alkali-rich domains in the olivine cumulate; (2) aphyric, silica-rich (SiO_2 as high as 90 wt.%) quenched melt inclusions in olivine; (3) high-Fe# (>0.9) symplectite and symplectite-like clasts; (4) high-Fe#, alkalic clasts without symplectic textures. The intercumulus domains clearly attained their enrichments in incompatible elements by isolation from the main mass of liquid and fractional crystallization of cumulate minerals. Fractional crystallization was also involved in petrogenesis of the other late-stage lithologies, but silicate liquid immiscibility (SLI) also may have played a role. The aphyric melt inclusions are depleted in FeO and MgO, enriched in SiO_2, and have high Fe#, as would be expected for late-stage residues of fractionation; however, they are depleted in P_2O_5 compared to earlier-stage melt inclusions. This requires a process such as SLI or fractionation of a very late-stage P-bearing mineral. The symplectites are composed mostly of fayalite, hedenbergitic pyroxene and silica. These rocks have high Fe#, as would be expected from crystal fractionation, but they are FeO-rich and alkali-poor, in contrast to crystal fractionation trends. The high-Fe# alkalic clasts have both high Fe# and high incompatible element concentrations, distinct from the symplectites.

This variety of late-stage igneous rocks highlights the contrast between water-bearing igneous systems on Earth and water-absent igneous rocks of the Moon. In many terrestrial igneous systems, H_2O is concentrated in late-stage liquids, and de-polymerizes those liquids. This H_2O-enrichment affects the miscibility, limits the viscosity, and enhances the diffusion rates of elements in late-stage liquids. These processes are important in the origin of terrestrial coarse-grained pegmatites. Pegmatites might have no real equivalent on the Moon. Relatively fine-grained clasts with K,Ba-feldspar, Ca-phosphates, and high Fe# olivine and/or pyroxene may be the closest lunar counterparts to terrestrial pegmatites.

LATE-STAGE CRYSTALLIZATION PRODUCTS IN NWA 773 GROUP LUNAR METEORITES. T. J. Fagan[1]*, S. Hayakawa[1], S. Kodama[1], Y. Kataoka[1] and A. Sasamoto[1], [1]Department of Earth Sciences, Waseda University, Tokyo, Japan 169-8050. *(fagan@waseda.jp)

Introduction: Many clasts in lunar meteorite Northwest Africa 773 and related meteorites can be linked together to illustrate stages of igneous evolution of a mafic magmatic system on the Moon [1-4]. Among the most distinctive rock-types in this set are olivine cumulate gabbros (OC) and fayalite-hedenbergite-silica symplectites [1-3]. These rocks originate from early and late stages, respectively, of magmatic evolution. However, in addition to the symplectites, a variety of domains with high Fe/(Fe+Mg) or enrichments in incompatible elements suggesting late-stage crystallization are present. In this study, we document several types of late-stage lithologies in NWA 773 group lunar meteorites and speculate on late-stages of magmatic evolution.

Methods: Late-stage crystallizing domains were identified in one polished thin section (PTS) of NWA 773 (on loan from M. Killgore of University of Arizona) and one PTS of NWA 2727 (Waseda University sample). The samples were studied using standard petrography, back-scattered electron (BSE) images and X-ray elemental maps. The elemental maps were critical for identifying high SiO_2, K_2O and/or Fe/(Fe+Mg) signatures of late-crystallizing assemblages. BSE images, X-ray maps and quantitative elemental analyses of minerals and glass were collected using a JEOL JXA-8900 electron microprobe at Waseda University. Quantitative analyses were collected by wavelength dispersive spectroscopy using well-characterized oxide and silicate standards at 15 kV and 20 nA. Incident beam spot sizes were one or two μm for most analyses of minerals and for glasses in fine inclusions. Larger spot sizes (7x5 μm) were used for some analyses of glass ± fine minerals in melt inclusions.

Late-stage rocks: *Symplectites.* The symplectites consist mostly of fine-grained (generally ≤4 μm across) intricately interwoven blebs of fayalitic olivine (Fa_{95}), hedenbergitic pyroxene ($Wo_{38}Fs_{53}$) and silica (Fig. 1). Detailed modes based on BSE images show that typical symplectites are similar to or somewhat pyroxene-rich compared to the idealized modes that would result from pyroxferroite breakdown. Some symplectite-like lithologies consist of multiple pyroxene-hosted inclusions of silica+olivine. Coarse-grained fayalitic olivine or hedenbergitic pyroxene may occur adjacent to symplectite domains; both sharp and gradational boundaries (with pyroxene riddled with curved inclusions of silica+olivine) occur. Coarse-grained feldspar ($An_{75}Or_4$) and Ca-phosphates are present in some symplectites. Most of the symplectites probably formed by breakdown of pyroxferroite in pyroxene-rich domains, leading to the variable excesses in mode of pyroxene.

Symplectites with glass inclusions. Some symplectites show variations in texture from the typical 3-phase symplectite to pyroxene-poor, olivine-rich domains. This olivine hosts multiple amoeboid inclusions of feldspathic glass ± fine elongate silica. The occurrence of feldspathic glass in these domains implies formation by direct quenching of silicate liquid without intervening pyroxferroite.

K,Ba-feldspar-bearing rocks. Coarse-grained (non-symplectic) Fe-rich olivine ± pyroxene occur with K,Ba-feldspar, feldspathic glass and silica in these clasts (Fig. 2). BaO-content in feldspar ranges up to 8.5 wt%. Ca-phosphates, ilmenite, troilite, ±baddeleyite also may be present.

K,Ba-feldspar also occurs in intercumulus domains of the olivine cumulate gabbro (Fig. 3). These domains are bordered by olivine and pyroxenes with compositions typical of the gabbro. Ca-phosphates, troilite and ilmenite coexist with the alkali feldspar (1 to 4 wt% BaO) in these domains.

Aphyric melt inclusions. Two types of melt inclusions occur in olivine. One type is characterized by dendritic pyroxene and appears to be primary. The other type is typically aphyric (though minor crystals may be present), and SiO_2-rich (as high as 90 wt% SiO_2). The pyroxene-phyric inclusions have been identified only in OC olivine, whereas aphyric inclusions occur in OC olivine, where they appear to be secondary, and fayalitic olivine, where they may be primary.

Late-stage crystallization: Fractional crystallization of olivine and pyroxene led to enrichments in incompatible K and Ba, among other elements, in intercumulate domains of the OC. This enrichment occurred without significant fractionation of Fe/(Fe+Mg). The residual intercumulus pockets were isolated from the main body of liquid, which subsequently fractionated to form liquid high in K_2O, BaO and Fe/(Fe+Mg). Crystallization of this liquid formed the K,Ba-feldspar-bearing clasts.

The evolution and timing of symplectite-bearing clasts and aphyric melt inclusions are uncertain. Most of these rocks are not K,Ba-rich. They might have formed after fractionation of K and Ba by crystallization of feldspar. Alternatively, silicate liquid immiscibility may have played a role in evolution of these late-stage lithologies.

References: [1] Fagan T.J. et al. (2003) *MaPS 38,* 529-554. [2] Jolliff B.L. et al. (2003) *GCA 67, 4857-4879.* [3] Zeigler R.A. et al. (2007) *LPS XXXVIII,* #2109. [4] Jolliff B.L. et al. (2007) *LPS XXXVIII,* #1489.

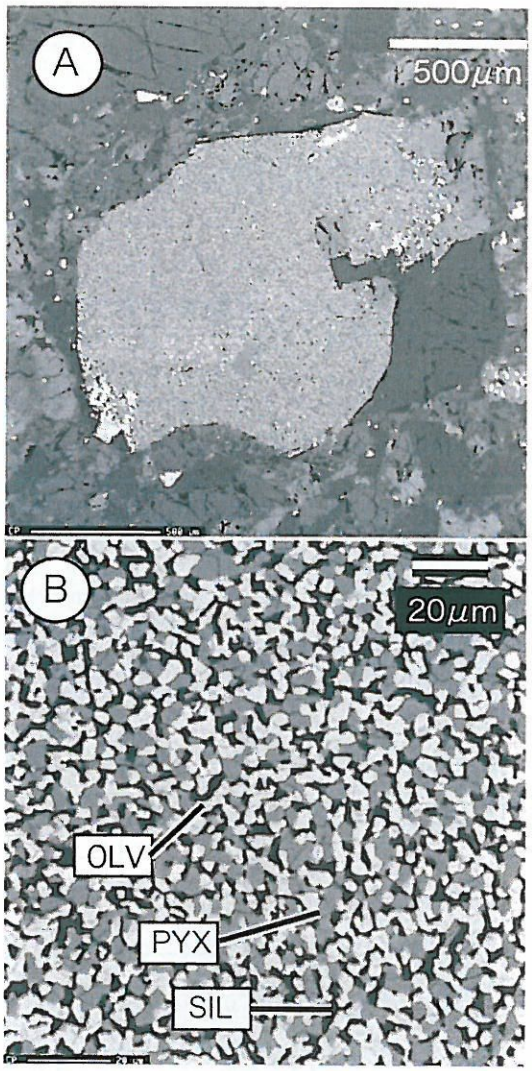

Fig. 1. BSE images of symplectite clast (A) and detail of symplectite texture (B). Abbreviations for this and other figures: OLV = olivine; PYX = pyroxene; SIL = silica; CAP = Ca-phosphate; CPX = high-Ca pyroxene; FGL = feldspathic glass; ILM = ilmenite; KBF = K,Ba-feldspar; MPX = low-Ca pyroxene; PLG = plagioclase feldspar; TRO = troilite.

Fig. 3.→ BSE image (A) and X-ray elemental map (B) of intercumulus domain in olivine cumulate. Red = K, Green = Ca and B = Al Kα X-rays.

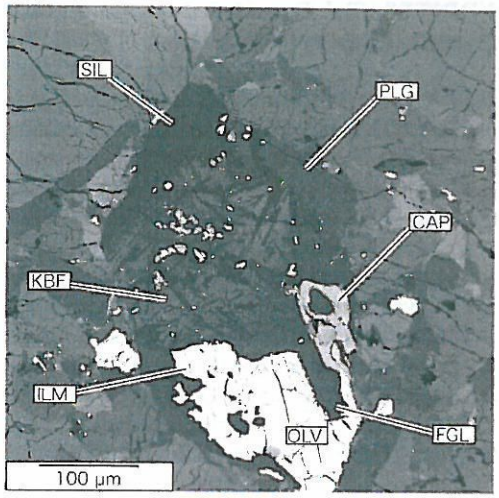

Fig. 2. BSE image of K,Ba-feldspar-bearing clast.

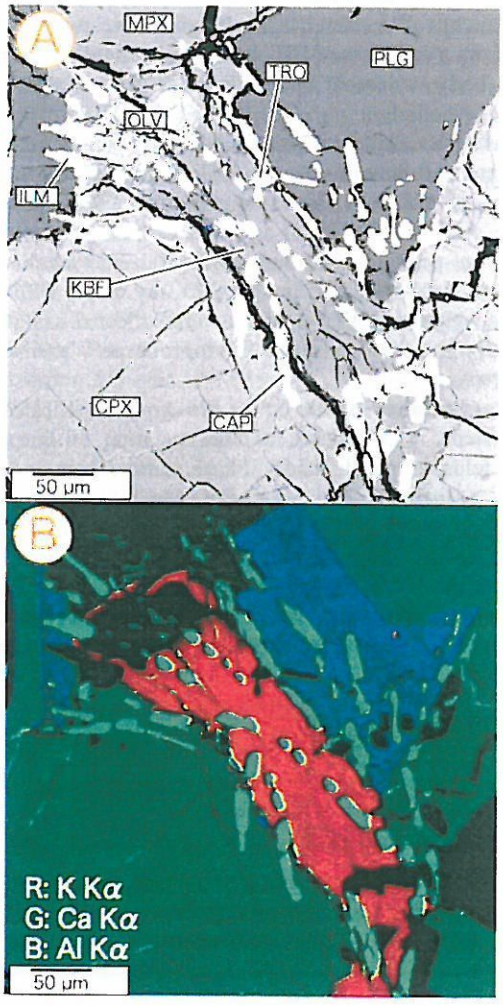

EQUILIBRATION REACTIONS BETWEEN SILICATES, SULFIDES AND Fe,Ni-METAL IN EH CHONDRITES. T. J. Fagan[1]*, S. Kataoka[1], K. Matsui[1], K. Norose[1] and A. Yoshida[1], [1]Department of Earth Sciences, Waseda University, Tokyo, Japan 169-8050. *(fagan@waseda.jp)

Introduction: An understanding of metamorphic reactions is useful because it offers insight into parent body processes and a means of identifying the most primitive chondrites. Recent work has identified some of the reactions that occur during incipient metamorphism in ordinary and carbonaceous chondrites [1]. Extrapolition of this progress to enstatite chondrites is plausible [2], yet different reactions may be significant in light of the distinct mineralogy (and hence formation conditions) of enstatite chondrites.

This project addresses metamorphism of enstatite chondrites by developing a mass-balance model of the main transfers of mass between silicates, sulfides and metallic minerals. We use an algebraic approach ("reaction space", developed originally for terrestrial metamorphism [3,4]) to limit the number of reactions that need to be considered to model changes in mineral abundances. We combine this model with observations from a small set of EH chondrites to identify pre-parent body vs. parent body effects as well as metamorphic reactions.

Methods: Algebraic manipulation of phases and components follow references [3-6]. Petrologic observations of polished thin sections of ALHA81189 (EH3), ALH 84170 (EH3) and St. Marks (EH5) are based on petrography, and elemental and back-scattered electron (BSE) imaging. X-ray maps, BSE images and quantitative analyses were collected using a JEOL JXA-8900 electron microprobe at Waseda University.

Mass balance model: In the EH chondrite silicate sub-system, main phases include enstatite, olivine, silica, feldspar and diopside. Phase endmembers and solid solutions in Na_2O-CaO-MgO-Al_2O_3-SiO_2 (NCMAS) are shown in Table 1. Fe and K, among other elements, may also occur in the natural minerals, but these can be described in terms of simple exchange components $FeMg_{-1}$ and NaK_{-1}; the phase endmembers as written in NCMAS are sufficient to denote mineral abundances [3,4].

Table 1. EH silicates in NCMAS oxide components.

	Na_2O	CaO	MgO	Al_2O_3	SiO_2
$NaAlSi_3O_8$	0.5	0	0	0.5	3
$CaMgSi_2O_6$	0	1	1	0	2
$MgSiO_3$	0	0	1	0	1
$AlAlMg_{-1}Si_{-1}$	0	0	-1	1	-1
SiO_2	0	0	0	0	1
$CaAlNa_{-1}Si_{-1}$	-0.5	1	0	0.5	-1
Mg_2SiO_4	0	0	2	0	1

The use of oxide components in Table 1 is a choice, however, and the phase compositions can be rewritten in terms of a new set of components (Table 2) as long as the new components span the same composition space [3-6].

Table 2. EH silicates in NCMAS new components.

	ab	di	en	*tk*	qz
$NaAlSi_3O_8$	1	0	0	0	0
$CaMgSi_2O_6$	0	1	0	0	0
$MgSiO_3$	0	0	1	0	0
$AlAlMg_{-1}Si_{-1}$	0	0	0	1	0
SiO_2	0	0	0	0	1
$CaAlNa_{-1}Si_{-1}$	-1	1	0	1	1
Mg_2SiO_4	0	0	2	0	-1

Each row in Table 2 is a mass balance. With the new set of components, the bottom two rows can be viewed as reactions:

$$ab = di + tk + qz - CaAlNa_{-1}Si_{-1} \quad (1a)$$

equivalently, ab = jadeite + quartz (1b)

and $fo + qz = 2\ en$ (2)

In EH chondrites, reaction (1) appears to be minor, but (2) is a significant monitor of equilibration [7].

Table 3*. Main EH phases in NCMAS+O,S,Fe.

	Na	Ca	Mg	Al	Si	O_2	S_2	Fe
ab	1	0	0	1	3	4	0	0
di	0	1	1	0	2	3	0	0
en	0	0	1	0	1	1.5	0	0
tk	0	0	-1	2	-1	0	0	0
qz	0	0	0	0	1	1	0	0
O_2	0	0	0	0	0	1	0	0
S_2	0	0	0	0	0	0	1	0
tl	0	0	0	0	0	0	0.5	1
fm	0	0	-1	0	0	0	0	1
ka	0	0	0	0	0	0	0	1
pl	-1	1	0	1	-1	0	0	0
fo	0	0	2	0	1	2	0	0

*ab, di, en, *tk*, qz as in Table 2; tl = FeS troilite; *fm* = $FeMg_{-1}$ exchange; ka = Fe,Ni-metal kamacite; *pl* = $CaAlNa_{-1}Si_{-1}$ plagioclase exchange; fo = Mg_2SiO_4 forsterite.

Reduction of a more complete matrix of the EH reacting system (Table 3) shows reactions (1), (2) and:

$$en + fm + 0.5\ S_2 = tl + qz + 0.5\ O_2 \quad (3)$$

and $$en + fm = ka + qz + 0.5\ O_2 \quad (4)$$

reflecting sulfidation (3) and reduction (4) of silicates.

Application to EH chondrites: The EH3 ALHA81189 has abundant POP chondrules with fine-

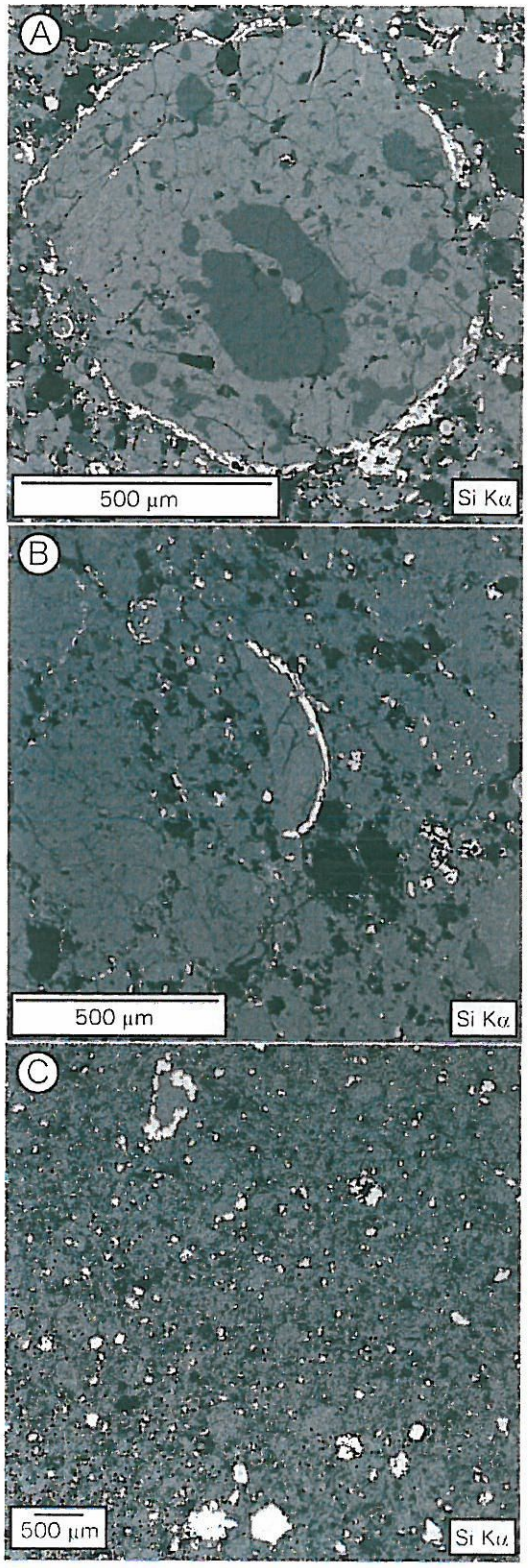

← Fig. 1. Si Ka X-ray maps of chondrules and silica textures in (A) ALHA81189, (B) ALH 84170 and (C) St. Marks. In general, gray = enstatite, dark gray = olivine, white = silica.

grained SiO_2-rich rims; in EH3 ALH 84170, silica rims are present, but olivine is less abundant; in St. Marks, olivine is not present and silica occurs as coarse crystals (Fig. 1). This sequence reflects varying progress along reaction (2) toward equilibration in EH silicates.

Chondrules are clearly defined in both ALHA81189 and ALH 84170, yet tend to be whole in the former and fragmented in the latter (Fig. 1A,B). This indicates that ALHA81189 is not equivalent to a metamorphic protolith of ALH 84170. Thus, we infer that the variable progress on reaction (2) relating these two meteorites is due to a pre-parent body process, such as chondrule formation.

Pyroxenes in ALHA81189 and ALH 84170 share similar distributions of Fe-abundance, which contrast with the narrower range and lower Fe-abundance of St. Marks pyroxene (Fig. 2). The pyroxene compositions indicate similar, limited progress on reactions (3) and (4) in the EH3 meteorites. St. Marks experienced greater sulfidation and/or reduction, and equilibration during parent body metamorphism. ALHA81189 is a primitive EH3 chondrite due to limited processing during chondrule formation as well as minor extent of metamorphism.

References: [1] Grossman J.N. and Brearley A.J. (2005) *MaPS, 40,* 87–122. [2] Bendersky C. et al. (2007) *LPS XXXVIII,* #2077. [3] Thompson J.B. et al. (1982) *J. Petrol., 23,* 1-27. [4] Thompson J.B. (1991) *Canadian Mineral., 29,* 615-632. [5] Greenwood H.J. (1975) *Amer. Mineral., 60,* 1-8. [6] Fagan T.J. and Day H.W. (1997) *Geology, 25,* 395-398. [7] Hicks T.L. et al. (2000) *LPS XXXI,* #1491.

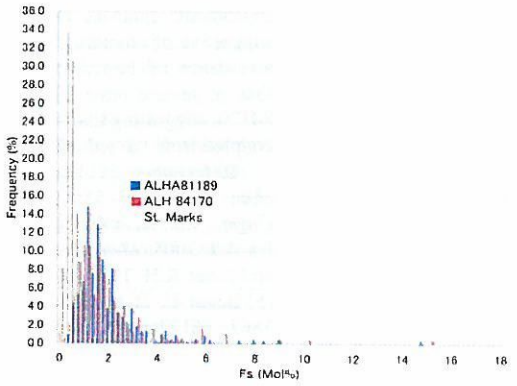

Fig. 2. Histograms of Fs content in pyroxenes from ALHA81189 (n = 209), ALH 84170 (n = 170) and St. Marks (n = 133).

ROLES OF CHONDRULE FORMATION AND PARENT BODY METAMORPHISM DURING EQUILIBRATION OF EH CHONDRITES.

T. J. Fagan[1], S. Kataoka[1], Y. Takahashi[1], and K. Matsui[2]. [1]Department of Earth Sciences, Waseda University, Tokyo, Japan 169-8050. (fagan@waseda.jp)

Introduction: Mild variations in extent of equilibration—generally considered metamorphic grade—have been identified in ordinary [1-3] and carbonaceous chondrites [4,5]. In contrast, subtle variations in equilibration of enstatite chondrites have been difficult to characterize [6-8]. In this study, we combine chondrule type with abundance of SiO_2-rich rims, Fe/(Mg+Fe) of mafic silicates, and speciation of silica to characterize equilibration in EH chondrites. Some of our observations are best explained by variations during chondrule formation—not parent body metamorphism.

Analytical Methods: Chondrule types were identified in polished thin sections of four EH3 chondrites (ALHA81189; MET 01018; ALH 84170; PCA 82518) and one EH5 chondrite (St. Marks). Elemental maps collected by electron microprobe (JEOL JXA-8900 at Waseda University) were combined with petrographic microscope observations to identify classical chondrule type (PP, POP, RP,...), presence or absence of a SiO_2-rich rim, and fragmented vs. whole chondrules. Silica polymorphs were identified (same samples except for MET 01018) by Raman spectroscopy (Jobin Yvon LabRam300 Raman microspectrometer). EPMA was used to determine Fe/(Mg+Fe) of pyroxene on a grid pattern in ALHA81189, ALH 84170 and St. Marks.

Results and Discussion: St. Marks is distinguished from the EH3s by its: (1) hazy, indistinct chondrule outlines; (2) absence of olivine; (3) low Fe/(Fe+Mg) pyroxene. The only SiO_2 polymorph identified is quartz (also see [7]), consistent with slow cooling rates of parent body metamorphism.

ALHA81189 is distinguished from the other EH3s by its abundance of: (1) POP chondrules; (2) SiO_2-rich rims; (3) whole chondrules. Cristobalite is abundant, but quartz has not been identified. Furthermore, ALHA81189 is characterized by low progress on the olivine + silica = pyroxene reaction [9]. Lack of equilibration on this reaction combined with the distinct set of chondrules suggests that the unequilibrated condition of this meteorite is due in part to incomplete reaction of olivine and SiO_2 (or $SiO_{(g)}$) during chondrule formation. The predominance of cristobalite indicates rapid cooling from high temperatures—suggestive of chondrule formation and minimal re-heating. The abundance of Fe-rich pyroxene in ALHA81189, while higher than in several other EH3s [10], is comparable to that in ALH 84170, suggesting that the reaction of olivine + Si-phase was decoupled from the reduction of Fe in pyroxene.

References: [1] Huss G.R. et al. 1981. *Geochim. Cosmochim. Acta* 45:33–51. [2] Sears D.W.G. et al. 1982. *Geochim. Cosmochim. Acta* 46:2471–2481. [3] Grossman J.N. and Brearley A.J. 2005. *Meteorit. Planet. Sci.* 40:87-122. [4] Scott E.R.D. and Jones R.H. 1990. *Geochim. Cosmochim. Acta* 54:2485–2502. [5] Bonal L. et al. 2006. *Geochim. Cosmochim. Acta* 70:1849-1863. [6] Zhang Y. et al. 1996. *J. Geophys. Research* 100:9417-9438. [7] Kimura M. et al. 2005. *Meteorit. Planet. Sci.* 40:855-868. [8] Weisberg M.K. et al. 2005. Abstract #1420. 36th Lunar Planet. Sci. Conf. [9] Hicks T.L. et al. 2000. Abstract #1491. 31st Lunar Planet. Sci. Conf. [10] Lusby D. et al. 1987. *Proc. 17th LPSC (J. Geophys. Research* 92):E679-E695.

FORMATION OF SYMPLECTITE-LIKE INCLUSIONS BY DIRECT QUENCHING FROM IGNEOUS LIQUID IN LUNAR METEORITE NWA 773.

T. J. Fagan, Department of Earth Sciences, Waseda University, Tokyo, Japan 169-8050. (fagan@waseda.jp)

Introduction: Symplectites are finely-intergrown minerals with curved surfaces which formed from rapid breakdown of a pre-existing phase. Fayalite+hedenbergite+silica symplectites have been observed in lunar and martian meteorites and in returned samples from the Moon, and are commonly attributed to breakdown of pyroxferroite [1-4]. Pyroxferroite is a pyroxenoid that forms metastably during rapid cooling of a liquid that has evolved to very low Mg/(Mg+Fe); subsequently the pyroxferroite breaks down to form fayalite+hedenbergite+silica symplectite (see [1-4]; but also see [5]). Key observations for the pyroxferroite breakdown petrogenesis are the uniform modal distribution and stoichiometry of fayalite, hedenbergite and silica, such that modal recombination of these phases yields a pyroxferroite composition [4].

Symplectite clasts have been identified in the breccia of lunar meteorite Northwest Africa 773 (NWA 773) and paired meteorites [6,7]. Many of the NWA 773 symplectites apparently formed by pyroxferroite breakdown as described above. However, deviations from silica stoichiometry in some silica-rich blebs associated with the symplectite suggest a different origin—namely, direct quenching from silicate liquid.

Analytical Methods: One polished thin section (on loan from M. Killgore of University of Arizona) was studied studied by petrographic microscope, back-scattered electron and elemental imaging, and quantitative elemental analyses. Imaging and analyses were collected using a JEOL JXA-8900 electron microprobe at Waseda University.

Results and Discussion: Several symplectite clasts with uniform distributions of hedenbergite, fayalite and silica are present in the NWA 773 breccia. One large clast has a texturally distinct core composed of a fayalite (Fa_{98}) crystal with abundant, blebby inclusions. Elemental mapping shows that the symplectite surrounding the fayalite core is essentially free of K and Al, whereas K and Al are concentrated in the blebby inclusions. The blebby inclusions do not have feldspar stoichiometry (~3.4 Si, 0.6 Al and 0.5 K atoms per 8 oxygen, respectively). Detailed mapping shows elongate SiO_2 crystals present within some inclusions. The lobate shape of the inclusions, deviations from stoichiometry and presence of silica microphenocrysts suggest an origin by direct quenching from liquid, without an intervening pyroxferroite stage.

Other lithic clasts with low Mg/(Mg+Fe) in the NWA 773 breccia are characterized by high-Ba K-feldspar [6]. This variety of evolved clasts reflects a diversity of processes during late-stage solidification of evolved lunar magma. The variety of clasts in NWA 773 may have resulted from more than one magmatic system, or from immiscibility of late-stage liquids, among other processes.

References: [1] Burnham C.W. 1971. *Proc. 2nd Lunar Sci. Conf.* p. 47-57. [2] Rubin A.E. et al. 2000. *Geology* 28:1011-1014. [3] Aramovich C.J. et al. 2002. *Amer. Mineral.* 87:1351-1359. [4] Warren P.H. et al. 2004. *Meteorit. Planet. Sci.* 39:137-156. [5] Xirouchakis D. et al. 2002. *Geochim. Cosmochim. Acta* 66:1867-1880. [6] Fagan T.J. et al. 2003. *Meteorit. Planet. Sci.* 38:529-554. [7] Zeigler R.A. et al. 2007. *Lunar Planet. Sci. Conf.* XXXVIII: Abstract #2109.

IDENTIFICATION OF SILICATE AND CARBONACEOUS PRESOLAR GRAINS IN THE TYPE 3 ENSTATITE CHONDRITE ALHA81189. S. Ebata[1], T. J. Fagan[2] and H. Yurimoto[1], [1]Department of Natural History Sciences, Hokkaido University, Sapporo 060-0810, Japan. E-mail: ebashin@ep.sci.hokudai.ac.jp ; [2]Department of Earth Sciences, School of Education, Waseda University, Tokyo, Japan.

Introduction: Primitive meteorites contain presolar silicate grains that predate the formation of our solar system [1-6]. In 2006, Ebata et al. have discovered the first evidence of presolar silicate grains from two type 3 enstatite chondrites [7]. The abundance of presolar silicates is higher in the ALHA81189. Because the sizes of presolar grains are small (~0.3 μm for silicate grains [e.g. 1, 2, 3]), presolar grains in situ determined isotopic composition and chemical composition have been limited. Here we report further in situ studies of presolar silicate and carbonaceous presolar grains in the primitive enstatite chondrite ALHA81189.

Experimental: The samples used in this study are polished thin sections of the ALHA 81189. We surveyed presolar grains by isotopography using a Hokudai isotope microscope system (Cameca ims-1270 + SCAPS [8]). For presolar grain identification, mineralogical and petrographical characterization of matrix areas containing isotopic anomalous grains has been conducted using a field emission type scanning electron microscope (JEOL JSM-7000F) equipped with energy dispersive X-ray spectrometer (Oxford INCA).

Results: The total analyzed areas of O-isotopography are ~41,000 μm^2. From the analyzed area, 10 presolar silicates were identified (volume abundance: ~22.0 ppm). Presolar carbonaceous grains were identified by C-isotopography: 7 grains in the analyzed area of ~36,600 μm^2 (volume abundance: ~17.2 ppm).

The size of presolar silicates is 0.2-0.5μm (average: ~0.33 μm) and carbonaceous grains is 0.2-1.2μm (average : ~0.55 μm). Six of presolar silicates were determined the chemical compositions (Enstatite: 2, Fe-rich pyroxene (En_{50}): 1, Fe-rich olivine (Fo_{30}): 1, SiO_2: 1, aggregates of pyroxene-like compositions: 1). The SiO_2 and aggregates may be amorphous. In the case of carbonaceous grains, three grains were determined the chemical compositions (graphite: 1, SiC: 2).

Discussion: The abundances of presolar silicate and carbonaceous grains in this study are ~60, 90% larger than the previous study [7], respectively. This is probably because of improvement of special resolution of isotopograpy using of smaller contrast aperture. The abundance is smaller than those of primitive carbonaceous chondrite and IDPs [e.g. 1, 5].

The average size of presolar silicate grains of the enstatite chondrite is comparable with carbonaceous chondrites and IDPs [e.g. 1, 2, 3]. In the case of presolar carbonaceous grains, the average size is smaller than those from carbonaceous chondrites [9]. Presolar grains of pryroxene compositions are dominant in the enstatite chondrite, whereas olivine, pryroxene and GEMS are equally distributed carbonaceous [e.g. 2, 3], IDPs [e.g. 1] and AMMs [10]. This suggests presolar silicates of enstatite composition were selectively survived in the enstatite parent body.

References: [1] Messenger et al. (2003) *Science* **300**, 105-108. [2] Nguyen and Zinner (2004) *Science* **303**, 1496-1499. [3] Nagashima et al. (2004) *Nature* **428**, 921-924. [4] Mostefaoui and Hoppe (2004) *ApJ* **613**, L149-L152. [5] Kobayashi et al. (2005) *Antarct. Meteor.* **XXIX**, 30-31. [6] Tonotani et al. (2006) *LPS* **XXXVII**, 1539. [7] Ebata et al. (2006) *LPS* **XXXVII**, 1619. [8] Yurimoto et al. (2003) *Appl. Surf. Sci.* **203-204**, 793. [9] Amari (1994) *GCA* **58**. 459-470. [10] Yada et al. (2006) *LPS* **XXXVII**, 1470.

Formation of symplectic inclusions by direct quenching of a high-FeO/(FeO+MgO) silicate liquid on the Moon. T. J. Fagan, [1]Waseda University, 1-6-1 Nishiwaseda, Shinjuku, Tokyo, Japan, fagan@waseda.jp.

Introduction:

Symplectites are fine-grained, complex intergrowths of two or more minerals sharing curved "worm-like" crystal boundaries. The intergrowths occur because of a combination of rapid breakdown of a pre-existing phase and short diffusion distances of the atoms forming the product phases [1,2]. Symplectites have been observed in terrestrial rocks and rocks returned from the Moon, as well as SNC meteorites and lunar meteorites [3-7].

Many symplectites reported from lunar and SNC meteorites and from the Apollo collection consist of intergrowths of fayalite, FeO-rich high-Ca pyroxene and a silica phase [6-9]. They are interpreted typically as the breakdown products of pyroxferroite, a metastable phase that can form during rapid cooling of a mafic silicate liquid that has evolved to compositions of high FeO/(MgO+FeO) [6-8]. Another model proposes that FeO-rich symplectites can form from exsolution and reactions among silicates and Fe-oxides [10]. In either case, the symplectites are a step removed from the true liquid compositions; thus characterization of late-stage liquids must be interpreted through intervening solid-state reactions.

Symplectites are present in lunar meteorite Northwest Africa 773 (NWA 773) and paired meteorites[9,11]. Most of these symplectites consist of intergrowths of stoichiometric fayalite, hedenbergite and silica, and I interpret them as products of breakdown of pyroxferroite (see above, and especially [8]). These formed during late stages of igneous differentiation, which resulted in the broad range of FeO/(FeO+MgO) observed in lithic clasts of the NWA 773 breccia [12]. However, some of the silica-rich symplectic phase is characterized by non-stoichiometric enrichments in K and Al. This paper proposes that this K- and Al-rich phase quenched directly from silica-rich liquid. If so, this phase allows a much more direct view of differentiated igneous liquid from the Moon (i.e., the phase quenched directly from a liquid without an intervening solid phase).

Analytical Methods:

The key observations of this study are from one polished thin section (PTS) of NWA 773 (on loan from M. Killgore of University of Arizona). An elemental map of the PTS was prepared for an earlier study [9] using a Cameca SX-50 electron microprobe at University of Hawaii. More detailed elemental and back-scattered electron (BSE) images and quantitative analyses were collected using a JEOL JXA-8900 electron microprobe at Waseda University. Quantitative analyses were collected by wavelength dispersive spectroscopy using well-characterized oxide and silicate standards and the following beam conditions: 15 kV; 20 nA; focused (0 μm) beam. Although the beam can be focused to diameters < 1 μm, the activation volumes are probably on the order of one or two μm. Thus, analyses of fine-grained, intergrown phases in the symplectite commonly yield low analytical totals.

Results and Discussion:

NWA 773 is composed of two distinct lithologies: an olivine cumulate and a breccia (Fig. 1). Several symplectite clasts are present in the breccia. One large clast is characterized by distinct relatively coarse euhedral crystals of plagioclase feldspar ($An_{70}Or_{04}$), and has a texturally distinct core composed of fayalite (Fa_{98}) with multiple inclusions. The fayalite core is surrounded by finely intergrown symplectite composed of homogeneously distributed hedenbergitic pyroxene, fayalitic olivine, and silica. Though analyses of these fine-grained minerals are different, they appear to be stoichiometric or nearly so. The Si-rich phase shows no evidence of significant enrichments in K or Al (Fig. 3). This symplectite is considered to be the equivalent of the pyroxferroite breakdown material of [7] and [8].

In contrast, the blebby, symplectite-like Si-rich inclusions in fayalite show significant enrichments in K and Al (Fig. 3). Obviously, this material is not silica. Moreover, quantitative analyses indicate that it does not match feldspar stoichiometry (~3.4 Si, 0.6 Al and 0.5 K atoms per 8 oxygen, respectively).

References:

[1] Mongoltip P. and Ashworth J.R. (1983) Jour. Petrology 24: 635-661. [2] Johnson C.D. and Carlson W.D. (1990) Jour. Metamorphic Geology 8: 697-717. [3] Papike J.J. et al. (1998) in Planetary Materials (Papike J.J., editor), Reviews in Mineralogy 36: p. 5-1 to 5-234. [4] Yanai K. and Kojima H. (1991) Proc. NIPR Symp. Antarct. Meteorites 4: 70-91. [5] Koeberl C. et al. (1993) Proc. NIPR Symp. Antarct. Meteorites 6: 14-34. [6] Aramovich C.J. et al. (2002) Amer. Mineral. 87: 1351-1359. [7] Rubin A.E. et al. (2000) Geology 28: 1011-1014. [8] Warren P.H. et al. (2004) Meteorit. Planet. Sci. 39: 137-156. [9] Fagan T.J. et al. (2003) Meteorit. Planet. Sci. 38: 529-554. [10] Xirouchakis D. et al. (2002) Geochim. Cosmochim. Acta 66: 1867-1880. [11] Zeigler R.A. et al. (2007) Lunar Planet. Sci. Conf. XXXVIII: Abstract #2109. [12] Fagan T.J. (2006) NIPR Antarct. Meteorit. XXX: 9-10.

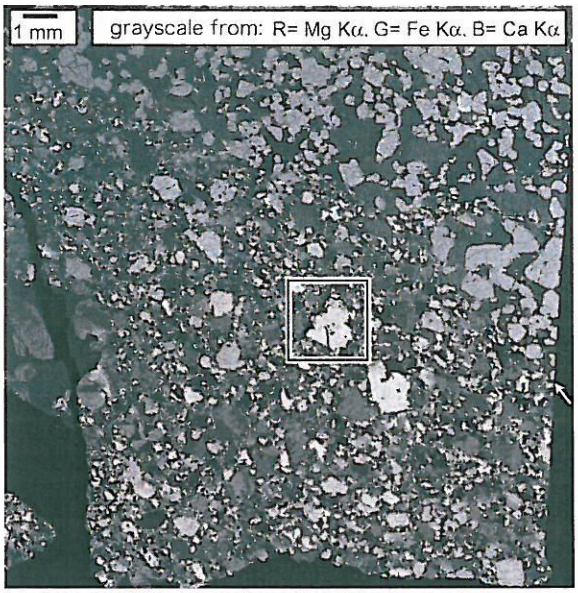

Fig. 1. NWA 773 breccia lithology shown in a grayscale image converted from R:G:B false color map with R = Mg, G = Fe and B = Ca Kα X-ray intensities. The more Fe-rich minerals appear bright in this image. Olivine cumulate lithology is in upper right portion of image (arrow at right points to boundary between cumulate and breccia). Square highlights area shown in greater detail in Fig. 2.

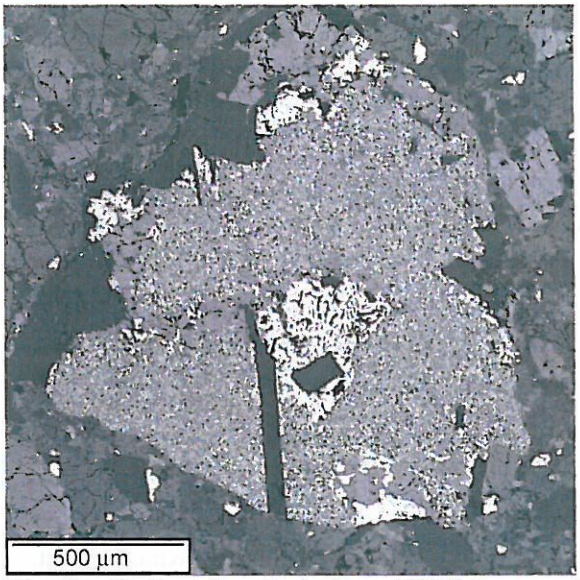

Fig. 2. Back-scattered electron (BSE) image of symplectite clast. This clast encloses a texturally distinct fayalite (Fa_{98}) with multiple inclusions (Fig. 3). Elongate, euhedral crystals with relatively dark BSE contrast are plagioclase feldspar ($An_{70}Or_{04}$).

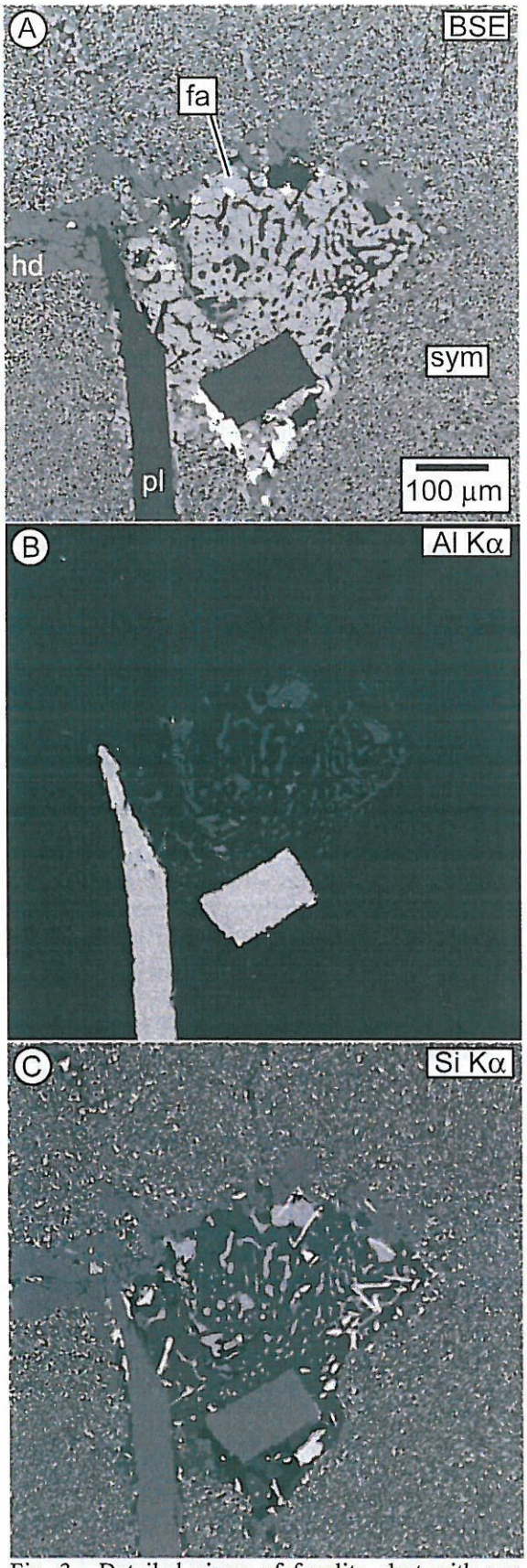

Fig. 3. Detailed views of fayalite clast with non-stoichiometric symplectic inclusions (see Fig. 2). All images at the same scale (see A). Abbreviations: fa = fayalite; hd = hedenbergite pl = plagioclase feldspar; sym = symplectite.

Mineral alteration of type B1, B2, and fluffy type A Ca-Al-rich inclusions from the Allende CV3 chondrite

Yu Tasai[1]; Hironobu Sato[1]; Timothy Fagan[1]

[1] Earth Sciences, Waseda Univ.

Calcium-aluminum-rich inclusions (CAIs) from chondritic meteorites preserve a geologic record of early solar system processes and conditions. Primary minerals from many CAIs have been partially replaced by secondary minerals; however, the physical conditions of alteration and implications for nebular and parent-body history are poorly known. This is partly due to the fine-grain size and complex textures of secondary minerals and partly due to greater research emphasis on the primary minerals.

This study focuses on secondary alteration of CAIs from the CV3 chondrite Allende. Secondary minerals have been identified previously in Allende CAIs, but their modes and distribution are poorly known, due in part to fine-grain size. In this study, modes of primary and secondary minerals were determined for one type B1 (3655A), one type B2 (4022-1) and one fluffy type A (FTA, 3529-47-1) CAI in Allende. The FTA CAI consists of several melilite-cored, diopside-rimmed nodules connected by FeO-rich silicate matrix, whereas the type B CAIs are single objects that apparently had sub-spherical form. Our thin section of 3655A consists of a wedge-shaped fragment of the original CAI.

Modes were determined using back-scattered electron (BSE) images and energy dispersive spectroscopy (EDS). BSE images of the three CAIs were collected and assembled into digital mosaics. Grids were overlain on the BSE images, and minerals on the grid cross points were identified based on BSE-brightness. Melilite, fassaite, primary anorthite, Mg-spinel, diopside, perovskite and secondary grossular were identified at this stage. Several secondary minerals, including secondary anorthite, Fe-bearing spinel, nepheline and sodalite, are fine-grained, occur together, and have similar dark appearance in BSE. These minerals were grouped together and defined as *BSE-dark minerals*. Grid points in the BSE-dark material were analyzed by SEM-EDS using the JEOL JSM-5900 secondary electron microscope at the National Institute of Polar Research (NIPR) and identified based on EDS spectra.

The modes indicate that all three CAIs were altered extensively. Approximately 25% of the original CAI minerals in the 3655A, 30% in the 4022-1 and 60% of the 3529-47-1 have been altered to form secondary minerals.

The two type B CAIs show similar patterns of alteration. Grossular is the most abundant secondary mineral in both CAIs (~20 mode% in 3655A and ~25% in 4022-1). Grossular occurs with relatively minor secondary anorthite and monticellite in veins that appear to replace melilite in both CAIs. Akermanite-rich melilite in the core of 3655A is partially pseudomorphed by grossular+monticellite+/-wollastonite. BSE-dark minerals in both type B CAIs are concentrated near the CAI margins, although some BSE-dark patches occur in the interior of 4022-1. The modes of BSE-dark minerals are minor (~2.4% in 3655A, 7% in 4022-1) relative to grossular.

CAI 3529-47-1 differs from the type B CAIs in pattern of alteration. A much higher proportion of 3529-47-1 consists of secondary minerals (~61 mode%). Furthermore, in contrast to the type B CAIs, BSE-dark minerals are more abundant (~49%) than grossular (~12%). The most abundant secondary minerals in 3529-47-1 are secondary anorthite (~21%) and Fe-bearing spinel (~18%), but nepheline (~6%) and sodalite (~1.5%) are also present.

The higher extent of alteration and greater abundance of BSE-dark minerals of the FTA CAI are due to the higher surface area of this CAI. An influx of Na, Cl and Fe occurred during BSE-dark alteration. The grossular-rich alteration veins and patches did not require this influx.

Fe-alteration of spinel in a fine-grained CAI from the Efremovka CV3 chondrite

Daiju Kashima[1]; Timothy Fagan[1]

[1] Earth Sciences, Waseda Univ.

Most calcium-aluminum-rich inclusions (CAIs) in chondritic meteorites formed initially in the solar nebula and were altered after the formation of 1^{st} -generation minerals. Alteration affected the initial isotopic and elemental compositions of 1^{st} -generation minerals. Different alteration events might have occurred in the solar nebula or in chondrite parent bodies.

This study focuses on the formation of Fe-bearing spinel in a fine-grained CAI (FGI-12) from the CV3 chondrite Efremovka. During previous work [1], variations in Fe-abundance of spinel were noted in this CAI; however, the compositional range of spinel composition was not determined. The goal of this study is to determine controls on spinel composition in FGI-12 from a systematic survey of spinel location and Fe/(Fe+Mg). The occurrence and composition of spinel grains from FGI-12 were compared with those of an adjacent coarse-grained type B1 CAI (CGI-10).

Spinel grains in the two adjacent CAIs were mapped and analyzed to evaluate variations in Fe/Mg. First, we made a back-scattered electron (BSE) mosaic of FGI-12, and identified spinel grains and composite grains larger than approximately 4 micrometer in diameter. A grid system was used to count the grains. For CGI-10, reflected light photomicrographs were collected and put together in a mosaic. A grid was placed on the mosaic and one spinel grain in each grid-box was selected for electron microprobe analysis (EPMA). Quantitative analyses of spinel grains were collected by EPMA using the JEOL JXA-8900 WD/ED combined micro-analyzer at Waseda University. Well-characterized oxides, silicates and, for one element (V), metal were used as standards, and abundances were detected by WDS. A focused beam and 15 kV accelerating voltage were used for all analyses. Analyses from FGI-12 were collected using a current of $1.0\text{x}10^{-8}$ A; a current of $2.0\text{x}10^{-8}$ A was used for analyses from CGI-10. The following elements were analyzed: Na; Mg; Al; Si; K; Ca; Ti; V; Cr; Mn; Fe; Zn. We corrected the Ti interference on V and the V interference on Cr using EPMA software.

The fine-grained CAI is approximately 1.7x1.1mm across in the plane of the thin section and consists mostly of spinel-cored nodules connected by a fine-grained diopside-rich matrix. Melilites surround some of the spinel grains. The spinel grains form irregularly shaped aggregates that range up to 30micrometer across. During EPMA some high Ca and Si contents were detected, but these are attributed to beam overlap with adjacent silicates. Spinel grains in FGI-12 are basically $MgAl_2O_4$-$FeAl_2O_4$ solid solutions. Most analyses yield less than 4.5 wt% FeO, but FeO ranges up to 9.0 wt%. Iron concentrations in spinel show a positive correlation with proximity to the CAI margin.

The coarse-grained CAI (CGI-10) has a round surface, approximately 5.0x4.4mm across in the plane of the thin section. Most of the spinel grains are approximately 5-10 micrometer across and occur as inclusions in much coarser crystals of melilite, pyroxene and anorthite. Similar to the FGI-12 spinel, the spinel from CGI-10 consists mostly of $MgAl_2O_4$-$FeAl_2O_4$ solid solution, and the more FeO-rich grains occur close to the CAI margin. However, the spinel in CGI-10 is not as Fe-rich (maximum of 2.3 FeO wt% in CGI-10).

In both CAIs, the Fe-rich spinel grains tend to occur near the edge of the CAI rim, suggesting that FeO-alteration occurred after CAI formation. The higher FeO-contents of FGI-12 are probably due to the greater porosity of this CAI. Fe-bearing spinel can form in the nebula if dust-enrichment is high. But this process should produce Cr-rich spinel [2], which was not observed. We infer that the Fe-alteration of spinel occurred after incorporation of the CAIs into the Efremovka parent body.

References: [1] Fagan T.J. et al., 2004. Meteor. Planet. Sci., 39: 1257-1272. [2] Ebel D. and Grossman L. 2000. Geoch. Cosmochim. Acta, 64:339-366.

Setting of equilibration process in the EH chondrites based on chondrule types and silica polymorphs

Sho Kataoka[1]; Timothy Fagan[1]; yuya Takahashi[1]

[1] Earth Sciences, Waseda Univ.

Metamorphism on the EH-chondrite parent body caused equilibration of many EH-chondrites; however, some steps toward equilibration may have occurred during chondrule formation and possibly other heating events in the nebula, before formation of the parent body. The purpose of this study is to distinguish between parent-body and nebular settings of equilibration in the EH chondrites. If equilibration occurred only on the parent body, then all EH chondrites should have formed initially from the same types of chondrules. If some equilibration occurred during chondrule formation, then different EH chondrites might form from variable types of chondrules.

This study investigates the setting of equilibration of EH chondrites from features of chondrules and silica polymorphs. We defined chondrule type using: texture (porphyritic, microcrystalline, barred, radial); mineral composition (olivine vs. pyroxene); shape (fragmented vs. whole); and presence or absence of a SiO^2-rich rim. Silica polymorphs were identified from Raman spectra. BSE, SEM and elemental maps were obtained by electron microprobe JEOL JXA-8900 at Waseda University and were used to characterize chondrules. Raman spectra were obtained by Jobin Yvon LabRam300 micro-spectrometer (HORIA) and air cooled CCD detector at Waseda University. Chondrule types were identified in polished thin sections of the following chondrites: four EH3 chondrites (ALHA81189; MET 01018; ALH 84170; PCA 82518) and one EH5 chondrite (St. Marks).

The chondrules in St. Marks have hazy, recrystallized boundaries, whereas chondrules in the EH3 chondrites have sharp, well-defined boundaries and are easy to recognize. Chondrules with SiO^2-rich rims and olivine phenocrysts were identified in all of the EH3 chondrites. On the other hand, no olivine-bearing chondrules and no chondrules with SiO^2-rich rims were identified in St. Marks. In fact, no olivine was identified at all in St. Marks. Silica is present in St. Marks, but as relatively coarse, subhedral to euhedral crystals, in contrast to the fine silica grains present in the EH3 chondrites. The only silica polymorph identified in St. Marks is quartz. This indicates St. Marks equilibrated at relatively low temperature or slow cooling rate. The differences between the EH3s and St. Marks are in all probability due to parent-body metamorphism.

Among the EH3s, ALHA81189 has high percentage of olivine-bearing chondrules (58%) and of chondrules with SiO2-rich rims (43%). The other EH3 chondrites are composed mainly of pyroxene-rich, olivine-absent chondrules (~85%) with fewer SiO^2-rich rims (20% or less). ALHA81189 is also distinct from the other EH3 chondrites based on chondrule shapes. In ALHA81189 ~35% of the chondrules identified are whole, whereas only ~10% of chondrules in the other EH3s appear to be unfragmented.

These features indicate that ALHA81189 is distinct from the other EH3 chondrites and relatively unequilibrated; however, the only silica polymorph identified in ALHA81189 was cristobalite. In contrast, in ALH 84170, cristobalite, tridymite and quartz all are present (also see [1]).

The silica from ALHA81189 experienced rapid cooling from high temperatures suggestive of chondrule formation. Much of the silica in ALH 84170 had a similar origin, but the presence of quartz indicates some silica in this meteorite formed at higher pressures, lower temperatures or lower cooling rates. The best candidate for the origin of the ALH 84170 quartz is parent-body metamorphism; however, this meteorite is unequilibrated, suggesting that the quartz formed during metamorphism prior to accretion of the ALH 84170 parent body. The presence of quartz in ALH 84170 indicates that ALH 84170 was derived from materials that experienced parent-body processing. In contrast, ALHA81189 formed from material processed mostly during chondrule formation.

Reference: [1] Kimura et al. (2005) Meteorit. & Planet. Sci. 40, 855-868.

Setting of Na-alteration in a type B2 Ca-Al-rich inclusion from the Allende CV3 chondrite

Timothy Fagan[1]; Mikiko Kudou[1]

[1] Earth Sciences, Waseda Univ.

http://www.dept.edu.waseda.ac.jp/earth/index_j.html

Ca-Al-rich inclusions (CAIs) in chondritic meteorites are recognized as primitive rocks with petrologic and isotopic records of high-temperature interactions between gas and condensed phases in the solar nebula. Many CAIs have also undergone low-temperature alteration, which may have occurred in their asteroidal parent bodies, or during earlier thermal events in the solar nebula, or in both nebular and parent-body settings. Determining the settings of alteration and thermal histories of CAIs remain major goals for understanding the formation and re-processing of rocks in the solar nebula and parent bodies.

This study focuses on the Na-alteration of melilite in a type B2 CAI (4022-1) from the CV3 chondrite Allende. Melilite with high Na_2O (0.28 wt%) and FeO (0.32 wt%) contents was discovered near the margin of this CAI. Yet, within 30 micrometers, both Na_2O and FeO are below electron microprobe analysis (EPMA) detection limits (0.03 wt% for Na_2O and 0.08 wt% for FeO). This discovery prompted a search for correlations between Na_2O, FeO and akermanite (Ak) content and location within this CAI.

Methods: Three sets of melilite analyses were collected: (1) near the rim of CAI 4022-1, where the secondary minerals grossular, secondary anorthite, FeO-bearing spinel and feldspathoids are abundant; (2) at randomly selected sites throughout the CAI; (3) at sites throughout the core and rim of a type B1 CAI (CGI-10, see [1]) from Efremovka. Back-scattered electron (BSE) images and quantitative EPMA were collected using the JEOL JXA-8900 electron microprobe at Waseda University. Analyses were conducted by WDS using a 15 kV focused beam with currents of 10 nA or 20 nA, and counting times of 10 s on peak and background. Oxides and silicates were used as standards.

Results and Discussion: Melilite with elevated Na_2O (0.15 wt%) and FeO (0.2 wt%) occur throughout the Allende type B2 CAI (4022-1), though the highest Na_2O- and FeO-contents (0.40 and 0.36 wt%, respectively) occur near the CAI margin. Comparable compositions are present near the rim of the Efremovka type B1 CAI (CGI-10), but melilite in the interior of CGI-10 is relatively depleted in Na2O and FeO. Most analyses show a correlation between Na2O and Ak-content; however, several exceptions to this trend occur near the margin of CAI 4022-1. Iron and Na_2O concentrations show a positive correlation for the CGI-10 and 4022-1 near-rim analyses, but no correlation between Na_2O and FeO was detected for the analyses collected throughout 4022-1.

The two Na_2O vs. FeO trends indicate two mechanisms for alteration of CAI 4022-1 melilite. The positive correlation between Na_2O and FeO in melilite near the CAI rim suggests that this alteration was coincident with formation of feldspathoids and FeO-bearing secondary minerals along the margin of the CAI. Sodium and Fe may have been incorporated into melilite by a combination of fluid-assisted diffusion and local recrystallization. Exceptions to the Na_2O-Ak correlation are gehelenitic melilites that occur near the CAI rim and incorporated Na_2O during this alteration event. A similar event affected melilite in Efremovka CGI-10.

Sodium and FeO are uncorrelated in melilite in the interior of CAI 4022-1. Our favored hypothesis for alteration of this melilite depends on an early Na-alteration event in the solar nebula followed by incomplete melilite melting, recrystallization and diffusive relaxation [2-4]. This model accounts for the efficient dispersal of Na to melilite throughout the CAI.

References: [1] Fagan T.J. et al. 2004 Meteorit. Planet. Sci. 39: 1257-1272. [2] MacPherson G.J. and Davis A.M. 1993 Geochim. Cosmochim. Acta 57: 231-243. [3] Beckett J.R. et al. 2000 Geochim. Cosmochim. Acta 64: 2519-2534. [4] Simon S.B. and Grossman L. 2006 Meteorit. Planet. Sci. 39: 1257-1272.

Timothy J. Fagan
Formation of symplectites by liquid-solid and solid-solid reactions during cooling of an FeO-enriched magma on the Moon (*in* Geological Society of America, Northeastern Section, 42nd annual meeting, Anonymous,)
Abstracts with Programs - Geological Society of America (March 2007), 39(1):40

Abstract 1 of 1

Formation of symplectites by liquid-solid and solid-solid reactions during cooling of an FeO-enriched magma on the Moon

Timothy J. Fagan
Geological Society of America (GSA), United States, Boulder, CO

Northwest Africa 773 (NWA 773) is a lunar meteorite composed of an olivine cumulate lithology and a heterolithic breccia. Many fragments in the breccia are plausibly linked with the cumulate and appear to have formed by Fe-enrichment during igneous differentiation of a single magmatic system (Fagan et al., 2003, Meteoritics and Planetary Science v. 38, 529-554). Accepting this interpretation, lithic and mineral clasts in this single sample preserve a record of igneous differentiation on the Moon. Lithic clasts in the breccia with hedenbergite, fayalite and silica or a silica-rich phase formed from a late stage liquid with extremely enriched FeO/(FeO+MgO). In many clasts, these minerals are intricately intergrown, forming symplectite textures. Most of the symplectites are characterized by uniform distributions of hedenbergite, fayalite and silica-all having curved, finely intergrown crystal boundaries, such that individual "grains" appear to be no more than 2 or 3 mu m across. Hedenbergite-fayalite-silica-symplectites have been reported from lunar and martian meteorites and are frequently, although not universally, interpreted as the breakdown products of metastable pyroxferroite (Ca1/7Fe6/7SiO3). The solid state breakdown of pyroxferroite is a plausible origin for the fine-grained symplectites in NWA 773; however, a slightly coarser grained symplectite-like texture apparently formed by direct interactions with late-stage liquid. In this texture, fayalite, which may be in direct contact with fine-grained symplectite, hosts multiple amoeboid SiO2-rich inclusions, resulting in a symplectite-like appearance. Several of the inclusions are wide enough for electron microprobe analyses and show significant deviations from silica stoichiometry (Al2O3 approximately 12 wt.%; K2O approximately 9 wt.%). Some inclusions contain silica, as well as the non-stoichiometric phase. These amoeboid symplectite-like inclusions are interpreted as quenched melt trapped by fayalite that crystallized directly from FeO-rich silicate liquid. The silica within the inclusions also crystallized directly from the melt. This symplectite-like texture did not form by pyroxferroite breakdown, but rather from direct crystallization and quenching of silicate liquid.

CORRELATION BETWEEN TEXTURE AND OXYGEN ISOTOPIC SYSTEMATICS IN CAIS FROM ACFER 094. T. J. Fagan[1], A. N. Krot[2], S. Kobayashi[3], and H. Yurimoto[3]. [1]Dept. Earth Sciences, Waseda University, 1-6-1 Nishiwaseda, Shinjuku, Tokyo 169-8050, Japan (fagan@waseda.jp), [2]Hawai'i Institute of Geophysics and Planetology, SOEST, University of Hawai'i at Manoa, Honolulu, HI 96822, USA. [3]Department of Natural History Sciences, Hokkaido University, Sapporo 060-0810, Japan.

Introduction: Ca-Al-rich inclusions (CAIs) in chondritic meteorites are associated with ^{16}O-rich oxygen isotopic compositions near –40‰ in both δ^{18}O and δ^{17}O [1-3]. In spite of this general association, there are significant variations toward isotopically heavier compositions both on the scale of minerals in CAIs and whole CAIs. Petrogenetic causes of these isotopic fluctuations and implications for nebular and chondritic parent body histories remain outstanding issues, in part because of the difficulty of disentangling parent-body from nebular effects. CAIs from the ungrouped carbonaceous chondrite Acfer 094 are ideally suited for evaluating pre-parent-body isotopic variations because of the unequilibrated pristine nature of this meteorite [4,5].

In this study, we present petrologic and isotopic evidence that some of the CAIs in Acfer 094 experienced a change in isotopic setting from the ^{16}O-rich compositions associated with CAIs to the ^{16}O-poor compositions associated with other chondrite components. Diopside rims formed on some of the Acfer 094 CAIs in a ^{16}O-poor setting prior to assembly of the Acfer 094 parent body. However, other CAIs in Acfer 094 did not undergo such rim formation, confirming the inference that CAIs in Acfer 094 were drawn from diverse populations with distinct thermal histories [6,7].

Analytical Methods: CAIs in one thin section of Acfer 094 (provided by A. Greshake) were identified by elemental X-ray mapping using the Cameca SX-50 electron microprobe at University of Hawai'i at Manoa (UHM). Additional characterization of the CAIs was conducted using scanning electron microscopes outfitted with BSE and EDS detectors at UHM, Tokyo Institute of Technology (TiTech) and Hokkaido University (Hokudai). Major element compositions of CAI minerals were determined by electron microprobe (Cameca SX-50) analyses at UHM using oxide and silicate standards. Detailed BSE imaging and elemental mapping of one CAI with a ^{16}O-poor diopside rim were collected using a field emission SEM at Hokudai.

Oxygen isotopic data were collected using the Cameca ims-1270 SIMS system that was formerly located at TiTech. This SIMS has subsequently been moved to Hokudai. Point analyses were collected at TiTech using conditions described previously [2]. Oxygen isotopic ratio mapping was conducted at Hokudai using the ims-1270 + SCAPS [8].

Results: Of 132 Acfer 094 CAIs identified by [6]: one is a pyroxene-hibonite (pyx-hib) spherule; one is rich in corundum; two are rich in hibonite (hib); 16 in grossite (gro); 17 in pyx+anorthite (an); and 95 in spinel+melilite (sp+mel). The CAIs have not been affected by Fe-alkali metasomatism. Most of the CAIs are zoned, with more refractory minerals in cores and less refractory rims. (An exception to the refractory core/less refractory rim pattern is the occurrence of spinel in cores and melilite in rims. This texture for spinel and melilite is widely reported and yet unexplained [e.g., 9]).

There are differences in the core-to-rim textures though: many of the melilite rims appear to drape continuously around core minerals (Fig. 1 A,B), whereas diopside rims tend to form a discontinuous break with the more refractory cores (Fig. 1 C,D). In many cases, a thin layer of anorthite ±melilite intervenes between diopside rim and refractory core (Fig. 1D).

Point oxygen isotopic analyses indicate that most CAI minerals are relatively ^{16}O-rich, but one analysis of rim diopside around a grossite-rich, spinel+hibonite-bearing CAI yields a ^{16}O-poor value (Fig. 2). The refractory core of this CAI is separated from the diopside rim by a layer of anorthite that replaced melilite (Fig. 1D). Grossite and spinel of this CAI are ^{16}O-depleted compared to other CAIs (Fig. 2). The two-dimensional oxygen isotopic distribution determined by SCAPS verifies the isotopic composition of the diopside rim (Fig. 3), indicating that the rim formed in a ^{16}O-poor setting. The sharp break in isotopic composition between CAI core and rim indicates that the diopside formed during a short-lived thermal event. These results combined with the primitive nature of Acfer 094 indicate that the set of CAIs in this meteorite experienced diverse thermal histories in distinct oxygen isotopic settings prior to assembly on the Acfer 094 parent body.

References: [1] Clayton R.N. et al. (1973) *Science, 182,* 485-488. [2] Yurimoto H. et al. (1998) *Science, 282,* 1874-1877. [3] MacPherson G.J. (2003) in *Meteorites, Comets and Planets* (ed. A.M. Davis) vol. 1, *Treatise on Geochemistry* (eds. H.D. Holland and K.K. Turekian), pp. 201-246. [4] Newton J. et al. (1995) *Meteoritics, 30,* 47-56. [5] Greshake A. (1997) *GCA, 61,* 437-452. [6] Krot A.N. et al. (2004) *GCA, 68,* 2167-2184. [7] Fagan T.J. et al. (2003) *LPS XXXIV,* Abstract #1274. [8] Yurimoto H. et al. (2003) *Appl. Surf. Sci., 203-204,* 793-797. [9] Krot A.N. et al. (2004) *MaPS., 39,* 1517-1553.

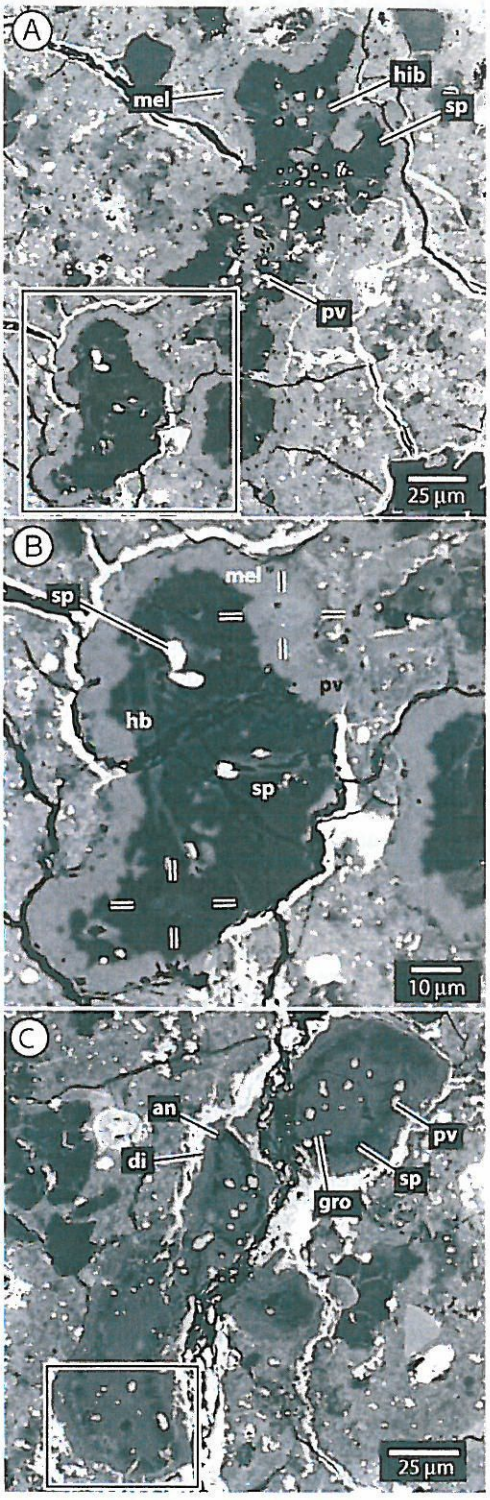

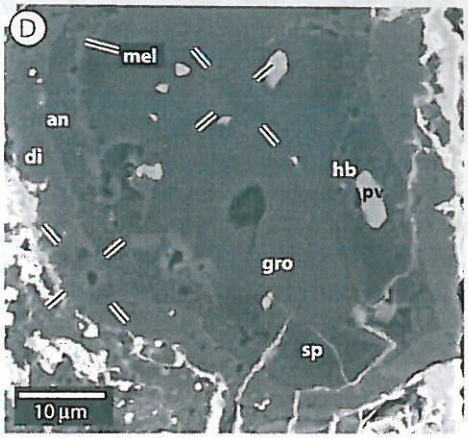

Fig. 1. BSE images of CAIs RO-89 (A,B) and RO-64 (C,D). Pits excavated by SIMS highlighted (B,D). an = anorthite; di = diopside; gro = grossite; hb = hibonite; mel = melilite; pv = perovskite; sp = spinel

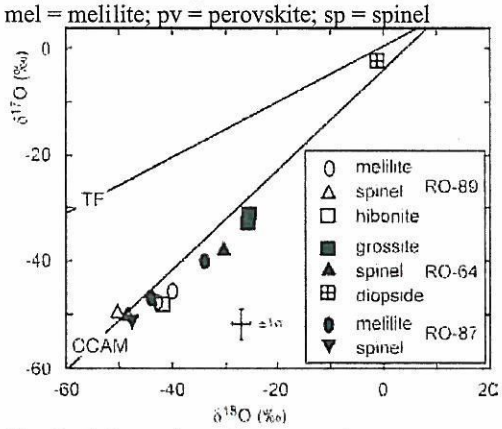

Fig. 2. Point analyses for oxygen isotopes.

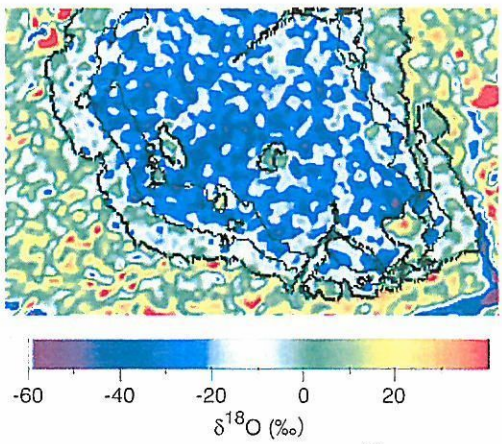

Fig. 3. SCAPS isotopography showing ^{16}O-poor diopside rim of RO-64. Compare with 1D.

Fe-enrichment vs. Si-enrichment trends in two samples from the Moon

T.J. Fagan[1]
[1]Department of Geology, Waseda University, 1-6-1 Nishiwaseda, Shinjuku, Tokyo, 169-8050, Japan
fagan@waseda.jp

Major silicate minerals in breccia clasts from the lunar meteorite NWA 773 show a range of compositions that can be explained by extreme Fe-enrichment during magmatic differentiation. Clasts in Apollo sample 15405 have also been interpreted as resulting from igneous differentiation (Ryder, 1976, EPSL v. 29, 255-268), though in this sample silica-rich clasts have mafic silicates with intermediate Mg/(Mg+Fe). This study reviews the evidence for magmatic differentiation in these rocks and speculates on the controls of magmatic trends on the Moon.

NWA 773 is composed of two rock-types: an olivine cumulate gabbro and a heterolithic breccia (Fagan et al., 2003, MaPS v. 38, 529-554). Major phases in the olivine gabbro include olivine (Fo_{68}), pigeonite ($Wo_{11}En_{65}$), augite ($Wo_{36}En_{50}$) and plagioclase, with minor K,Ba-feldspar, ilmenite, troilite and Ca-phosphates. Co-magmatic clasts in the breccia consist of gabbros, FeO-rich lithic clasts and symplectites. Pyroxene exhibits a continuous variation in Mg/(Fe+Mg) in these lithologies from ~0.75 to 0.05. Likewise, pyroxene Ti/(Cr+Ti) shows a continuous variation from ~0.2 to 1.0. Olivine records only a part of the Fe-enrichment trend, with a gap in the occurrence of olivine between ~Fo_{55} to Fo_{15}. Silica and K,Ba-feldspar occur in some, but not all, clasts with fayalitic olivine. Some of the FeO-rich clasts have symplectic intergrowths of fayalite, hedenbergite, and silica or a non-stoichiometric silica-rich phase.

Reported results (Ryder, 1976) from Apollo sample 15405 show a range in augite and pigeonite compositions from Mg/(Mg+Fe) as high as 0.8 in basaltic clasts to values near 0.3 in granitic clasts. The main difference between the NWA 773 and 15405 trends is the timing of free silica relative to Fe-enrichment in mafic silicates and is comparable to tholeiitic and calc-alkaline trends on Earth.

One controlling factor in the terrestrial systems is hypothesized to be oxygen fugacity. In high-$f(O_2)$ systems, Fe precipitates in oxide minerals, driving the residual liquid to more SiO_2-rich compositions with relatively small changes in silicate mineral Mg/(Mg+Fe). In low-$f(O_2)$ systems, Fe speciates in mafic silicates, resulting in a broad shift in silicate Mg/(Mg+Fe) with minor variation in silica during differentiation.

Oxygen fugacity is a possible control in lunar magmatic systems, but may drive magmatic crystallization in opposite directions to those observed on Earth. With the lower $f(O_2)$ of the Moon, Fe can be displaced from the silicate assemblage by precipitation as Fe-metal or Fe-sulfides.

A record of extreme FeO/(MgO+FeO) enrichment during igneous crystallization on the Moon preserved in lunar meteorite Northwest Africa 773. T. J. Fagan, [1]Department of Earth Sciences, Waseda University, 1-6-1 Nishiwaseda, Shinjuku, Tokyo, 169-8050, Japan (fagan@waseda.jp)

Introduction:

The evolution of major element compositions in typical igneous suites on Earth involve progressive enrichment in SiO_2 and increase in FeO/(FeO+MgO). In the tholeiitic trend, FeO/(FeO+MgO) increases to high values prior to significant SiO_2-enrichment, whereas SiO_2-enrichment dominates in the calc-alkaline trend. Oxygen fugacity, among other variables, has been postulated as a control on whether a given magmatic system follows a tholeiitic or a calc-alkaline trend (e.g., [1]). These trends lead to distinct types of rocks in later stages of differentiation, even though initial compositions might have been similar.

In this study, a tholeiitic-type trend is inferred from the breccia of lunar meteorite Northwest Africa 773 (NWA 773). Lithic fragments in the breccia show a textural similarities and a progressive increase in FeO/(FeO+MgO), suggesting that they formed as part of a single evolving magmatic system on the Moon [2,3]. Free silica occurs in rocks which have attained high FeO/(FeO+MgO). This trend is roughly analogous to the terrestrial tholeiitic trend. In contrast, granitic rocks (with free silica, K-feldspar and relatively albitic plagioclase) in Apollo 15 sample 15405 are characterized by pyroxene with moderate FeO/(FeO+MgO) [4,5]. The contrast between granitic clasts in NWA 773 and those in 15405 suggest that lunar magmatic systems evolved by different extents of SiO_2- and FeO/(FeO+MgO)-enrichment.

In a general sense, these trends are comparable to terrestrial calc-alkaline and tholeiitic trends. However, oxygen fugacity may be associated with the opposite trend on the Moon. Namely, systems with relatively high $f(O_2)$ on the Moon might evolve along a tholeiitic path.

Analytical Methods:

Two polished thin sections of NWA 773 were studied using standard petrographic techniques. Major element compositions of minerals were determined by electron microprobe analysis (EPMA) using a Cameca SX-50 instrument at the University of Hawaii at Manoa [2]. The Cameca SX-50 was also used to collect X-ray elemental maps and back-scattered electron images at a variety of scales.

Igneous differentiation of NWA 773 breccia:

Petrologic, geochemical, noble gas and oxygen isotopic data were used to document NWA 773 as a lunar meteorite in 2003 [2]. The meteorite is composed of a gabbroic lithology with olivine cumulate texture and a fragmental breccia (Fig. 1). Sm-Nd data from the olivine cumulate yield the youngest igneous age (~2.87 Ga) of any analyzed rock from the Moon [6]. A petrologic connection with very-low-Ti basalts [3] and pairings with more recently found meteorites [7] have been proposed.

A variety of clasts occur in the NWA 773 breccia, including: gabbro; zoned two-pyroxene clasts, ferroan gabbroic to granitic rocks (Fig. 2); silica-hedenbergite-fayalite symplectite; and rocks with transitional symplectic textures. Gabbroic lithic clasts have mineral textures and olivine-hosted melt inclusions similar to those in the gabbro lithology. Pyroxene and olivine compositions range from identical to those of the gabbro lithology ($Wo_{11}En_{65}$, $Wo_{35}En_{50}$, Fo_{68}) to somewhat more ferroan values (Fig. 3). Pigeonitic pyroxene shows a continuous spread in major element composition to near Fe-endmember compositions (Fig. 3). In contrast, olivine with intermediate compositions is not observed, but ferroan olivine coexisting with silica ±K,Ba-feldspar occurs in symplectite and coarse-grained clasts (Figs. 2,3). K,Ba-feldspar is also present in inter-cumulus domains enriched in incompatible elements in the gabbro [2].

From the textural similarities and trends in mineral composition and assemblages, these types of breccia clasts are interpreted as products of progressive differentiation in a magmatic system that formed the gabbro at early stages [2,3]. Differentiation resulted in silica-bearing rocks, but only after extensive FeO/(FeO+MgO)-enrichment in pyroxene (Fe# > 65 in symplectite, Fe# > 85 in coarser-grained clasts; see Fig. 3).

In contrast, silica-bearing clasts from Apollo 15 coexist with more magnesian pyroxene (Fig. 3), suggesting different proportions of increase in SiO_2-content and FeO/(FeO+MgO) in different magmatic systems on the Moon. As has been suggested for terrestrial systems [1], oxygen fugacity may be a significant variable determining between these two trends. On Earth, relatively high $f(O_2)$ results in formation of Fe-oxides, removing Fe from the silicate system, leading to SiO_2-enrichment. On the Moon, relatively high $f(O_2)$ may diminish the role of metal and sulfides, increasing the Fe available to silicate minerals, leading to tholeiitic-like FeO/(FeO+MgO) enrichment (also see [8]).

References:

[1] Yagi K. and Takeshita H. (1987) in Magmatic processes: Physicochemical principles (Mysen B.O., ed.) p. 183-190. [2] Fagan T.J. et al. (2003) MaPS 38, 529-554. [3] Jolliff B. et al. (2003)

GCA 67, 4857-4879. [4] Ryder G. (1976) *EPSL 29*, 255-268. [5] Meyer C. et al. (1996) MaPS 31, 370-387. [6] Borg L.E. et al. (2004) Nature 432, 209-211. [7] Bunch T.E. et al. (2003) LPSC XXXVII, #1375. [8] Snyder G.A. et al. (1999) LPSC XXX, #1499.

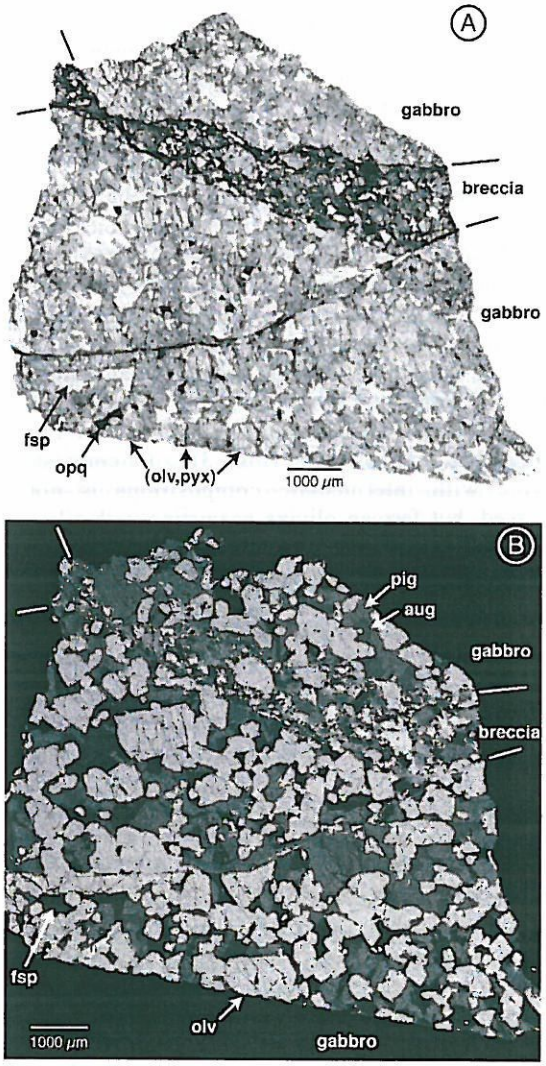

Figure 1. Olivine cumulate gabbro and breccia textures in one thin section of NWA 773. (A) Transmitted light (not plane-polarized). Olivine and pyroxenes appear similar, with higher relief than feldspar. (B) False-color elemental map (R=Mg, G=Fe, B=Ca Kα), reduced to gray-scale. Abbreviations: aug = augite; fsp = feldspar; olv = olivine; opq = opaque minerals; pig = pigeonite.

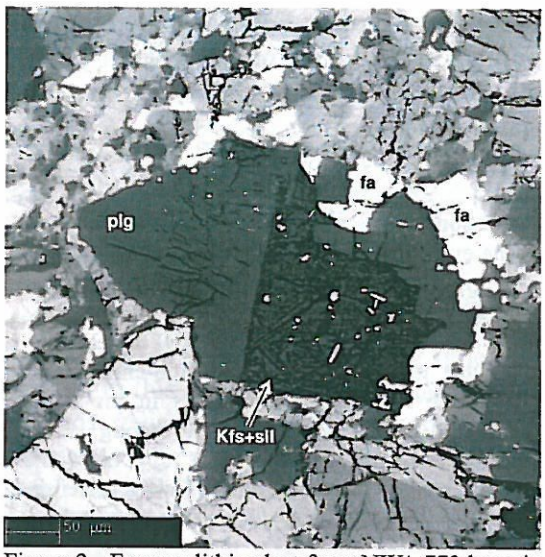

Figure 2. Ferroan lithic clast from NWA 773 breccia. Back-scattered electron image. Mineral abbreviations: fa = fayalite (Fa_{97}); Kfs+sil = K-feldspar intergrown with silica; plg = plagioclase feldspar (An_{72}).

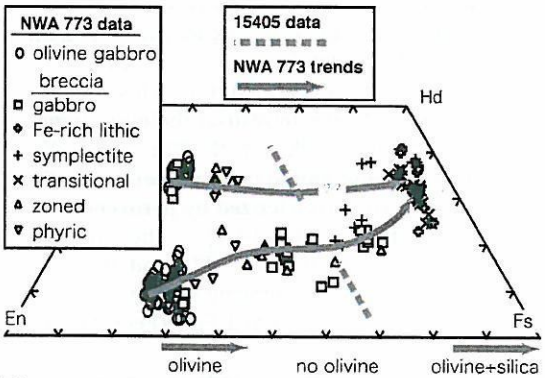

Figure 3. Pyroxene "quadrilateral" (Di-Hd-En-Fs) showing compositional variations in pyroxene from NWA 773 olivine gabbro and breccia, and from Apollo sample 15405 (thin sections 57 and 145, data from [3,4]). Pyroxene from a variety of clast types in NWA 773 breccia were analyzed, including gabbro, FeO-rich lithic fragments, symplectite, transitional symplectite, a zoned pyroxene mineral clast, and a pyroxene-phyric basalt. Individual analyses for 15405 are not plotted. Compositional ranges for olivine and olivine coexisting with silica in NWA 773 are also shown. Compositional trends for NWA 773 are shown.

Mineralogy and petrography of the oxidized CV chondrite Yamato 86009. M. Komatsu[1], A. N. Krot[2], T. Fagan[3], M. Miyamoto[1], T. Mikouchi[1], and K. Keil[2], [1]Department of Earth & Planetary Science, University of Tokyo, Japan (mutsumi@um.u-tokyo.ac.jp), [2]Hawaii Institute of Geophysics and Planetology, University of Hawaii at Manoa, USA, [3]Department of Earth Sciences, School of Education, Waseda University, 1-6-1 Nishiwaseda Shinjuku-ku Tokyo, Japan.

Introduction: The CV chondrites are subdivided into the oxidized Allende-like (CV_{oxA}), oxidized Bali-like (CV_{oxB}), and reduced (CV_{red}) subgroups [1]. In both oxidized subgroups, common secondary minerals in chondrules, CAIs, and matrices include magnetite, Ni-rich metal, Fe,Ni-sulfides, Ca,Fe-rich pyroxenes, and andradite. Phyllosilicates and fayalite ($Fa_{>90}$) are common in the CV_{oxB} (e.g., Bali, Kaba, Mokoia), whereas secondary fayalitic olivine (Fa_{30-50}), nepheline, and sodalite are observed largely in the CV_{oxA} (e.g., Allende, ALH84028) [2,3]. Secondary minerals in the CV_{red} chondrites Efremovka and Leoville are similar to those in the CV_{oxA}, but much less abundant.

It has been previously suggested that the major chemical and mineralogical differences between the CV subgroups largely reflect their complex alteration [4]. In order to understand the alteration history of the CV chondrites, we performed mineralogical studies of the Yamato 86009 CV3 carbonaceous chondrite.

Analytical methods: Two polished thin sections of Yamato-86009, 51-1 and 51-2 were studied by optical microscopy and in the BSE mode with Hitachi S-4500 and JEOL 5900LV scanning electron microscopes. Chemical analyses and X-ray maps were obtained using JEOL JCM-733, JX-8900, and Cameca-SX50 electron microprobes.

Results: Y-86009 consists of chondrules (53 vol%), AOAs (2 vol%), Ca-Al-rich inclusions (1 vol%) and fine-grained matrix (43 vol%) with isolated mineral fragments (1 vol%).

Chondrules: Chondrules in Y-86009 cover various textural types (porphyritic, barred and cryptocrystalline), size ranges (50 μm–1.1 mm), and shapes (spherical and fragmental). Type I chondrules in Y-86009 consist of magnesian olivine ($Fo_{>90}$) and low-Ca pyroxene phenocrysts, opaque nodules and glassy mesostasis with or without high-Ca pyroxene. Most of anorthite-normative mesostasis is partly replaced by Al-bearing phyllosilicates, nepheline and sodalite. The opaque nodules consist of Fe-Ni-sulfides and magnetite extensively replaced by ferrous ($Fa_{>70}$) olivine and, occasionally, Ca-Fe-rich pyroxenes. Fayalite grains in the outer portion of chondrules show inverse compositional zoning zoning (Fig. 1a). Occasionally, fine-grained rims around Type I chondrules are crosscut by fayalite-magnetite-sulfide veins, which typically start at the opque nodules and extend into the Y-86009 matrix (Fig. 1b).

AOAs: AOAs are irregularly-shaped objects, 50-750 μm in size, composed of anhedral, fine-grained (1-20 μm) olivines and refractory, Ca-Al-rich nodules. The degree of alteration varies between individual AOAs. Lightly-altered AOAs (Fig. 2) consist of nearly pure forsterite ($Fo_{>98}$), high-Ca pyroxene, anorthite ± spinel (FeO < 1 wt.%). Anorthite is partly replaced by phyllosilicates (Fig. 2), but it is much less common than in heavily-altered AOAs. In some cases, enstatite (Wo_5En_{94}) is present around the metal-magnetite nodules. Lightly-altered AOAs are texturally similar to AOAs in Y-81020 (CO3.0), except having phyllosilicates and magnetite. Representative analyses of primary minerals of AOAs from Y-86009 are listed in Table 1.

Heavily-altered AOAs have porous textures, and are mainly composed of fine-grained forsteritic olivine (Fo_{96-99}) and Al-diopside (Fig. 4). They typically show enrichment in FeO along the cracks and grain boundaries. Anorthite is rare and largely replaced by fine-grained Mg-Al-silicates, which although are too small to be analyzed by EPMA, appear to be similar in BSE images to phyllosilicates described in CAIs from Mokoia [5], Bali and Kaba [6]. The anhderal grains of Ca-Fe-rich pyroxene (hedenbergite?) occur along grain boundaries. Euhedral fayalitic olivine grains (Fa_{63-71}) overgrow forsterite. Hedenbergite and fayalite are occasionally observed in direct contact with phyllosilicates. Occasionally, fayalite grains are rather coarse and show inverse compositional zoning (Fig. 3b). Some forsterite grains are overgrown by euhedral pyroxene ($Wo_{41}En_{56}Fs_3$, <10 μm in size) along the rim of AOAs. This type of pyroxene has higher content of MnO and Cr_2O_3 (~1.9 wt%) than Al-diopside associated with spinel in the interior of the AOA.

CAIs: Most CAIs are porous and consist of spinel (FeO < 1 wt%) and Al-diopside. Melilite and anorthite are probably replaced by Al-phyllosilicates.

Matrices: Matrix is dominated by platy, lath-shaped and irregular-shaped fayalitic olivine crystals (1-5 μm, Fa_{30-50}). The grain sizes of matrix olivine are larger than those in CV_{oxB}, but much smaller than those in CV_{oxA}. Some irregularly-shaped fayalitic olivines in the matrix show normal Mg-Fe zoning (Mg-rich core and Fe-rich rim) which is also observed in the Allende matrix. Texturally, the matrix appears to be intermediate between CV_{red}, CV_{oxA} and CV_{oxB} [7].

Discussion: Based on our observations, we infer that Y-86009 experienced hydrous alteration that resulted in formation of secondary phyllosilicates, magnetite, Fe-Ni-sulfides, fayalite, Ca-Fe-rich pyroxenes, and andradite These alteration features are similar to those in the CV_{oxB} chondrites Bali and Mokoia [9]. However, there are some important mineralogical differences as well. The common presence of anorthite in AOAs and rarity of Fa_{100} implies that the degree of aqueous alteration is lower than other CV_{oxB} chondrites. In addition, secondary fayalite in Kaba is rarely shows inverse compositionally zoning and approaches nearly pure fayalite. The presence of nepheline, sodalite and lath-shaped fayalitic olivine in matrix implies that Y-86009 also experienced higher temperature, and possibly more prolonged aqueous alteration than Kaba. We infer that Y-86009, like MET00430 [7], is intermediate between CV_{oxA} and CV_{oxB}. Indeed, inverse chemical zoning of the individual ferrous olivines are similar to those in MET00430 [7], suggesting the dissolution of ferrous olivine and precipitation of more forsteritic olivine from a fluid phase during the late-stage thermal

metamorphism, and probably reflect fluctuations of fluid compositions on a local scale [9].

References: [1] Weisberg M. K. et al. (1997) *Meteorit. Planet. Sci., 32,* A138. [2] Kojima H. and Tomeoka K. (1996) *Geochim. Cosmochim. Acta, 60,* 2651-2666. [3] Krot A. N. et al. (1998) *Meteorit. Planet. Sci., 33,* 623-645. [4] Krot A. N. et al. (1995) *Meteoritics, 30,* 745-775. [5] Krot A. N. et al. (1998) *Meteorit. Planet. Sci., 33,* 1065-1085 [6] Cohen R. E. et al. (1983) *Geochim. Cosmochim. Acta, 41,* 1739-1757. [7] Krot A. N. et al. (2003) *International Symp. Evolution of Solar System Materials,* 61-62. [8] Kimura M. and Ikeda Y. (1998) *Meteorit. Planet. Sci., 33,* 1139-1146. [9] Krot A. N. et al. (2004) *Antarct. Meteorit. Res., 17,* 153-171.

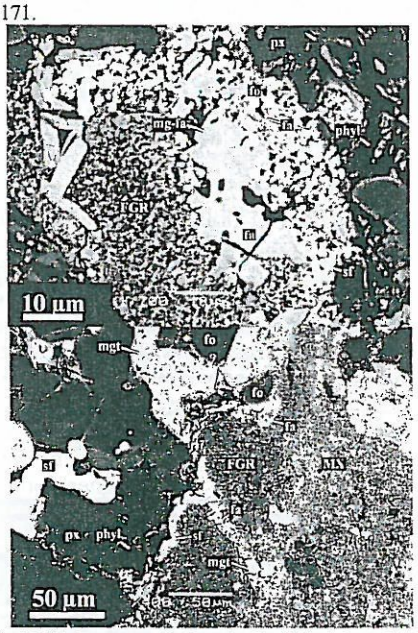

Fig. 1. BSE images of chondrule #51 (a) and #52 (b). (a) Opaque nodule in the chondrule preriphery is replaced by sulfide (sf) and magnetite (mgt); the latter is replaced by fayalite (fa), which in turn is replaced by a more magnesian olivine. (b) Fayalite-magnetite-sulfide veins starting at the opaque nodules and crosscutting the fine-grained rims around the chondrule. px=pyroxene, FGR=fine-grained rim, MX-matrix.

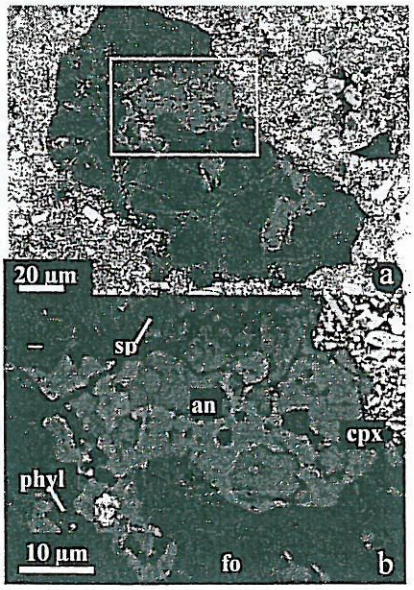

Fig. 2. BSE images of unaltered AOA #214. It consists of nearly pure forsterite (fo), high-Ca pyroxene (cpx), anorthite (an), and spinel (sp). Anorthite is partly replaced by phyllosilicates (phyl).

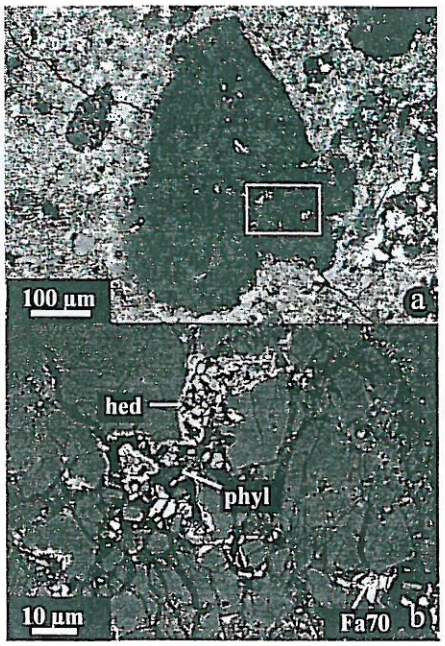

Fig. 3. BSE image of altered AOA #5. Anorthite is completely replaced by phyllosilicates (phyl). Hedenbergite (hed) and fayalite are observed in direct contact with phyllosilicates. Occasionally, fayalite grains are rather coarse and show inverse compositional zoning.

Table 1. Representative analysis of minerals in AOAs.

mineral	Fo	cpx	an	en	cpx
AOA #	15	2	214	202	15
SiO_2	43.6	49.0	42.8	58.8	52.0
Al_2O_3	0.91	5.4	37.2	0.20	5.4
TiO_2	0.30	2.4	0.03	n.a.	0.63
FeO	1.3	1.3	0.93	0.60	0.53
MnO	0.12	0.06	0.01	0.10	2.0
MgO	51.5	22.3	0.7	37.2	18.1
CaO	2.0	20.3	18.4	2.6	18.3
Na_2O	0.05	n.a.	0.15	n.a.	0.11
K_2O	0.04	n.a.	0.02	n.a.	0.02
Cr_2O_3	0.22	0.07	0.04	0.10	1.9
V_2O_3	0.03	n.a.	n.a.	n.a.	n.a
NiO	0.12	n.a.	0.03	0.10	0.03
P_2O_5	n.a.	0.24	0.25	n.a.	0.15
Total	100.2	101.0	100.5	99.9	99.0
Fa	1.4	-	-	-	-
Wo	-	38.8	-	4.8	41.7
En	-	59.3	-	94.3	57.4

fo = forsteritic olivine, cpx = Al-diopside, an = anorthite, en = enstatite, rim cpx = euhedral high-Ca pyroxene in the rim of AOA.

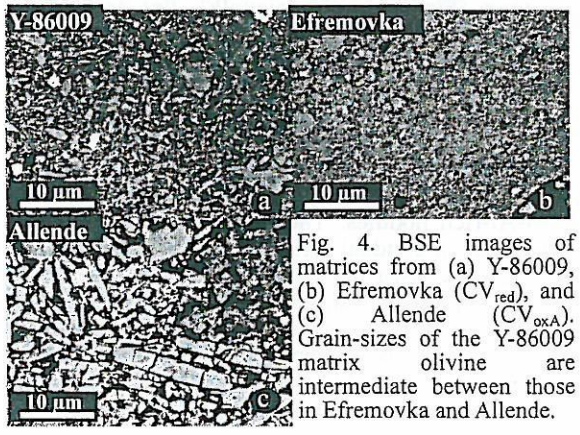

Fig. 4. BSE images of matrices from (a) Y-86009, (b) Efremovka (CV_{red}), and (c) Allende (CV_{oxA}). Grain-sizes of the Y-86009 matrix olivine are intermediate between those in Efremovka and Allende.

Al-Mg ISOTOPIC CONSTRAINTS ON ALTERATION OF ALLENDE Ca-Al-RICH INCLUSIONS. T. J. Fagan[1], Y. Guan[2] and G. J. MacPherson[3], [1]Waseda University, Geology Department, 1-6-1 Nishiwaseda, Shinjuku, Tokyo, 169-8050, Japan (fagan@waseda.jp), [2]Department of Geological Sciences, Arizona State University, Tempe, AZ 85287, USA. National Museum of Natural History, Smithsonian Institution, Washington, DC 20560, USA.

Introduction: Ca-Al-rich inclusions (CAIs) from the Allende CV3 chondrite show textures indicating that melilite and to some extent, primary anorthite were partially replaced by secondary minerals, including grossular, monticellite, secondary anorthite and feldspathoids [1-4]. Whether these secondary minerals originated during one or multiple stages of alteration, and in a nebular or asteroidal setting or both, have implications for nebular history and alteration processes. This study is a continuation of our efforts to address this issue using Al-Mg isotope systematics to evaluate the timing of alteration.

Analytical Methods: Polished thin sections of two Allende CAIs, USNM 4022-1 and USNM 3529-47-1, were characterized using a petrographic microscope and a JEOL JSM-840A scanning electron microscope (SEM). Elemental compositions were measured with both energy dispersive (on the SEM) and wavelength dispersive techniques (using a JEOL JXA-8900 electron microprobe).

Isotopic measurements were collected using the ASU Cameca ims-6f ion microprobe. A 12.5 kV O^- primary beam of 0.05 – 0.2 nA was focused into a <5 μm spot for all analyses. Secondary ions were accelerated to 10 kV and collected with an energy band-pass of ~50 V under a mass resolving power of ~3500.

Mineralogy and Textures: CAI 4022-1 is a type B2 CAI with coarse-grained primary melilite, anorthite, Ca-Ti-pyroxene (fassaite) and Mg-spinel, and an incomplete Wark-Lovering (WL) rim dominated by diopside. A narrow zone inside of the WL diopside is dominated by fine-grained feldspathoid, Fe-bearing spinel., and thin laths of secondary anorthite. Feldspathoid-rich patches also occur in the interior of the CAI (Fig. 1A), where the secondary anorthite is coarser and more equant than the lath-shaped anorthite near the CAI rim. Melilite and primary anorthite throughout the CAI are transected and bounded by alteration veins dominated by grossular with some monticellite or secondary anorthite (Fig. 1A).

CAI 3529-47-1 is a fluffy type A CAI composed of numerous individual nodules enclosed in and partially separated from one another by meteorite matrix and accretionary rim material. Melilite is the dominant primary mineral in the nodules, with accessory spinel and perovskite; diopside forms a thin rim around each nodule (Fig. 1B). All of the nodules show some replacement of primary melilite by fine-grained secondary lath-like anorthite, feldspathoids, grossular, and Fe-bearing spinel (Fig. 1B).

Al-Mg Isotopic Results: Some analyses of primary anorthite from CAI 4022-1 have ^{26}Mg excesses indicating "canonical" [5] initial $^{26}Al/^{27}Al$ ratios (Fig. 2A); however, several analyses, particularly those with high Al/Mg ratios, form a spread with lower relative ^{26}Mg excesses. We infer that this deviation from canonical is caused primarily by partial re-equilibration after initial crystallization (e.g., [6]). In addition to these results, one analysis of primary anorthite with exceptionally high Al/Mg (~1050) exhibits no ^{26}Mg excess.

All analyses of secondary anorthite from 4022-1 show no excesses of ^{26}Mg (Fig. 2A). The other secondary phases have lower Al/Mg; however, resolvable excess ^{26}Mg ($^{26}Mg/^{24}Mg$ = 0.1403 ±0.0003, $^{27}Al/^{24}Mg$ = 29.6 ±0.9, initial $^{26}Al/^{27}Al$ ~ $3x10^{-5}$; uncertainties reported throughout are 2σ) was detected in one of three grossular grains analyzed.

Analyses of gehlenitic melilite from fluffy type A CAI 3529-47-1 show canonical Al-Mg isotopic systematics (Fig. 2B). Except for one analysis of sodalite ($^{26}Mg/^{24}Mg$ = 0.139 ±0.003, $^{27}Al/^{24}Mg$ = 2200 ±100) and one of anorthite ($^{26}Mg/^{24}Mg$ = 0.1388 ±0.0004, $^{27}Al/^{24}Mg$ = 31.8 ±1.6), our results from secondary anorthite, grossular and feldspathoids from this CAI have ^{26}Mg excesses that correlate with Al/Mg (Fig. 2C). A regression through these points (excluding the sodalite and anorthite noted above) yields initial $^{26}Al/^{27}Al$ of 4.7 (±2.6) $x10^{-6}$ with initial $^{26}Mg/^{24}Mg$ = 0.13985 ±0.00020 (MSWD = 0.74).

Timing and Setting of Alteration Events: These analyses combined with our initial results from a type B2 and a compact type A CAI [4] suggest complex alteration histories for Allende CAIs. Most of the secondary phases from the three compact CAIs investigated show no excesses of ^{26}Mg, consistent with late (parent-body setting) alteration. However, some grossular analyses have significant ^{26}Mg, excesses, as do nearly all the secondary phases analyzed from a fluffy type A CAI. If the Al-Mg system can be applied as a chronometer in this case, Allende CAIs appear to have undergone some alteration prior to formation of the Allende parent body. Fluffy Type A CAIs may be more generally characterized by early (nebular?) alteration relative to

type B and compact Type A CAIs; more data are require to confirm this possibility.

References: [1] Hutcheon I. D. and Newton R. C. (1981) *LPS XII*, 491-493. [2] Wark D. A. (1981) *LPS XXII*, 1145-1147. [3] Davis A. M. et al. (1994) *LPS XXV*, 315-316. [4] Fagan T.J. et al. (2005) *LPS XXXVI*, #1820. [5] MacPherson G.J. et al. (1995) *Meteoritics 30*, 365-386. [6] Podosek F.A. et al. (1991) *GCA 55*, 1083-1110.

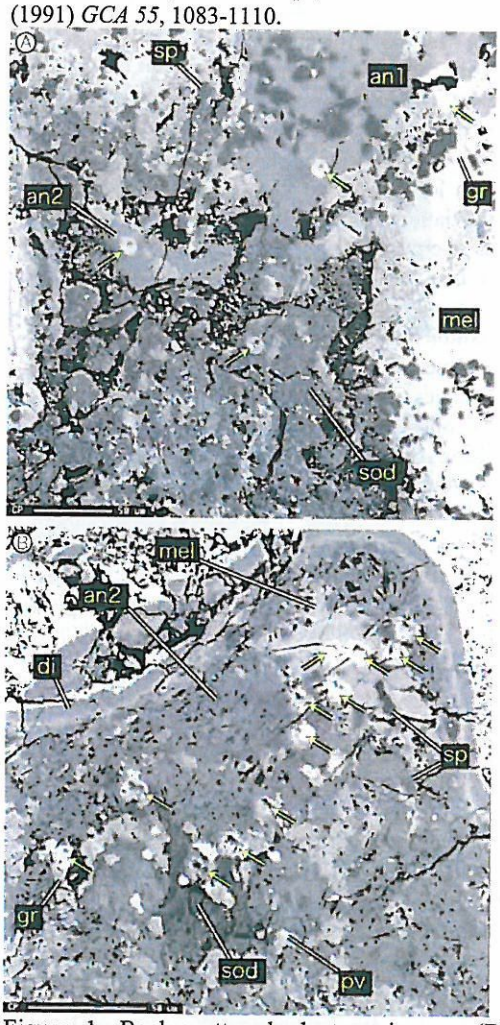

Figure 1. Back-scattered electron images (BEI) showing mineralogy and textures of altered domains in Allende CAIs. The BEI are overlain on secondary electron images to highlight SIMS craters (arrows). (A) Feldspathoid-rich patch in the interior of type B2 CAI 4022-1. (B) Secondary anorthite-rich domain near the margin of a melilite nodule of fluffy type A CAI 3529-47-1. Abbreviations: an1 = primary anorthite; an2 = secondary anorthite; di = diopside; gr = grossular; mel = melilite; pv = perovskite; sod = sodalite; sp = spinel.

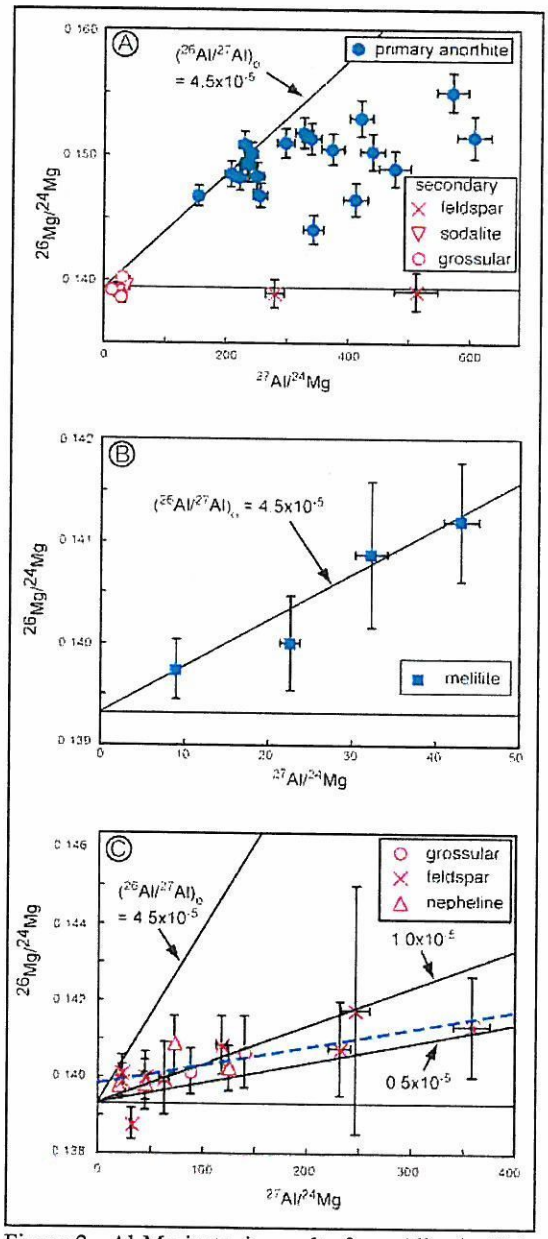

Figure 2. Al-Mg isotopic results from Allende CAIs 4022-1 (A) and 3529-47-1 (B, C). Error bars show 2σ analytical error. Two analyses with normal $^{26}Mg/^{24}Mg$ have Al/Mg too high to be plotted in (A) and (C): primary anorthite in 4022-1 ($^{27}Al/^{24}Mg$ ~ 1050) and sodalite in 3529-47-1 ($^{27}Al/^{24}Mg$ ~ 2200). Lines showing initial Al isotopic ratios are not fits to the data; rather, they are shown for reference. Blue dashed line in C is a fit to data excluding analyses of sodalite with $^{27}Al/^{24}Mg$ ~ 2200 (not plotted) and feldspar with $^{27}Al/^{24}Mg$ =32, $^{26}Mg/^{24}Mg$ = 0.1388 (plotted).

AMOEBOID OLIVINE AGGREGATES IN THE YAMATO-86009 CV3 CHONDRITE. M. Komatsu[1], T. Fagan[2], M. Miyamoto[3], A.N. Krot[4] and T. Mikouchi[3], [1]The University Museum, University of Tokyo, 7-3-1 Hongo Bunkyo-ku Tokyo, Japan (mutsumi@um.u-tokyo.ac.jp), [2]Department of Earth Sciences, School of Education, Waseda University, 1-6-1 Nishiwaseda Shinjuku-ku Tokyo, Japan, [3]Department of Earth & Planetary Science, University of Tokyo, Japan. [4]Hawaii Institute of Geophysics and Planetology, University of Hawaii at Manoa, USA.

Introduction: Amoeboid olivine aggregates (AOAs) are important refractory components of carbonaceous chondrites (except CH and CB chondrites) and have been interpreted to represent solar nebular condensates that experienced high-temperature annealing, but largely escaped melting [1]. Because AOAs in primitive chondrites are composed of fine-grained minerals (forsterite, anorthite, spinel) that are easily modified during postcrystallization alteration, the mineralogy of AOAs can be used as a sensitive indicator of metamorphic or alteration processes [1, 2]. In order to understand the alteration history of the CV3 chondrites, we performed mineralogical studies of AOAs in the Yamato-86009 CV carbonaceous chondrite. Although oxygen isotope compositions of the Y-86009 AOAs have been previously reported [3], their mineralogical studies have not been described yet. Here we report the mineralogy and petrography of AOAs in this meteorite and compare them to those in other CV3 chondrites.

Samples and analytical procedure: Two polished thin sections of Y-86009, 51-1 and 51-2, were studied using optical microscopy, SEM, EBSD (Electron back-scattering diffraction) and EPMA.

Results: Y-86009 consists of chondrules (53 vol%), AOAs (2 vol%), Ca-Al-rich inclusions (1 vol%) and fine-grained matrix (43 vol%) with isolated mineral fragments (1 vol%). In chondrules, anorthite-normative mesostasis is partly replaced by Al-bearing phyllosilicates. AOAs are commonly surrounded by ~20-μm-thick accretionary rims dominated by fine-grained fayalitic olivine (Fa_{10-40}). The rims are often discontinuous and portions of AOAs are observed in direct contact with the Y-86009 matrix. In contrast, fine-grained rims around chondrules are commonly complete.

Mineralogy and petrography of AOAs: AOAs are irregularly-shaped objects, 50-750 μm in size, composed of anhedral, fine-grained (1-20 μm) olivines and refractory, Ca-Al-rich nodules. Here we describe three typical AOAs.

AOA #5 is a porous aggregate mainly composed of fine-grained forsteritic olivine (Fo_{96-99}) and Al-diopside (Fig. 1). Anorthite is rare; it is largely replaced by fine-grained Mg, Al-silicates, which although are too small to be analyzed by EPMA, appear to be similar in BSE images to phyllosilicates described in the Mokoia CAIs [4]. The anhderal grains of Ca-Fe-rich pyroxene (hedenbergite?) occur along grain boundaries. Euhedral fayalitic olivine grains (Fa_{63-71}) overgrow forsterite. Hedenebrgite and fayalite are occasionally observed in direct contact with phyllosilicates.

AOA #2, 170 μm in size, shows similar mineralogy to AOA #5 (Fig. 2). Anorthite is partly replaced by Al-bearing phyllosilicates. Fayalite grains are rather coarse and show inverse compositional zoning, possibly indicating Fe-Mg exchange with a fluid phase.

AOA #15 is a porous aggregate composed of fine-grained olivine (Fo_{92-99}), Al-diopside, and spinel (FeO 2-6 wt%). Most of the anorthite is replaced by fine-grained Al-bearing phyllosilicates. Olivine shows enrichment in FeO along the grain boundaries, in contact with phyllosilicates. Some forsterite grains are overgrown by euhedral pyroxene ($Wo_{41}En_{56}Fs_3$, < 10 μm in size) along the rim of the AOA (Fig. 3). This pyroxene has higher content of MnO and Cr_2O_3 (~1.9 wt%) than Al-diopside associated with spinel in the interior of the AOA. Secondary fayalitic olivine is absent. In this AOA, an unusual anorthite-like phase (ALP) is observed (Fig. 3). It is ~100 μm in size, and has a homogeneous composition similar to anorthite, but with high FeO (Table 1). EBSD study shows the phase is probably a glass. Porous enstatite (Wo_7En_{91}) and a silica-rich phase, which contains minor Mg and Al, are enclosed in the anorthite-like phase.

Discussion: AOAs in Y-86009 are mainly composed of forsteritic olivine, Al-diopside and spinel. Although they are texturally similar to those in the reduced and the Allende-like oxidized CV chondrites [7], they show important mineralogical differences. The Y-86009 AOAs experienced hydrous alteration that resulted in replacement of anorthite by phyllosilicates. Most forsterite grains have undergone minimal, if any, alteration; some olivines show enrichment in FeO (Fig. 4). In addition to phyllosilicates, other secondary minerals are fayalite and hedenbergite. These alteration features are similar to those in CAIs, chondrules, and matrices of the Bali-like oxidized CVs [7]. The characteristic alteration minerals of the Allende AOAs, which include zoned ferrous olivine, nepheline and sodalite are absent in the Y-86009 AOAs. We infer that AOAs in Y-86009 were originally similar to those in reduced CVs [9], and subsequently experienced low-temperature aqueous alteration; they largely escaped Fe-alkali metasomatic alteration that resulted in formation of nepheline and sodalite in the Allende AOAs [7]. The presence of the anorthite-like phase (glass?) indicates that some AOAs may have experienced melting and rapid cooling.

References: [1] Krot A. N. et al. (2004) *Chem. Erde, 64,* 185-282. [2] Chizmadia L.J. et al. (2002) *MAPS, 37,* 1781-1796. [3] Hiyagon H. and Hashimoto A. (1999) *Science, 283,* 828-831. [4] Cohen R.E. et al. (1983) *GCA, 4I,* 1739–1757. [5] Komatsu M. et al. *MAPS 36,* 629-643 [6] Komatsu M. (2003) Ph.D thesis. University of Tokyo. [7] Krot A.N. et al. (1998)

MAPS 33, 623-645. [8] Krot A. N. et al. (1995) *Meteoritics 30*, 748-776.

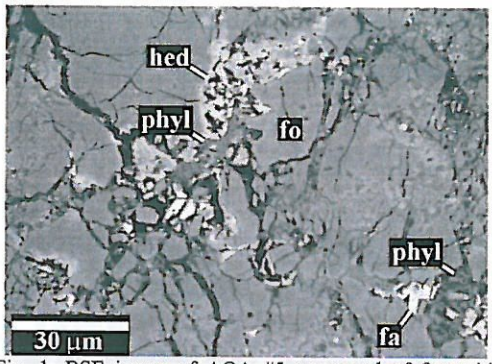

Fig. 1. BSE image of AOA #5 composed of forsteritic olivine (fo) and secondary phyllosilicate (phyl), fayalitic olivine (fa) and hedenbergite (hed).

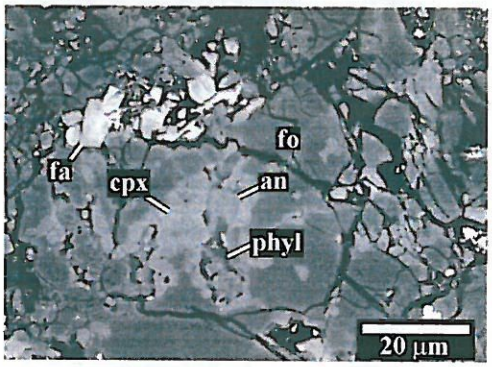

Fig. 2. BSE image of AOA #2 composed of forsteritic olivine (fo), anorthite (an), and Al-diopside (cpx). Anorthite is partly replaced by phyllosilicates (phyl); Forsteritic olivines are overgrown by fayalitic olivine grains (fa) which show inverse compositional zoning.

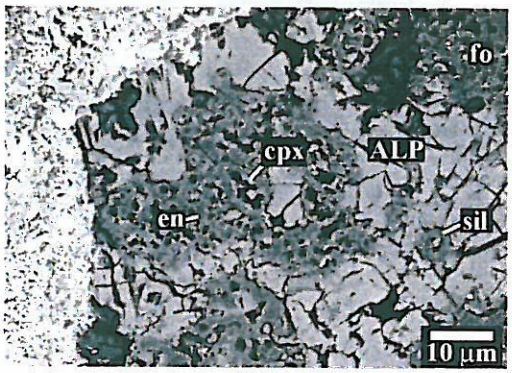

Fig. 3. BSE image of AOA #15 containing anorthite-like phase (ALP) enclosing enstatite (en), Al-diopside (cpx), and silica-rich phase (sil).

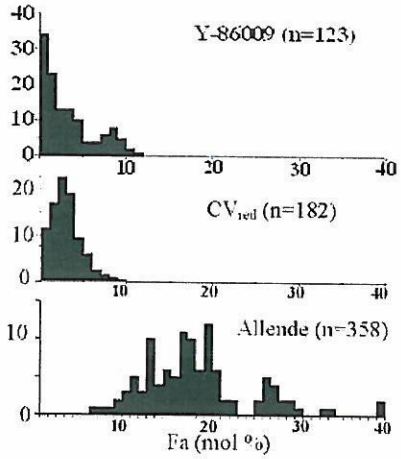

Fig. 4. Histograms of olivine compositions in AOAs from Y-86009, reduced CV chondrites Leoville, Vigarano, Efremovka (CV_{red}) [5], and oxidized CV chondrites Allende [6]. Olivines in the Y-86009 AOAs are less ferrous than those from the Allende AOAs and have similar compositional ranges to those from the reduced CV chondrites.

Table 1. Representive analyses of minerals in AOA.

	fo	cpx	an	en	ALP	rim cpx
AOA #	15	2	202	15	15	15
SiO_2	43.6	49.0	42.8	52.5	42.7	52.0
Al_2O_3	0.91	5.4	37.2	5.2	33.7	5.4
TiO_2	0.30	2.4	0.03	0.73	0.05	0.63
FeO	1.3	1.3	0.93	0.93	8.1	0.53
MnO	0.12	0.06	0.01	0.15	0.32	2.0
MgO	51.5	22.3	0.7	34.9	0.28	18.1
CaO	2.0	20.3	18.4	3.8	12.7	18.3
Na_2O	0.05	n.a.	0.15	0.24	2.0	0.11
K_2O	0.04	n.a.	0.02	0.06	0.05	0.02
Cr_2O_3	0.22	0.07	0.04	0.39	n.a.	1.9
V_2O_3	0.03	n.a.	n.a.	0.04	0.04	n.a
NiO	0.12	n.a.	0.03	0.15	n.a.	0.03
P_2O_5	n.a.	0.24	0.25	0.02	0.16	0.15
total	100.2	101.0	100.5	99.1	99.9	99.0
Fa	1.4	-	-	-	-	-
Wo	-	38.8	-	7.2	-	41.7
En	-	59.3	-	91.4	-	57.4

an = anorthite; ALP = anorthite-like phase; cpx = Al-diopside; en = enstatite; fo = forsteritic olivine.

PRESOLER SILICATE GRAINS IN ENSTATITE CHONDORITES S. Ebata[1], K. Nagashima[2], S. Itoh[1], S. Kobayashi[1], N. Sakamoto[1], T. J. Fagan[3], and H. Yurimoto[1], [1]Division of Earth and Planetary Sciences, Hokkaido University, Sapporo 060-0810, Japan. (ebashin@ep.sci.hokudai.ac.jp); [2]Hawai'i Institute of Geophysics and Planetology, School of Ocean and Earth Science and Technology, University of Hawai'i at Manoa, Honolulu, HI 96822, USA; [3]Department of Earth Sciences, School of Education, Waseda University, Tokyo, Japan.

Introduction: Primitive meteorites contain presolar grains that predate the formation of our solar system. Recently presolar silicate grains were identified in IDPs [1] and in primitive carbonaceous and ordinary chondrites [2-6]. In enstatite chondrites, presolar carbonaceous and oxide grains have been reported [e.g. 7-9], but no presolar silicate grains have been identified.

Here we report the first finding of presolar silicates from enstatite chondrites. We used an isotope microscope [10] to identify presolar grains in three primitive enstatite (EH3) chondrites: Yamato (Y)-691, Allan Hills (ALHA) 81189, and Sahara (SAH) 97072.

Experimental: The samples used in this study are polished thin sections of Y-691, ALHA 81189, and SAH 97072. Mineralogical and petrographical characterization of matrices was conducted using a scanning electron microscope (JEOL JSM-5310LV) equipped with energy dispersive X-ray spectrometer (Oxford LINK ISIS). After the characterization, we surveyed presolar grains by isotopography using an isotope microscope system (Cameca ims-1270 + SCAPS [10]); originally installed in TiTech and now in Hokkaido Univ. (Hokudai).

The analytical techniques for isotopography basically followed those described in elsewhere [3]. We acquired the following isotopographs for each analyzing field as a sequence of $^{12}C^-$, $^{13}C^-$, $^{12}C^-$, $^{27}Al^-$, $^{28}Si^-$, $^{16}O^-$, $^{18}O^-$, $^{16}O^-$, $^{17}O^-$, and $^{16}O^-$. Total integration time for one field was ~1 hour. In order to obtain better lateral resolution of isotopographs than the case of [3], a smaller contrast aperture (50 μm in diameter) was used in this study except for the case of C-isotopes. A larger contrast aperture (150 μm in diameter) was used for C-isotopographs in order to minimize sample consumption by sputtering with an enough precision of isotope ratio through the sequence. Lateral resolutions of the isotopographs using contrast aperture of the 50 μm and of the 150μm are 0.3-0.5 μm and ~1 μm, respectively. These analytical conditions keep the sputtering depth less than 100 nm for the sequence.

The digital image processing using a moving-average (3 x 3 pixels) was applied to simple secondary ion ratio images in order to reduce the statistical error. The selection criterion for distinguishing presolar grains and estimation of the analytical errors of the grains are the same as [3].

Results: The total analyzed areas of oxygen isotopographs are ~61,000 μm^2, ~58,000 μm^2, and ~30,000 μm^2 for Y-691, ALHA 81189, and SAH 97072, respectively. From the analyzed areas, 3 and 9 presolar silicates were identified for Y-691 and ALHA 81189, respectively (e.g. Fig. 1), whereas no presolar silicates for SAH 97072. Presolar carbonaceous grains were also identified by carbon isotopographs: 10 grains from areas of ~63,000 μm^2 for Y-691; 6 from ~61,000 μm^2 for ALHA 81189; and 2 from ~32,000 μm^2 for SAH 97072 (e.g. Fig. 2).

Matrix-normalized abundances of presolar silicate grains were calculated to be ~49, ~155 and <33 grains/mm^2 corresponding to ~4, ~14 and <3 ppm for Y-691, ALHA 81189 and SAH 97072, respectively, assuming the mean grain size to be 0.3 μm in diameter.

Matrix-normalized abundances of presolar carbonaceous grains were calculated to be ~159, ~98 and ~62 grains/mm^2 corresponding to ~14, ~9 and ~6 ppm for Y-691, ALHA 81189 and SAH 97072, respectively, assuming the mean grain size to be 0.3 μm in diameter.

Discussion: The carbonaceous presolar grains are roughly equally distributed in the three EH3 chondrites in this study. The average abundance is ~10 ppm that is consistent with the value estimated from abundances of exotic noble-gas components from acid-resistant residue of Qingzhen EH3 meteorite (10.9 ppm [7]). The smaller abundance in SAH 97072 may be due to decomposition of the presolar carbonaceous grains by thermal and/or aqueous metamorphism in the parent body.

The abundance of presolar silicates is the highest in ALHA 81189 and continues to Y-691, SAH 97072. The lowest abundance for SAH 97072 is the same as the case of carbonaceous grains. These results support that metamorphic degree is highest in SAH 97072 among the three EH3 chondrites.

The abundance of presolar silicates is much smaller in EH3 chondrites than in primitive carbonaceous chondrites [5]. The EH3 chondrites, like most type 3 carbonaceous chondrites, have undergone some parent body metamorphism. The small abundance in EH3 chondrites suggests that

parts of the presolar silicate grains of EH3 chondrites have been decomposed by the mild thermal metamorphism. Other possibilities are that the EH3-matrix materials have been affected thermally during chondrule formation or diluted to a greater extent by fragmentation of chondrules. We infer that the abundance of presolar silicate grains (14 ppm) of ALHA 81189 is a minimum estimate of the original abundance for EH3 chondrite formation area in the solar nebula.

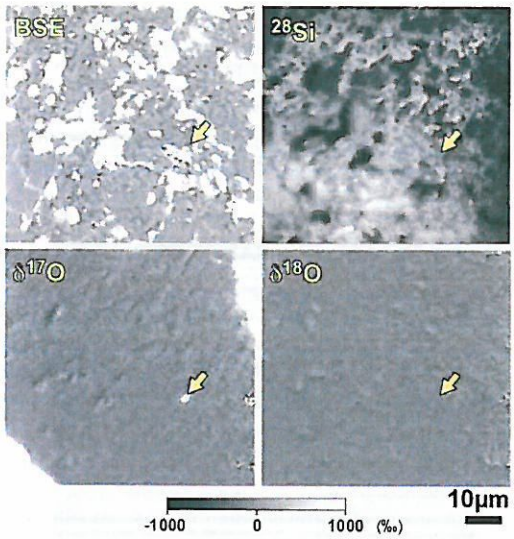

Fig. 1. Corresponding images of BSE, secondary ion ($^{28}Si^-$), and O-isotope ratios ($\delta^{17}O$ and $\delta^{18}O$) from Y-691. Yellow arrows indicate locations of presolar silicate grain. White areas at upper-right and lower-left corners of $\delta^{17}O$ image show interferences of $^{16}OH^-$.

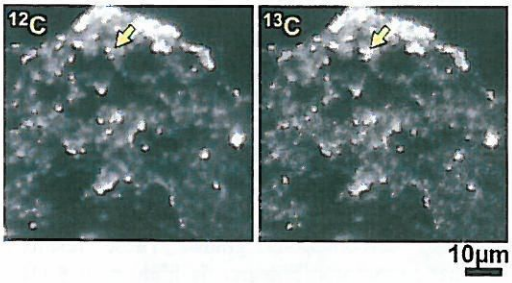

Fig. 2. Corresponding images of secondary ion ($^{12}C^-$ and $^{13}C^-$) from Y-691. Yellow arrows indicate locations of presolar carbonaceous grain.

The oxygen isotopic compositions of presolar silicates in the EH3 chondrites are shown in Fig. 3. The most grains (~ 80%) have excesses in ^{17}O with nearly normal $^{18}O/^{16}O$ ratios. These grains are categorized into group 1, which likely formed around O-rich red giant and asymptotic giant branch stars. The rest belongs to group 4, which have nearly normal $^{17}O/^{16}O$ ratios and excesses in ^{18}O. The origin of the group is considered as asymptotic giant branch stars or super novae [11].

References: [1] Messenger et al. (2003) *Science* **300**, 105-108. [2] Nguyen and Zinner (2004) *Science* **303**, 1496-1499. [3] Nagashima et al. (2004) *Nature* **428**, 921-924. [4] Mostefaoui and Hoppe (2004) *ApJ* **613**, L149-L152. [5] Kobayashi et al. (2005) *Antarct. Meteor.* **XXIX**, 30-31. [6] Tonotani et al. (2006) *LPS* **XXXVII**, this volume. [7] Huss and Lewis (1995) *GCA* **59**, 115-160. [8] Besmehn et al. (2001) *MAPS* **36**, A20. [9] Lin et al. (2002) *ApJ* **575**, 257-263. [10] Yurimoto et al. (2003) *Appl. Surf. Sci.* **203-204**, 793. [11] Nittler et al. (1997) *ApJ* **483**, 475-495.

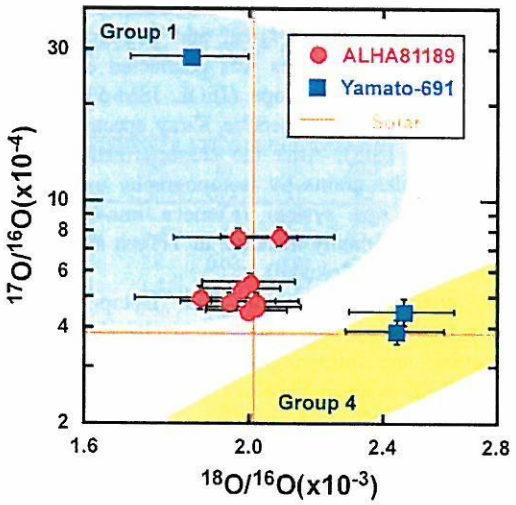

Fig. 3. O-isotopic ratios of presolar silicate grains from Y-691 and ALHA 81189. Error bars are 2σ. Ten grains belong to Group 1 and two grains belong to Group 4 defined by [11].